Evolution of self-interacting axion around rotating black holes

Hidetoshi Omiya

Department of Physics, Graduate School of Science,
Kyoto University, Kyoto 606-8502, Japan

February 6, 2023

Abstract

Axions are one of the most motivated particles beyond the standard model. One of the motivations to consider axions is the string theory, which predicts a plentitude of axions in our universe, which is called the axiverse scenario. The axions from the string theory can have mass in various ranges. In particular, when the axion has a mass with its Compton wavelength comparable to the size of rotating black holes, the macroscopic condensate of the axion will spontaneously form by the energy and angular momentum extraction mechanism called superradiance. The presence of the axion condensate opens the possibility of detecting or constraining the axion through gravitational wave observations. One possibility is the detection of characteristic gravitational waves emitted by the condensate. In particular, self-interaction of the axion is thought to cause the violent collapse of the condensate, called bosenova, which leads to the burst of gravitational waves. On the other hand, the self-interaction also dissipates the condensate, which may result in the saturation of the condensate. In such a case, condensate will emit continuous gravitational waves. To detect or constrain the axion with future gravitational wave observations, precise knowledge of the evolution of the self-interacting axion around the rotating black hole is required.

In this thesis, we study the effect of the self-interaction on the evolution of the axion condensate. Our main goal is to track the evolution of the self-interacting condensate, starting from the extremely small amplitude, such as the quantum fluctuation, to the large amplitude where bosenova may happen. We propose two new methods, the perturbative and the non-perturbative numerical methods, to examine the evolution. The basic strategy in both methods is to employ the adiabatic approximation, the large hierarchy between the growth time scale and the dynamical time scale. With our methods, we find that the evolution of the condensate depends on the mass of the axion. In particular, we show that for most of the axion mass the condensate is likely to evolve into the quasi-stationary configuration, in which the energy gain by the superradiance and the dissipation by the self-interaction balance. For this case, bosenova is not expected. We also present exceptional cases when bosenova can be expected.

Contents

Chapter 1

Introduction

Axions are well-motivated particles beyond the Standard Model in a variety of contexts. They were originally proposed as a solution to the strong CP problem [1, 2, 3, 4, 5, 6, 7], and then noticed to be a good candidate for dark matter [8, 9, 10, 11, 12]. In addition, string theory naturally predicts plentitude of axions in its low energy sector [13, 14, 15, 16], which is called *axiverse* scenario [15]. In the axiverse scenario, axions can have Compton wavelengths in various scales, up to cosmological scales. In this thesis, we focus on the axions in the string theory (string axion) with the Compton wavelength in the range of astrophysical scales. In such cases, axions are expected to cause various interesting astrophysical phenomena, which are detectable by gravitational wave observations [15, 17].

We consider an axion field around a rotating black hole. Similar to the famous Penrose process [18, 19], a bosonic field can extract the energy and the angular momentum from the rotating black hole. This energy extraction mechanism is called *superradiance* [20, 21, 22, 23, 24, 25]. Note that the axion is bounded by the gravitational potential of the black hole, owing to its mass. Therefore, the axion which extracted energy from the black hole does not dissipate to infinity. Therefore, the bounded axion accumulates around the black hole, which implies instability. This instability is called *superradiant instability* [26, 27, 28, 29, 30, 25], and its time scale can be much shorter than the age of the Universe when the Compton wavelength of the axion is comparable to the size of the black hole. Due to the superradiant instability, the axion would spontaneously form a macroscopic condensate around the rotating black hole. In this thesis, we call the macroscopic condensate of the axion an *axion condensate*. For the special case when the axion condensate is composed of the single unstable mode, we refer it as an *axion cloud*.

The presence of the axion condensate allows us to detect the axion through gravitational wave observations. Since the axion condensate grows by extracting the rotational energy of the black hole, the existence of the axion implies the spin-down of the black hole [17, 31]. The spin-down by the axion might be observed through the distribution of the black hole spin. In addition, the axion condensate has the quadrupole moment and thus radiates continuous gravitational waves. Observation of the characteristic gravitational waves can also verify the axion [32, 33, 34, 35, 36].

Several effects can have an impact on the evolution of the axion condensate. These effects include the axion self-interaction [17, 37, 38, 39, 40, 41, 42], the tidal interaction in binary systems [43, 44, 45, 46, 47, 48, 49], and interactions with other fields [50, 51]. The axion self-interaction is particularly interesting among these effects. For example, if the self-interaction is attractive, the condensate is thought to collapse when it becomes dense [37, 39]. This collapse, called bosenova, is thought to cause a burst of gravitational

waves. It has also been suggested that the interaction between clouds may dissipate the energy of the condensate efficiently and forces it to settle into a quasi-stationary state [42]. In such cases, explosive phenomena will not occur.

However, the previous works on the self-interaction have to be improved to constrain or detect the axion by future gravitational wave observations. Most works treat the self-interaction perturbatively [17, 40, 41, 42], but perturbative expansion breaks down once the growth is accelerated by the attractive self-interaction (see Chpater 3). In addition, many works assume non-relativistic approximation, where the Compton wavelength of the axion is much longer than the size of the black hole. The non-relativistic approximation allows one to calculate in analytic form but cannot handle the most interesting parameter region where the instability time scale is shortest. Furthermore, low order perturbation theory misses the deformation of the condensate.

Other works study the self-interaction by the numerical simulations [37, 39]. The limitation of the dynamical simulation comes from the large hierarchy between the dynamical time scale and the instability time scale. For this reason, numerical simulation can be performed only in a time much shorter than the time shorter than the condensate grows from a small amplitude where the linear approximation is valid to a large amplitude where the self-interaction collapses the condensate. Thus, to study the evolution in a strongly nonlinear regime, one needs to guess the configuration of the condensate with a large amplitude. In [37, 39], they take the initial condition for the numerical simulation by simply scaling the solution of the linearized equation. However, it is difficult to justify such an initial condition since the condensate changes its shape by the effect of self-interaction as it grows.

The aim of this thesis is to study the consistent evolution of the self-interacting axion condensate. In particular, we focus on tracking the evolution from small to large amplitude, where the nonlinearity is strong. We overcome the above problems by formulating higher order perturbation theory which can be used for any axion mass [52, 53] (Chapter 3) and developing a method to track the nonlinear evolution [54, 53] (Chapter 4). Our basic strategy is to use the adiabatic nature of the problem, which is a significant discrepancy between the dynamical time scale and the instability time scale. Our calculation shows the condensate settles to a quasi-stationary state in most cases owing to the dissipation of the condensate by the self-interaction. This indicates that explosive phenomena rarely happen. Moreover, we show that the realized quasi-stationary state turns out to be stable against further level transition due to the self-interaction [53] (Chapter 5). We also show an exceptional case when the dissipative effects are too weak to prevent the condensate from the explosion [53] (Chapter 6).

In this thesis, we take the unit $c = G = \hbar = 1$ unless otherwise stated. The useful conversion in our unit is

$$1\text{eV} \sim 7.5 \times 10^9 M_\odot^{-1} \sim 5.1 \times 10^9 \text{km}^{-1} \sim 1.5 \times 10^{15} \text{s}^{-1} \ .$$

Thus, the Compton wavelength of the axion is comparable to the size of the solar mass black hole when the axion mass is $\sim 10^{-10}$eV. Also, our metric convention is $(-, +, +, +)$. This thesis is organized as follows.

Chapter 2

We review the basics of the axion condensate, superradiant instability and the observable phenomena associated with it.

Chapter 3

We formulate the perturbative method to take into account the effect of the self-interacting condensate. This Chapter is based on the author's previous work:

H. Omiya, T. Takahashi and T. Tanaka, "Renormalization group analysis of superradiant growth of self-interacting axion cloud," PTEP **2021**, no.4, 043E02 (2021) [52],

and the work under the review:

H. Omiya, T. Takahashi, T. Tanaka and H. Yoshino, "Impact of multiple modes on the evolution of self-interacting axion condensate around rotating black holes," [arXiv:2211.01949 [gr-qc]] [53].

Chapter 4

We formulate the nonlinear method to track the evolution of the condensate in the strongly nonlinear regime. This Chapter is based on the author's previous work:

H. Omiya, T. Takahashi and T. Tanaka, "Renormalization group analysis of superradiant growth of self-interacting axion cloud," PTEP **2021**, no.4, 043E02 (2021) [52],

and the work under review:

H. Omiya, T. Takahashi, T. Tanaka and H. Yoshino, "Impact of multiple modes on the evolution of self-interacting axion condensate around rotating black holes," [arXiv:2211.01949 [gr-qc]] [53].

Chapter 5

We investigate whether the configuration obtained in the previous chapters can be altered by further perturbative effects or not. This Chapter is based on the author's work under review:

H. Omiya, T. Takahashi, T. Tanaka and H. Yoshino, "Impact of multiple modes on the evolution of self-interacting axion condensate around rotating black holes," [arXiv:2211.01949 [gr-qc]] [53].

Chapter 6

We briefly comment on the case in which the condensate starts with the dominance of a higher multipole mode.This Chapter is based on the author's work under review:

H. Omiya, T. Takahashi, T. Tanaka and H. Yoshino, "Impact of multiple modes on the evolution of self-interacting axion condensate around rotating black holes," [arXiv:2211.01949 [gr-qc]] [53].

Chapter 6

We summarize our study and comment on its future direction.

Chapter 2

Review: Axion Cloud

If the string axion exists in our universe with an appropriate mass range, the axion will spontaneously form a macroscopic condensate of the axion around a rotating black hole. The basic formation mechanism is superradiance, which is the energy and the angular momentum extraction from the black hole by a bosonic field. If the condensate significantly grows within the age of the universe, it will induce observable phenomena. One is the spin-down of the black hole. Since the axion cloud extracts the angular momentum from the black hole, a highly spinning black hole in the corresponding mass range is forbidden if the axion exists. Another is the emission of the characteristic gravitational waves. These phenomena open the possibility of detecting the axion by gravitational wave observations.

In this chapter, we review the basics of the axion condensate. In Sec. 2.1, we briefly review the superradiance and the instability associated with it. In Sec. 2.2, we present the solution of the linearized equation of motion of the axion field around a rotating black hole. Finally, in Sec. 2.3, we summarize possible observational signatures of the axion cloud.

2.1 Superradiance and superradiant instability

2.1.1 Superradiance

Superradiance is the scattering process of the wave where the reflected wave has a larger amplitude than the incident wave. Here, we explain the superradiance of a massless complex scalar field Φ by a rotating black hole. The equation of motion of the scalar field Φ is given by

$$\Box_g \Phi = 0 \ , \tag{2.1}$$

where $\Box_g$ is the d'Alambertian in the Kerr space-time, whose explicit form is given in Appendix. A. Owing to the symmetry of the Kerr space-time, separation of the variable is possible [55]. We take the ansatz

$$\Phi = e^{-i(\omega t - m\varphi)} S_{lm\omega}(\theta) R_{lm\omega}(r) \ . \tag{2.2}$$

Here, the functions $S_{lm\omega}$ and $R_{lm\omega}$ denote the angular and radial mode functions, respectively. The solution is specified by the frequency ω and the angular quantum numbers l and m. The radial mode function satisfies the following differential equation [55]

$$\frac{d^2}{dr_*^2} u_{lm\omega} - V_{\text{eff}}(r_*) u_{lm\omega} = 0 \ , \tag{2.3}$$
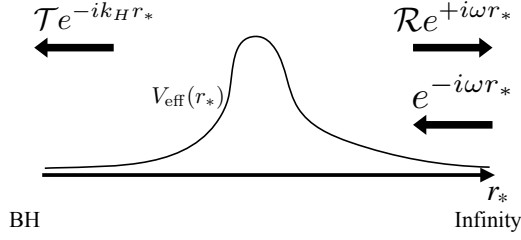
Figure 2.1: Scattering of a massless scalar field by the black hole. The scalar wave with the unit amplitude is coming from infinity and is scattered by the black hole with the transmission and the reflection amplitudes, $\mathcal{T}$ and $\mathcal{R}$. The black solid curve shows the effective potential V_{eff}. Owing to the rotation of the black hole, the radial wave number at infinity and the horizon is different.

where $u_{lm\omega} = \sqrt{r^2 + a^2} R_{lm\omega}$ and r_* is defined by $dr_* = (r^2 + a^2)/\Delta dr$. The definitions of r, a, and Δ are shown in Appendix A. Here, V_{eff} is the effective potential of the wave equation given by

$$V_{\text{eff}} = -\omega^2 - \frac{a^2 m^2 - 4amMr\omega}{(a^2 + r^2)^2} - \frac{\Delta(a^2\omega^2 + \Lambda_{lm}(\omega))}{(a^2 + r^2)^2}$$
$$+ \frac{\Delta(a^2 - 4Mr + 3r^2)}{(a^2 + r^2)^3} - \frac{3\Delta^2 r^2}{(a^2 + r^2)^4} , \tag{2.4}$$

with $\Lambda_{lm}(\omega)$ as a separation constant. The asymptotic form of V_{eff} is

$$V_{\text{eff}} \to \begin{cases} \omega^2 , & (r \to \infty) , \\ k_H^2 , & (r \to r_+) , \end{cases} \tag{2.5}$$

with $k_H = \omega - m\Omega_H$, where $\Omega_H \equiv a/2Mr_+$ is the angular velocity of the horizon.

Suppose that an incident wave comes from infinity ($r = +\infty$) with the unit amplitude. The wave is partially absorbed by the black hole, and the rest is scattered back to infinity (see Fig. 2.1). The mode function in such a situation behaves in the asymptotic region as

$$R_{lm\omega}(r) \to \begin{cases} \mathcal{T} e^{-ik_H r_*} , & (r \to r_+) , \\ e^{-i\omega r_*} + \mathcal{R} e^{+i\omega r_*} , & (r \to \infty) , \end{cases} \tag{2.6}$$

where $\mathcal{T}$ and $\mathcal{R}$ is the transmission and the reflection coefficients, respectively. Even though the precise forms of the coefficients $\mathcal{T}$ and $\mathcal{R}$ are not known, their relation can be obtained by the conservation of the Wronskian

$$W = R_{lm\omega}^* \partial_{r_*} R_{lm\omega} - R_{lm\omega} \partial_{r_*} R_{lm\omega}^* . \tag{2.7}$$

By evaluating the Wronskian at the horizon and infinity, we obtain

$$k_H |\mathcal{T}|^2 = \omega(1 - |\mathcal{R}|^2) . \tag{2.8}$$

Thus, the reflected wave has a larger amplitude than the incident wave, i.e., $|\mathcal{R}| > 1$, when $k_H < 0$, or equivalently when

$$\omega < m\Omega_H . \tag{2.9}$$

This amplification mechanism of the wave is called superradiance [25]. The condition (2.9) is called the *superradiance condition*. When the superradiance condition is satisfied, the energy and angular momentum of the black hole are extracted by the scalar field.

2.1.2 Superradiant instability

Now we consider the case when the scalar field is massive. Because of the mass, the scalar field can be bounded by the gravitational potential of the black hole. Therefore, the scalar field that extracts the energy from the black hole by the superradiance can be reflected back to the black hole, avoiding the escape to infinity. Then, the scalar field experiences the superradiant scattering repeatedly and further extracts the energy of the black hole. Thus, the amplification of the scalar field outside the black hole continually occurs, indicating the existence of instability. In this subsection, we mathematically formulate the instability of a massive scalar field on the Kerr space-time.

The equation of motion of a massive complex scalar field is given by

$$(\Box_g - \mu^2)\Phi = 0 \ . \tag{2.10}$$

In a similar manner as the equation of motion of a massless complex scalar field (2.1), Eq. (2.10) can be decomposed under the ansatz Eq. (2.2). The mode functions obey

$$\frac{1}{\sin\theta}\frac{d}{d\theta}\left(\sin\theta\frac{dS_{lm\omega}}{d\theta}\right) + \left[c^2(\omega)\cos^2\theta - \frac{m^2}{\sin^2\theta}\right]S_{lm\omega} = -\Lambda_{lm}(\omega)S_{lm\omega} \ , \tag{2.11}$$

$$\frac{d}{dr}\left(\Delta\frac{dR_{lm\omega}}{dr}\right) + \left[\frac{K^2(\omega)}{\Delta} - \mu^2r^2 - \lambda_{lm}(\omega)\right]R_{lm\omega} = 0 \ , \tag{2.12}$$

with

$$c^2(\omega) = a^2(\omega^2 - \mu^2) \ , \qquad K(\omega) = (r^2 + a^2)\omega - am \ ,$$
$$\lambda_{lm}(\omega) = -2am\omega + a^2\omega^2 + \Lambda_{lm}(\omega) \ , \tag{2.13}$$

and $\Lambda_{lm}(\omega)$ is the separation constant. Since we are interested in the bounded modes, we can concentrate on the region $|\omega| < \mu$. Under the condition $|\omega| < \mu$, the asymptotic form of $R_{lm\omega}$ is

$$R_{lm\omega}(r) \to \begin{cases} \left(\dfrac{r - r_+}{M}\right)^{-i\frac{2Mr_+}{r_+ - r_-}(\omega - m\Omega_H)} \ , & (r \to r_+) \ , \\ \dfrac{1}{r/M}r^{-\frac{\mu^2 - 2\omega^2}{\sqrt{\mu^2 - \omega^2}}}e^{-\sqrt{\mu^2 - \omega^2}r} \ , & (r \to \infty) \ . \end{cases} \tag{2.14}$$

To show the existence of the instability $\omega_I \equiv \mathrm{Im}\,[\omega] > 0$, we consider the energy-momentum tensor of the free scalar field $T^\mu_{\ \nu}$, which is

$$T^\mu_{\ \nu} = \frac{1}{2}\left(\partial^\mu\Phi\partial_\nu\Phi^* + \partial^\mu\Phi^*\partial_\nu\Phi\right) + \delta^\mu_{\ \nu}\left(-\frac{1}{2}|\partial_\alpha\Phi|^2 - \frac{\mu^2}{2}|\Phi|^2\right) \ . \tag{2.15}$$

Owing to the conservation of $T^\mu_{\ \nu}$, we have

$$(T^\mu_{\ \nu}\xi^\nu_{(t)})_{;\mu} = 0 \ , \tag{2.16}$$

where $\xi^\mu_{(t)} = (1, 0, 0, 0)$ is the timelike killing vector corresponding to the static observers at infinity (see App. A). To consider the fluxes going through the event horizon, it is

convenient to consider in the ingoing Kerr coordinates $(\tilde{t}, r, \theta, \tilde{\varphi})$ (see App. A for the definition). Integrating Eq. (2.16) over $\tilde{t} =$constant surface Σ, we obtain

$$-\frac{\partial}{\partial \tilde{t}} \left(\int_{\Sigma} \sqrt{-\tilde{g}^{00}} \rho^2 \sin\theta dr d\theta d\tilde{\varphi} \; T^{\mu}{}_{\nu} \xi^{\nu} (n_{(\tilde{t})})_{\mu} \right) = \int_{\partial\Sigma} \rho^2 \sin\theta d\theta d\tilde{\varphi} \; T^{\mu}{}_{\nu} \xi^{\nu} (n_{(r)})_{\mu} \; , \quad (2.17)$$

where $(n_{(\tilde{t})})_{\mu} = -\delta^0_{\mu}$ and $(n_{(r)})_{\mu} = -\delta^1_{\mu}$. The right-hand side of Eq, (2.17) corresponds to the energy flux through the boundaries of Σ, at infinity and the event horizon. Since we are considering bounded modes, the flux through the infinity vanishes. The contribution from the event horizon is calculated as

$$(\text{R.H.S.}) = 4\pi M r_+ \omega_R \left(\frac{|\omega|^2}{\omega_R} - m\Omega_H \right) |R_{lm\omega}(r_+)|^2 \; . \quad (2.18)$$

Therefore, energy flux is negative, when

$$\frac{|\omega|^2}{\omega_R} < m\Omega_H \; , \quad (2.19)$$

is satisfied. The condition (2.19) becomes the superradiance condition (2.9), when $\omega_I \ll \omega_R$. Here, ω_R is the real part of the frequency ω. On the other hand, the left-hand side shows the change rate of the energy on Σ. The straightforward calculation shows

$$(\text{L.H.S.}) = 2\omega_I \int_{\Sigma} \sqrt{-\tilde{g}^{00}} \rho^2 \sin\theta dr d\theta d\tilde{\varphi} \; T^0{}_0 \; . \quad (2.20)$$

Combining Eqs. (2.17), (2.18) and (2.20), we obtain

$$2\omega_I E = 4\pi M r_+ |R_{lm\omega}(r_+)|^2 \omega_R \left(m\Omega_H - \frac{|\omega|^2}{\omega_R} \right) \; , \quad (2.21)$$

with

$$E = \int_{\Sigma} \sqrt{-\tilde{g}^{00}} \rho^2 \sin\theta dr d\theta d\tilde{\varphi} \; T^0{}_0 \; . \quad (2.22)$$

Equation (2.21) shows that the mode is unstable ($\omega_I > 0$), when both the condition (2.19) and $E > 0$ hold. Since the condition (2.19) is similar to the superradiance condition (2.9), this instability is called superradiant instability. From the derivation in this subsection, the inverse of the instability timescale ω_I and the energy stored in the unstable mode determines the energy extraction rate from the black hole.

2.2 Configuration of the axion cloud

The previous section shows that a massive scalar field on a Kerr space time can possess unstable modes. To show the presence of unstable modes, here we numerically solve the radial equation (2.12) under the boundary condition (2.14). In this thesis, we use the continued fraction method presented in [30] to solve these differential equations. The detail of the numerical method is reviewed in appendix B.

The pair of boundary conditions (2.14) forces the spectrum of the frequency ω to be discrete. Following the spectrum of the Hydrogen atom, we label the spectrum by the
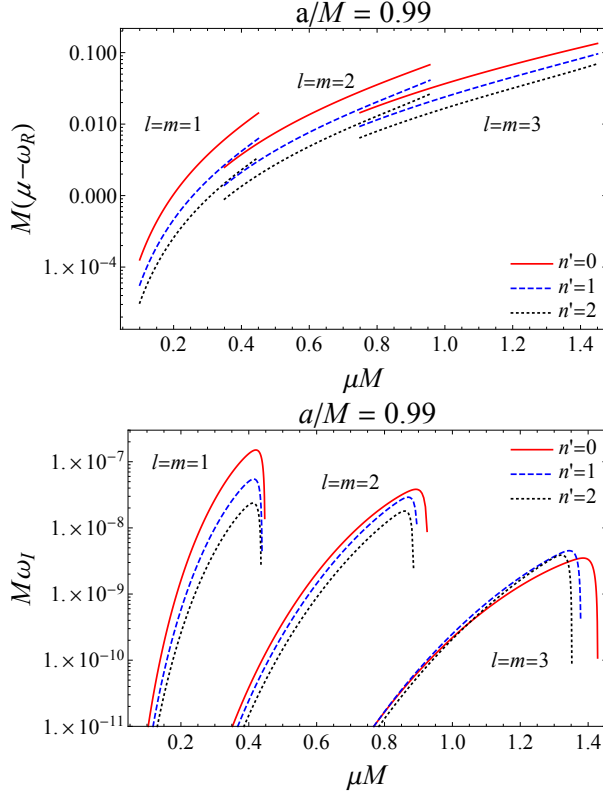
Figure 2.2: (Top) The real part of the frequencies $\omega^{(n)}$. The red solid, blue dashed, and black dotted curves correspond to $n = l + 1 + n'$, with $n' = 0, 1$, and 2, respectively. The spin of the central BH is set to $a/M = 0.99$. (Bottom) Similar plot for the imaginary part of the frequencies $\omega^{(n)}$.

principal quantum number $n = n' + l + 1, n' = 0, 1, 2, \ldots$. We express the mode function with the principal quantum number n as

$$\Phi_{nlm} = e^{-i(\omega^{(nlm)}t - m\varphi)} S_{lm\omega^{(nlm)}}(\theta) R_{lm\omega^{(nlm)}}(r) . \tag{2.23}$$

We refer to the mode with the smallest n as the *fundamental mode* for each pair of l and m, and modes with larger ones as *overtone modes*.

In Fig. 2.2, we show the real and the imaginary part of $\omega^{(nlm)}$. First, we observe that the real part of the frequency satisfies $\omega_R \lesssim \mu$. In addition, ω_R gets closer to μ as n increases. Another feature is that , for $\mu M \ll 1$, the spectrum becomes almost identical to the case of a Hydrogen atom, which is independent of l and m, as [28]

$$\omega_R^{(nlm)} \sim \mu \left(1 - \frac{(\mu M)^2}{2n^2} \right) . \tag{2.24}$$

The imaginary part of the frequency is much smaller than the real part. In particular, ω_I is significantly reduced as μ is decreased. For a fixed axion mass, the fundamental mode with the smallest $l(= m)$ that satisfies the superradiance condition has the largest ω_I in most of the parameter region of μM. The ω_I of overtones with the same orbital angular momentum l is smaller by a factor of order unity, where ω_I is significantly suppressed for larger l. Recall that ω_I corresponds to the energy extraction rate from the black hole. The scalar field must tunnel through the angular momentum barrier to extract the energy from the black hole. The angular momentum barrier is higher for the larger l,
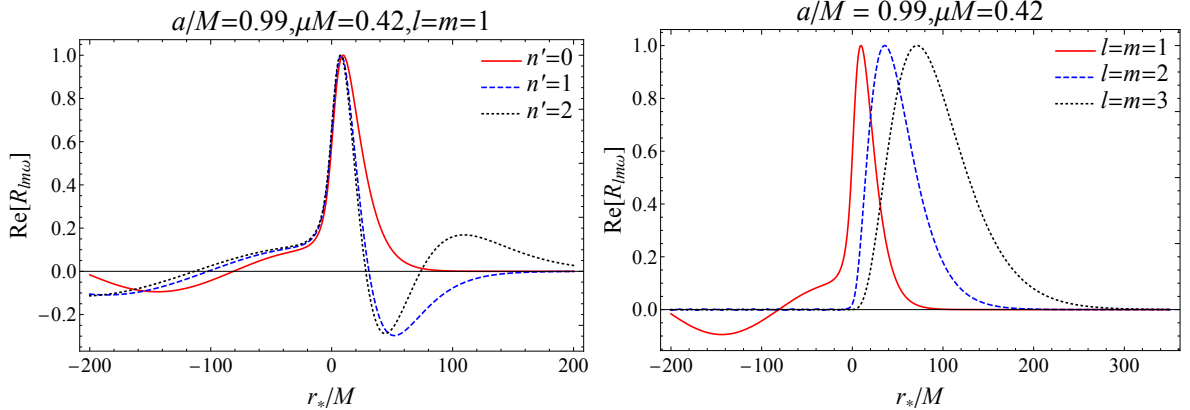
13

Figure 2.3: (Left) The real part of the radial mode function $R_{lm\omega}$. The red solid, blue dashed, and black dotted curves correspond to $n = l + 1 + n'$, with $n' = 0, 1$, and 2, respectively. The angular quantum numbers are set to $l = m = 1$, while the axion mass to $\mu M = 0.42$ and the spin of the central BH to $a/M = 0.99$. The mode functions are normalized to peak amplitude of unity. (Right) The same figure but for fundamental modes with $l = m = 1$, $l = m = 2$, and $l = m = 3$, instead of the overtones of the $l = m = 1$ mode.

which explains the suppression of ω_I for large l. The suppression for large l can also be seen by the approximate formula

$$\omega_I^{(nlm)} \sim \frac{2r_+}{M}(\mu M)^{4l+5}(-\mu + m\Omega_H)\frac{2^{4l+2}(2l+n+1)!}{n!(l+n+1)^{2l+4}}$$

$$\times \left(\frac{l!}{(2l)!(2l+1)!}\right)^2 \prod_{j=1}^{l}\left(j^2\left(1 - \frac{a^2}{M^2}\right) + 4r_+^2(\mu - m\Omega_H)^2\right) , \quad (2.25)$$

for $\mu M \ll 1$ [28].

Next, we show the real part of the radial mode functions in Fig. 2.3. We observe that the behavior of the mode functions away from the event horizon is similar to the wave function of the Hydrogen atom. As the principal quantum number increases, the number of nodes in the far region ($r_* \gtrsim 0$) increases. In addition, the mode functions get more widely extended. For larger l, the mode functions become more extended to the far region. This is because the angular momentum barrier extends to further regions for larger l. The larger height of the angular momentum barrier for large l also explains the significant suppression of the mode functions with larger l near the horizon.

To summarize, the unstable bounded modes satisfy the superradiant condition

$$\omega_R^{(nlm)} < m\Omega_H , \quad (2.26)$$

and evolve adiabatically,

$$\omega_I^{(nlm)} \ll \omega_R^{(nlm)} . \quad (2.27)$$

Even if the instability time scale ω_I^{-1} is much longer than the dynamical timescale ω_R^{-1}, it is much shorter the age of the universe [17]. For example, the time scale of the instability with $a/M = 0.99$ and $\mu M \sim 0.42$, which gives almost the shortest instability time scale [30], is

$$\frac{1}{\omega_I} \sim 1\text{min}\left(\frac{M}{M_\odot}\right) , \quad (2.28)$$

which is much shorter than the age of the universe.

Thus, the condensate of the axion will spontaneously form by the superradiant instability. As already mentioned, we call an axion condensate formed by the single unstable mode an axion cloud. Since the axion is a real scalar field, the configuration of the axion cloud is given by

$$\phi_{nlm} = \Phi_{nlm} + \Phi^*_{nlm} \ . \tag{2.29}$$

In the following, we normalize the radial mode function such that the energy of ϕ_{nlm} on the constant t surface satisfies,

$$\int dr \, d\cos\theta \, d\varphi \, (r^2 + a^2 \cos^2\theta)\sqrt{g^{tt}}T_{\mu\nu}(\phi_{nlm})\xi^\mu_{(t)}n^\nu_{(t)} = F_a^2 M \ , \tag{2.30}$$

where F_a is the decay constant of the axion, M is the mass of the black hole and

$$T_{\mu\nu}(\phi_{nlm}) = \partial_\mu\phi_{nlm}\partial_\nu\phi_{nlm} + g_{\mu\nu}\left(-\frac{1}{2}(\partial\phi_{nlm})^2 - V(\phi_{nlm})\right) \ . \tag{2.31}$$

Here, $V(\phi)$ is the potential of the axion. In the linearized approximation adopted in this section, it is given by

$$V(\phi) = \frac{\mu^2}{2}\phi^2 \ . \tag{2.32}$$

2.3 Observational Signature of the axion cloud

We showed that an axion spontaneously forms a macroscopic condensate around a rotating black hole. In this section, we briefly explain the possible observational signals of the axion condensate.

2.3.1 Spin-down of the BH

The axion condensate extracts the angular momentum of the black hole by the superradiance. This angular momentum extraction can be observed as the almost depleted region on the black hole spin and mass.

Let us demonstrate how the depleted region can be obtained, following Ref. [17]. For the axion to extract the black hole angular momentum, it must have an unstable mode, which corresponds to the condition (2.26) or

$$\omega_R^{(nlm)}(\mu, M, a) < m\Omega_H = m\frac{a/M}{2(1 + \sqrt{1 - (a/M)^2})} \ . \tag{2.33}$$

Another condition is that angular momentum extraction must be fast enough. For example, the spin-down of the black hole cannot be observed if the time scale of the angular momentum extraction is longer than the age of the Universe. Therefore,

$$\omega_I^{(nlm)}(\mu, M, a) > 75\tau_{uni}^{-1} \ , \tag{2.34}$$

must be satisfied. Here, $\tau_{uni} \sim 10\mathrm{Gyr}$ is the age of the Universe and the factor 75 corresponds to the required e-folding number for the axion condensate to have the angular
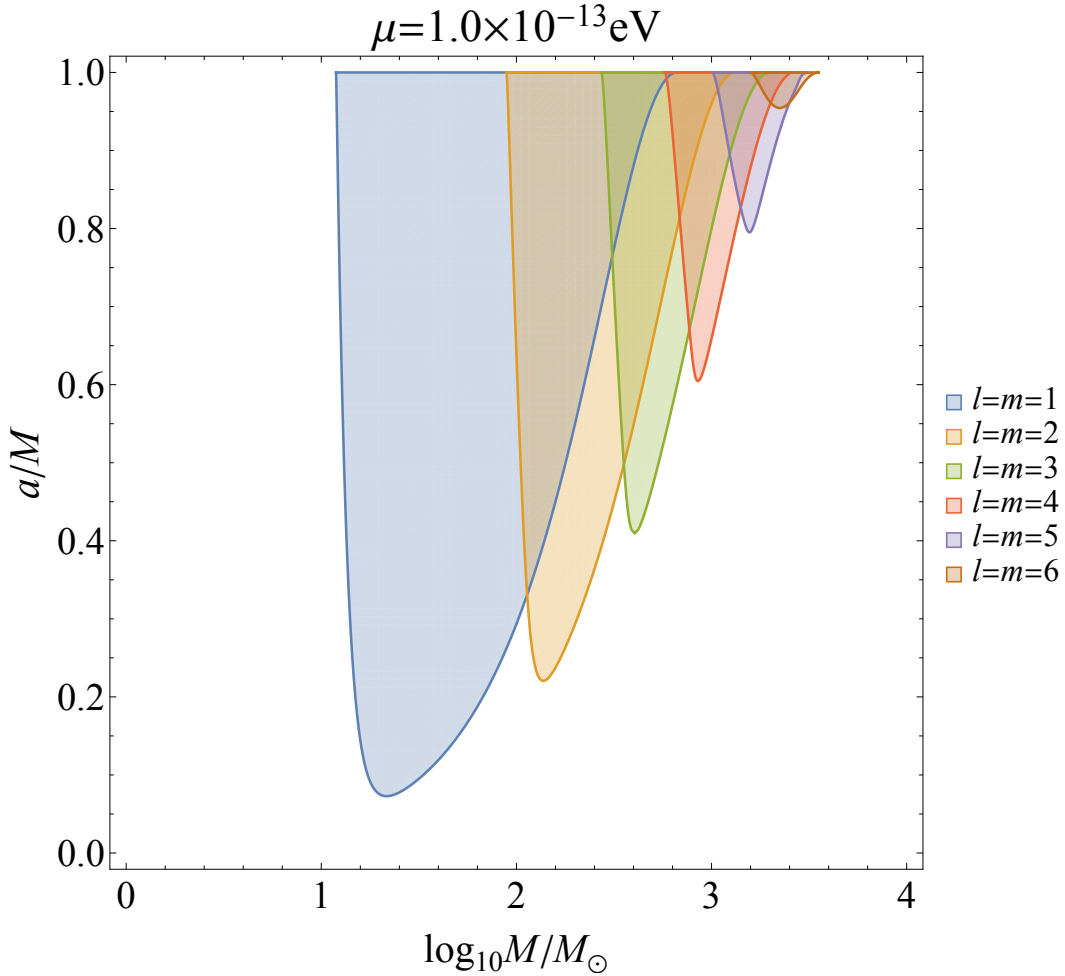
Figure 2.4: Each region shows the value of the BH spin and mass cannot exist under the presence of the axion with $\mu = 10^{-13}$eV. We show the region for $l = m = 1, 2, 3, 4, 5$, and 6.

momentum comparable to the black hole. We show the region which satisfies these inequalities in Fig. 2.4, using the non-relativistic approximation ($\mu M \ll 1$) for $\omega_{R,I}^{(nlm)}$ (see Eqs. (2.24) and (2.25)) and setting $\mu = 10^{-13}$eV. Roughly speaking, if the black hole in the shaded region is observed, we can rule out the axion with mass $\mu = 10^{-13}$eV. Moreover, as we change the mass of the axion, the shaded region shifts horizontally. In this way, one can constrain the axion in various mass ranges.

However, the above argument is premature to be applied to give a constraint on the mass of the axion. Various effects may change the shape of the excluded region. For example, environmental effect, such as the spin-up of the black hole by the accretion, offset the shape of the excluded region [31]. In addition, we assumed that the evolution of the axion condensate is described by the linear approximation, even if the condensate grows to a large amplitude. When the amplitude is large, the non-linear effect of the self-interaction can alter the evolution of the condensate significantly. Therefore, to constrain the axion by the black hole spin measurement, the precise evolution of the axion under various effects must be known.

2.3.2 Continuos gravitational wave emission

Since the axion condensate can have a significant mass, it can be a source of gravitational waves. Let us consider the case when the condensate is a superposition of two different superradiant modes

$$\phi = \sqrt{E_1}\phi_1 + \sqrt{E_2}\phi_2 \ , \tag{2.35}$$

where $\phi_1 = \phi_{n_1 l_1 m_1}$ and $\phi_2 = \phi_{n_2 l_2 m_2}$. For simplicity, we assume $m_1 \leq m_2$ and $\omega_1 < \omega_2$. Note that ϕ_1 and ϕ_2 are normalized to have unit energy in the unit of $F_a^2 M$. Thus E_1 and E_2 correspond to the energies of the cloud 1 and the cloud 2.

We consider gravitational waves sourced by the condensate. Since the energy-momentum tensor of the scalar field is quadratic in ϕ, it is made from the terms such as

$$\partial_\mu \phi_1 \partial_\nu \phi_1 \ , \qquad\qquad \partial_\mu \phi_2 \partial_\nu \phi_2 \ , \qquad\qquad \partial_\mu \phi_1 \partial_\nu \phi_2 \ .$$

Therefore, the t- and φ- dependence of each term in the energy-momentum tensor takes the form of $e^{-i(\omega t - m\varphi)}$. The terms which give the dominant contribution to gravitational waves are $(\omega, m) = (2\omega_1, 2m_1)$ and/or $(\omega_2 - \omega_1, m_2 - m_1)$, since they have smaller $|m|$ than the other term. These two contributions are called a pair annihilation signal and a level transition signal, respectively.

For $l_1 = m_1 = 1, n_1 = 2$ and $l_2 = m_2 = 2, n_2 = 3$ case under $\mu M \ll 1$, the amplitude of these gravitational waves can be calculated as [17, 42]

$$h_{\text{gw}}^{\text{ann}} \sim 5.6 \times 10^{-18} (\mu M)^6 \left(\frac{1\text{kpc}}{d}\right) \left(\frac{M}{M_\odot}\right) \frac{E_1}{M} \ , \tag{2.36}$$

$$h_{\text{gw}}^{\text{trans}} \sim 2.4 \times 10^{-18} (\mu M)^3 \left(\frac{1\text{kpc}}{d}\right) \left(\frac{M}{M_\odot}\right) \sqrt{\frac{E_1}{M}\frac{E_2}{M}} \ . \tag{2.37}$$

Their frequencies are approximated as

$$\omega^{\text{ann}} \sim 4.0 \times 10^2 (\mu M) \left(\frac{M_\odot}{M}\right) \text{kHz} \ , \tag{2.38}$$

$$\omega^{\text{trans}} \sim 2.8 \times 10 (\mu M)^3 \left(\frac{M_\odot}{M}\right) \text{kHz} \ . \tag{2.39}$$

Since the frequency of the transition signal is given by the difference between the frequencies of the two modes, it is much smaller than that of the annihilation signal in general. Simultaneous detection of these continuous waves would be strong evidence of the axion.

Nonetheless, it is non-trivial whether the condensate can grow to a significantly large amplitude, when nonlinear effects such as the self-interaction of the axion are considered. For example, the energy dissipation due to the self-interaction is essential when the cloud becomes dense [17]. In addition, self-interaction can significantly alter the evolution of the condensate and cause another gravitational wave emission, as we explain in the following subsection.

2.3.3 Bosenova

Other than the continuous gravitational waves, the burst of gravitational waves can be emitted when one considers the self-interaction of the axion. Owing to the attractive

nature of the self-interaction[1], the condensate can collapse when it becomes dense. Since the mass of the condensate can be a few % of the central black hole, a sizable burst of gravitational waves can be expected. The collapse of the condensate associated with the burst of gravitational waves is named *bosenova*, in analogy with the explosion of the Bose-Einstein condensate in cold-atom experiments [56].

The precise non-linear dynamics of the condensate during the collapse must be understood to estimate the amplitude of the burst-like gravitational waves. The occurrence of the bosenova has been suggested by the dynamical simulation in Ref. [37, 39]. The amplitude of the gravitational waves at a distance of a kpc is estimated as [32]

$$h \sim 10^{-21} \left(\frac{\epsilon}{0.05} \right) \left(\frac{16}{c_{\mathrm{bn}}} \right)^2 \left(\frac{M}{10M_\odot} \right) \left(\frac{\mu M}{0.4} \right) \left(\frac{F_a}{6 \times 10^{16}\mathrm{GeV}} \right) \, , \qquad (2.40)$$

where ϵ is the fraction of the condensate falling into the black hole, c_{bn} is the ratio of the duration of the collapse and the light crossing time of the condensate ($\sim M/(\mu M)^2$ for $\mu M \ll 1$), and F_a is the decay constant of the axion. The quantities $\epsilon \sim 0.05$ and $c_{\mathrm{bn}} \sim 16$ is obtained from the numerical simulation. The amplitude is large enough for the advanced LIGO to detect.

However, it is too early to conclude the bosenova occurrence because of the uncertainty of the initial condition in the dynamical simulation. Since there is a large discrepancy in the dynamical time scale and the instability time scale (see Sec. 2.2), performing the dynamical simulation for a sufficiently long time is difficult. Thus, dynamical simulation cannot track the whole evolution of the condensate, starting from such a small amplitude as seeded by quantum fluctuation to a sufficiently large amplitude enough to make bosenova happen. In Ref. [37, 39], the initial condition is given by scaling a linearized solution. However, such a prescription is difficult to justify, since the distribution of the condensate should gradually change from the linear one as it evolves under the effect of the self-interaction. Therefore, to simulate the bosenova in a realistic situation, we need a more sophisticated calculation, including the effects of the self-interaction.

---

[1]If one considers cosine-type potential, the leading non-linear term is attractive.

Chapter 3

Perturbative Approach to the self-interacting axion condensate

In the previous section, we reviewed that the self-interaction may cause the observationally interesting phenomenon called bosenova. To further investigate such a possibility, the evolution under the effect of the self-interaction starting from a small amplitude must be understood precisely. For this purpose, we first study the early stage of evolution, where the amplitude is still small. In such a regime, the self-interaction can be treated perturbatively. In this chapter, we formulate a perturbative method to track the evolution, based on our paper [52] and [53].

In the rest of this thesis, we adopt

$$
S = F_a^2 \int d^4x \sqrt{-g} \left\{ -\frac{1}{2} g^{\mu\nu} \partial_\mu \phi \partial_\nu \phi - V(\phi) \right\} , \tag{3.1}
$$

as the action of the axion, with the potential

$$
V(\phi) = \mu^2 (1 - \cos \phi) . \tag{3.2}
$$

Note that we normalize the axion field by the decay constant F_a to make ϕ dimensionless. Then, the equation of motion of the axion is given by the sine-Gordon equation on the Kerr space-time

$$
\Box_g \phi - \mu^2 \sin \phi = 0 , \tag{3.3}
$$

which is independent of F_a.

3.1 Formulation

In the rest of this chapter, we solve nonlinear equation (3.3) perturbatively. Since we are interested in the regime where the amplitude is small, we approximate Eq. (3.3) as

$$
(\Box_g - \mu^2)\phi = -\lambda \phi^3 , \tag{3.4}
$$

and perturbatively expand the axion field as

$$
\phi = \phi^{(0)} + \lambda \phi^{(1)} + \cdots , \tag{3.5}
$$

where $\lambda = \dfrac{\mu^2}{3!}$. The leading order and the next of Eq. (3.4) are

$$(\Box_g - \mu^2)\phi^{(0)} = 0 \ , \tag{3.6}$$

$$(\Box_g - \mu^2)\phi^{(1)} = -\left(\phi^{(0)}\right)^3 \ . \tag{3.7}$$

The solution to the zeroth order equation (3.6) is ϕ_{nlm}, given in Eq. (2.29). We take $\phi^{(0)}$ to be a superposition of two different clouds $\phi_1 = \phi_{n_1 l_1 m_1}$ and $\phi_2 = \phi_{n_2 l_2 m_2}$:

$$\phi^{(0)} = \sqrt{E_1}\phi_1 + \sqrt{E_2}\phi_2 \ . \tag{3.8}$$

Same as before, we take the normalization of $\phi_{l_i m_i \omega_i}$ such that the energy of the i-th cloud on the constant t surface is equal to 1, in the unit of $F_a^2 M$. Thus, E_1 and E_2 correspond to the energies of the cloud 1 and the cloud 2 in the unit of $F_a^2 M$, respectively.

We solve the first order equation (3.7) by the Green's function method. The retarded Green's function G_{ret} satisfies

$$(\Box_g - \mu^2)G_{\mathrm{ret}}(x, x') = \frac{1}{\sqrt{-g(x)}}\delta^{(4)}(x - x') \ . \tag{3.9}$$

We decompose the Green's function as

$$G_{\mathrm{ret}}(x, x') = \frac{1}{2\pi}\sum_{l,m}\int_C \frac{d\omega}{2\pi} e^{-i\omega(t-t')}e^{im(\varphi-\varphi')}S_{lm\omega}(\theta)S_{lm\omega}(\theta')G_{lm\omega}(r, r') \ , \tag{3.10}$$

where

$$G_{lm\omega}(r, r') = \frac{1}{W_{lm}(\omega)}\left(R_{lm\omega}^{\mathrm{in}}(r)R_{lm\omega}^{\mathrm{up}}(r')\theta(r' - r) + R_{lm\omega}^{\mathrm{in}}(r')R_{lm\omega}^{\mathrm{up}}(r)\theta(r - r')\right) \ . \tag{3.11}$$

Here, the functions $R_{lm\omega}^{\mathrm{in}}$ and $R_{lm\omega}^{\mathrm{up}}$ are the solutions to the radial equation of motion (2.12) satisfying the boundary conditions

$$R_{lm\omega}^{\mathrm{in}} \longrightarrow \begin{cases} e^{-i(\omega - m\Omega_H)r_*} \ , & (r \to r_+) \\[2mm] A_{\mathrm{in}}(\omega)r^{+i\frac{\mu^2 - 2\omega^2}{\sqrt{\omega^2 - \mu^2}}}(\omega)\dfrac{e^{-i\sqrt{\omega^2 - \mu^2}r}}{r} \\[3mm] \qquad + A_{\mathrm{out}}(\omega)r^{-i\frac{\mu^2 - 2\omega^2}{\sqrt{\omega^2 - \mu^2}}}\dfrac{e^{+i\sqrt{\omega^2 - \mu^2}r}}{r} \ , & (r \to +\infty) \end{cases} \tag{3.12a}$$

$$R_{lm\omega}^{\mathrm{up}} \longrightarrow \begin{cases} B_{\mathrm{in}}(\omega)e^{-i(\omega - m\Omega_H)r_*} + B_{\mathrm{out}}(\omega)e^{+i(\omega - m\Omega_H)r_*} \ , & (r \to r_+) \\[2mm] r^{-i\frac{\mu^2 - 2\omega^2}{\sqrt{\omega^2 - \mu^2}}}\dfrac{e^{+i\sqrt{\omega^2 - \mu^2}r}}{r/M} \ , & (r \to +\infty) \end{cases} \tag{3.12b}$$

We choose the branch such that $\mathrm{Im}\left[\sqrt{\omega^2 - \mu^2}\right] > 0$ for $\omega^2 < \mu^2$. This choice implies the boundary conditions at infinity for $\omega^2 < \mu^2$ are

$$R_{lm\omega}^{\mathrm{in}} \longrightarrow A_{\mathrm{in}}(\omega)r^{+\frac{\mu^2 - 2\omega^2}{\sqrt{\mu^2 - \omega^2}}}\dfrac{e^{+\sqrt{\mu^2 - \omega^2}r_*}}{r}$$

$$\qquad + A_{\mathrm{out}}(\omega)r^{-\frac{\mu^2 - 2\omega^2}{\sqrt{\mu^2 - \omega^2}}}\dfrac{e^{-\sqrt{\mu^2 - \mu^2}r_*}}{r} \ , \tag{3.13}$$

$$R_{lm\omega}^{\mathrm{up}} \longrightarrow r^{+\frac{\mu^2 - 2\omega^2}{\sqrt{\mu^2 - \omega^2}}}\dfrac{e^{-\sqrt{\mu^2 - \omega^2}r_*}}{r} \ . \tag{3.14}$$
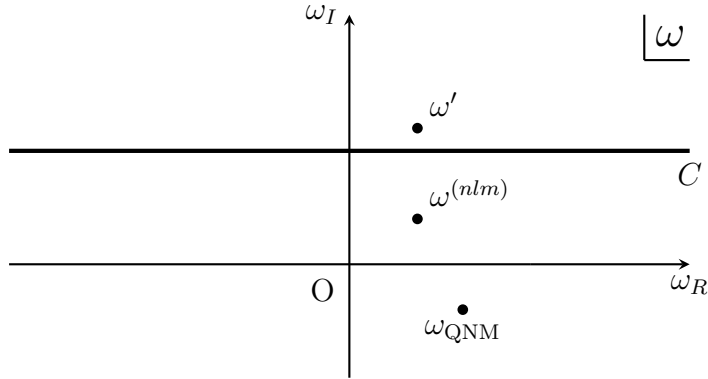
Figure 3.1: The integration contour C in Eq. (3.10) on the complex ω plane. The frequencies $\omega^{(nlm)}$ and ω_{QNM} are the frequencies of the superradiant unstable modes and the quasi-normal modes, both of which are zero points of the Wronskian. The frequency ω' corresponds to the frequency of the source in Eq. (3.7).

These boundary conditions imply that the in-mode (up-mode) solution $R_{lm\omega}^{\mathrm{in}}$ ($R_{lm\omega}^{\mathrm{up}}$) is purely ingoing (outgoing) at the event horizon (infinity). See Appendix B for the numerical construction of these mode functions.

The function $W_{lm}(\omega)$ in Eq. (3.11) is the Wronskian defined by

$$W_{lm}(\omega) \equiv \Delta \left(R_{lm\omega}^{\mathrm{in}} \partial_r R_{lm\omega}^{\mathrm{up}} - R_{lm\omega}^{\mathrm{up}} \partial_r R_{lm\omega}^{\mathrm{in}} \right) \ . \tag{3.15}$$

With the boundary conditions (3.12), the Wronskian is evaluated as

$$W_{lm}(\omega) = 2i\sqrt{\omega^2 - \mu^2} A_{\mathrm{in}}(\omega) \ . \tag{3.16}$$

We choose the integration contour C on the complex ω plane to pass above all zero points of the Wronskian $W_{lm}(\omega)$ (see Fig. 3.1). Note that frequencies of clouds, $\omega^{(nlm)}$, are the zero points of the Wronskian because the boundary condition of the cloud (see Eq. (2.14)) implies $A_{\mathrm{in}}(\omega^{(nlm)}) = 0$. This choice of the contour C corresponds to taking the retarded boundary condition.

Using the Green's function, the formal solution to the first order equation (3.7) is

$$\phi^{(1)} = -\int \sqrt{-g(x')} \, d^4x' \, G_{\mathrm{ret}}(x, x') s^{(1)}(x') + (\text{homogeneous solution}) \ , \tag{3.17}$$

where $s^{(1)}$ is the source term in (3.7) given by

$$s^{(1)} = -\left(E_1^{3/2} \phi_1^3 + E_2^{3/2} \phi_2^3 + 3E_1 E_2^{1/2} \phi_1^2 \phi_2 + 3E_1^{1/2} E_2 \phi_1 \phi_2^2 \right) \ , \tag{3.18}$$

and we added an arbitrary homogeneous solution since the first order equation has ambiguity in their choice. Later in Sec. 3.3, we utilize this ambiguity to improve the perturbative expansion. Since each term is composed of a product of ϕ_i, its (t', φ')-dependence is factorized as $\propto e^{-i(\omega't' - m'\varphi')}$, with some (ω', m'). Now, recall the Green's function in the form of spectral decompotsition (3.10). The (t', φ')-dependence of $\phi^{(1)}$ also takes the form $e^{-i(\omega t - m\varphi)}$.

The integration over φ' gives $\delta_{mm'}$. Therefore, the summation over m picks up $m = m'$. The integration contour C in Fig. 3.1 is taken such that both t' and ω integrals converge.

Then, we can exchange their order and perform the integration with respect to t' first. The integration over t' gives

$$e^{-i\omega t} \int_{-\infty}^{t} dt' \, e^{i(\omega - \omega')t'} = \frac{e^{-i\omega' t}}{i(\omega - \omega')} \; . \tag{3.19}$$

Then, the integral over ω takes form

$$\int_{C} \frac{d\omega}{2\pi i} \frac{e^{-i\omega' t}}{\omega - \omega'} S_{lm\omega}(\theta) S_{lm\omega}(\theta') G_{lm\omega}(r, r') s^{(1)}_{\omega' m'}(r', \theta') \; , \tag{3.20}$$

where $s^{(1)}_{\omega' m'}$ is the coefficient of the $e^{-i(\omega t' - m'\varphi)}$ component in the source $s^{(1)}$. Taking into account $1/\omega$ factor in the inverse of the Wronskian, the integrand decays faster than $|\omega|^{-2}$ at large $|\omega|$, if the growth of the mode functions $R_{lm\omega}$ and $S_{lm\omega}$ as $|\omega| \to \infty$ is slower than $|\omega|^{0}$.

Now, we deform the integration contour C to the one composed of a small circle around the pole at $\omega = \omega'$ and a large semi-circle in the upper half-plane. The integral at a large semi-circle vanishes since the integrand drops as fast as $\propto |\omega|^{-2}$. Therefore, we only need to care about the poles at $\omega = \omega'$. After the above procedure, the first order solution (3.17) takes

$$\phi^{(1)} = - \sum_{(\omega', m')} \sum_{l \geq m'} S_{lm'\omega'}(\theta) e^{-i(\omega' t + m'\varphi)}$$
$$\times \int dr' d\theta' \, (r'^2 + a^2 \cos^2 \theta') S_{lm'\omega'}(\theta') G_{lm'\omega'}(r, r') s^{(1)}_{\omega' m'}(r', \theta')$$
$$+ \text{(homogeneous solution)} \; . \tag{3.21}$$

Thus, after identifying all possible (ω', m') in the source term, the first order solution is obtained by r' and θ' integration through Eq. (3.21).

Let us identify (ω', m') contained in $s^{(1)}$ and classify them by the superradiance condition (2.26), the boundedness $|\omega| < \mu$, and the size of the wavelength compared to the radial extension of the cloud $r_c \sim M/(\mu M)^2$.[1] The third condition determines the suppression of the r' integration in Eq. (3.21). For concreteness, we work with $l_1 = m_1 = 1, n_1 = 2$, and $l_2 = m_2 = 2, n_2 = 3$, the fundamental modes of the lowest and second lowest multipoles[2]. Note that ϕ is real. Therefore, the term with $(-\omega'^*, -m')$ always appear if the term with (ω', m') exists. We abbreviated the former in the following classification of (ω', m'), since it is just the complex conjugate of the latter.

The possible combinations of (ω', m') are summarized and classified in Table 3.1. The property of each class is the followings:

High frequency radiation

These modes are unbounded and escape to infinity. Thus, The modes in this class cause the dissipation of the condensate. However, the energy dissipation is suppressed because the wavelengths are much shorter than the spatial extension of the

---

[1]This approximation is valid as long as $\mu M \lesssim 1$ and the deformation of the condensate from its linear configuration can be neglected.

[2]We take the second mode not to be a $l = m = 1$ overtone which has a more significant growth rate than the $l = m = 2$ modes since $l = m = 1$ overtones turn out to decay in the two mode approximation adopted in this section. This point will be discussed in Sec. 5.2.

Table 3.1: Classification of (ω', m') contained in $s^{(1)}$ based on the superradiance condition, the boundedness, and the size of the wavelength compared to the radial extension of the cloud r_c.

Class	(ω', m')	Superradiance condition	Boundedness	Wavelength
High frequency radiation	$(3\omega_1, 3), (3\omega_2, 6),$ $(2\omega_1 + \omega_2, 4),$ $(\omega_1 + 2\omega_2, 5)$	Superradiant	Unbound	$\ll r_c$
Low frequency radiation	$(2\omega_2 - \omega_1^*, 3)$	Superradiant	Unbound	$\sim r_c$
Non-superradiant dissipative mode	$(2\omega_1 - \omega_2^*, 0)$	Non-superradiant	Bound	$\sim r_c$
Superradiant bounded mode	$(2\omega_1 - \omega_1^*, 1),$ $(2\omega_2 - \omega_2^*, 2),$ $(\omega_1 + \omega_2 - \omega_2^*, 1),$ $(\omega_2 + \omega_1 - \omega_1^*, 2)$	Superradiant	Bound	$\sim r_c$

cloud. In fact, we will show that the energy dissipation through these modes is much slower than the superradiant instability as long as the self-interaction can be treated perturbatively in Chapter 4. Thus, these modes cannot terminate the growth of the cloud, and we neglect them in this section.

Low frequency radiation

In a similar manner to the high frequency radiation, the mode in this class also satisfies $\mathrm{Re}\,[\omega'] > \mu$, thus escapes to infinity. Unlike in the case of the high frequency radiation, its wavelength ($\sim 1/\mu(\mu M)$) becomes comparable to the size of the cloud. Thus, the energy dissipation can be large enough to be relevant for the saturation of the superradiant instability [42].

Non-superradiant dissipative mode

This excited mode is bounded, *i.e.*, $\omega' < \mu$. Thus, it does not contribute to the energy dissipation to infinity. However, this mode cannot satisfy the superradiance condition (2.26) because $m' = 0$. Such a non-superradiant excitation contributes to positive energy flux to the horizon, which means the energy dissipation to the BH.

Superradiant bounded mode

These excited modes have almost the same ω' (the difference is at most $\mathcal{O}(\omega_{1,I})$, which is small) and the strictly same m' as those of the superradiant modes in the zeroth order solution. Therefore, these modes are both bounded and superradiant. In Sec. 3.3, we show that these modes contribute to accelerate the superradiant instability. We refer to these modes as superradiant bounded modes.

In the followings, we separately deal with these modes and calculate the contribution on the time evolution of the condensate.

3.2 Energy dissipation

First, we treat the source terms corresponding to the low frequency radiation and the non-superradiant dissipative modes. For these modes, $s^{(1)}_{\omega'm'}$ is given by

$$s_{\omega_0 0} = 3E_1 \sqrt{E_2} R_1(r')^2 R_2^*(r') S_1(\theta')^2 S_2^*(\theta') \ , \tag{3.22}$$

$$s_{\omega_3 3} = 3\sqrt{E_1} E_2 R_1^*(r') R_2(r')^2 S_1^*(\theta') S_2(\theta')^2 \ . \tag{3.23}$$

Here, we introduce $\omega_0 = 2\omega_1 - \omega_2^*$ and $\omega_3 = 2\omega_2 - \omega_1^*$. According to Eq. (3.21), the first order solution contains terms with

$$\phi^{(1)} \supset -3E_1\sqrt{E_2} e^{-i\omega_0 t} \sum_l S_{l0\omega_0}(\theta) \int dr'd\theta' \, (r'^2 + a^2 \cos^2\theta') S_{l0\omega_0}(\theta')$$

$$\times \, G_{l0\omega_0}(r,r') R_1(r')^2 R_2^*(r') S_1(\theta')^2 S_2^*(\theta')$$

$$- 3\sqrt{E_1} E_2 e^{-i\omega_3 t + 3\varphi} \sum_l S_{l3\omega_3}(\theta) \int dr'd\theta' \, (r'^2 + a^2 \cos^2\theta')$$

$$\times \, S_{l3\omega_3}(\theta') G_{l3\omega_3}(r,r') R_1(r')^* R_2(r')^2 S_1(\theta')^* S_2(\theta')^2 \ . \tag{3.24}$$

We consider the long-term effect of dissipation due to these modes by promoting E_1 and E_2 to time-dependent variables. Using the relation between the energy E and the angular momentum J of a cloud with (ω, m), [3]

$$J = \frac{m}{\omega} E \ , \tag{3.25}$$

the energy and the angular momentum conservation laws lead to

$$\frac{dE_1}{dt} + \frac{dE_2}{dt} = -F^E_{\text{tot}} \ , \tag{3.26}$$

$$\frac{m_1}{\omega_{1,R}} \frac{dE_1}{dt} + \frac{m_2}{\omega_{2,R}} \frac{dE_2}{dt} = -F^J_{\text{tot}} \ . \tag{3.27}$$

Here, F^E_{tot} and F^J_{tot} are, respectively, the net outgoing energy and angular momentum fluxes evaluated at the boundaries substituting $\phi = \phi^{(0)} + \lambda\phi^{(1)}$.

The energy fluxes at the boundaries, $F_{\mathcal{H}^+}$ from the event horizon and $F_{\mathcal{I}^+}$ from infinity, are given by

$$F_{\mathcal{H}^+} = \int d\cos\theta d\varphi \, 2Mr_+ T_{\mu\nu}(\phi)\xi^\mu_{(t)} l^\nu|_{r=r_+} \ , \tag{3.28}$$

$$F_{\mathcal{I}^+} = \int d\cos\theta d\varphi \, (r^2 + a^2\cos^2\theta)\sqrt{g^{rr}} T_{\mu\nu}(\phi)\xi^\mu_{(t)} n^\nu_{(r)}|_{r\to\infty} \ . \tag{3.29}$$

Here, l^μ is the outgoing null vector specified by $l^\mu = \frac{1}{2}(1, \Delta/(r^2+a^2), 0, a/(r^2+a^2))$ [22], and $n^\mu_{(r)}$ is the outward-pointing unit vector normal to the $r =$ constant surface. The angular momentum flux can be calculated by replacing the time-like killing vector $\xi^\mu_{(t)}$ with the rotational killing vector $-\xi^\mu_{(\varphi)} = (0,0,0,-1)$. For the energy and angular momentum fluxes composed of a single (ω, m), the angular momentum flux is obtained by multiplying m/ω to the energy flux. After some calculation, we obtain

$$F_{\mathcal{H}^+} = 2\omega_{1,I} E_1 + 2\omega_{2,I} E_2 - F_0 E_1^2 E_2 \ , \tag{3.30}$$

$$F_{\mathcal{I}^+} = -F_3 E_1 E_2^2 \ , \tag{3.31}$$

---

[3]Note that this relation holds only for a cloud satisfying the linearized equation of motion.
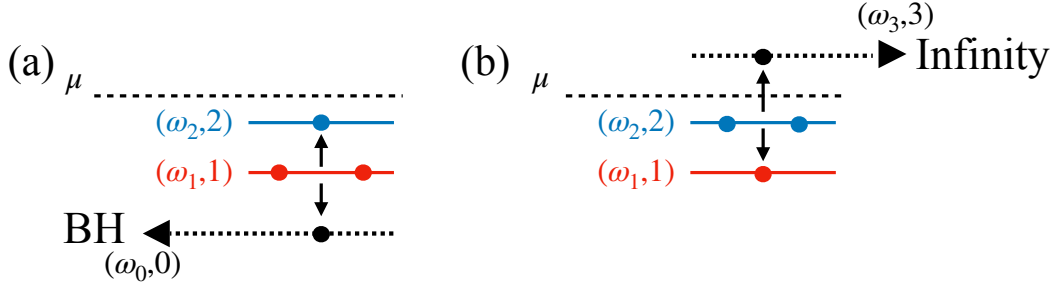
Figure 3.2: Figures (a) and (b) visualize the energy dissipation processes by the excitation of $(\omega', m') = (\omega_0, 0)$ and $(\omega_3, 3)$ modes, respectively. The solid horizontal lines correspond to the energy levels of the bound states involved in the process. In the case of (a), one of the two axions in the $l = m = 1$ cloud makes a transition to the $l = m = 2$ cloud. Owing to the energy and angular momentum conservation laws, the other simultaneously generated axion occupies the $(\omega, m) = (\omega_0, 0)$ mode with $\omega_0 = 2\omega_1 - \omega_2 < \mu$. Since the $m = 0$ mode is non-superradiant, this axion particle transfers the energy to the BH. In the case of (b), one of the two axions in the $l = m = 2$ cloud makes a transition to the $l = m = 1$ cloud. In this case, the axion after transition occupies the $(\omega, m) = (\omega_3, 3)$ mode with $\omega_3 = 2\omega_2 - \omega_1 > \mu$, which carries the energy to infinity.

with

$$F_0 = \sum_{l \geq 0} 72\pi M \lambda^2 r_+ \omega_{0,R}^2 \left| \frac{1}{W_{l0}(\omega_0)} \int_{r_+}^{\infty} dr \int_0^{\pi} d\theta \, (r^2 + a^2 \cos^2\theta) \right.$$

$$\left. \times R_{l0\omega_0}^{\mathrm{up}}(r) S_{l0\omega_0}(\theta) R_1(r)^2 R_2(r)^* S_1(\theta)^2 S_2(\theta) \right|^2, \tag{3.32}$$

$$F_3 = \sum_{l \geq 3} 36\pi \lambda^2 \omega_{3,R} \sqrt{\omega_{3,R}^2 - \mu^2} \left| \frac{1}{W_{l3}(\omega_3)} \int_{r_+}^{\infty} dr \int_0^{\pi} d\theta \, (r^2 + a^2 \cos^2\theta) \right.$$

$$\left. \times R_{l3\omega_3}^{\mathrm{in}}(r) S_{l3\omega_3}(\theta) R_2(r)^2 R_1(r)^* S_2(\theta)^2 S_1(\theta) \right|^2. \tag{3.33}$$

In Appendix C, we show the details of the calculation. Note that F_0 corresponds to the energy flux carried by the (ω_0, m_0) modes and F_3 is that by the (ω_3, m_3) modes. Note also that the dissipation comes from the second order in λ. In the following, we keep only the most dominant l mode in the summation. In the present case, they are the $l = 0$ mode in F_0 and the $l = 3$ mode in F_3.

The evolution equations for energies (3.26) and (3.27) reduce to

$$\frac{dE_1}{dt} + \frac{dE_2}{dt} = 2\omega_{1,I} E_1 + 2\omega_{2,I} E_2 - F_0 E_1^2 E_2 - F_3 E_1 E_2^2, \tag{3.34}$$

$$\frac{1}{\omega_{1,R}} \frac{dE_1}{dt} + \frac{2}{\omega_{2,R}} \frac{dE_2}{dt} = 2\omega_{1,I} \frac{1}{\omega_{1,R}} E_1 + 2\omega_{2,I} \frac{2}{\omega_{2,R}} E_2 - \frac{3}{\omega_{3,R}} F_3 E_1 E_2^2. \tag{3.35}$$

Simple algebra transforms Eqs. (3.34) and (3.35) to

$$\frac{dE_1}{dt} = 2\omega_{1,I} E_1 - \frac{2\omega_{1,R}}{\omega_{0,R}} F_0 E_1^2 E_2 + \frac{\omega_{1,R}}{\omega_{3,R}} F_3 E_1 E_2^2, \tag{3.36}$$

$$\frac{dE_2}{dt} = 2\omega_{2,I} E_2 + \frac{\omega_{2,R}}{\omega_{0,R}} F_0 E_1^2 E_2 - \frac{2\omega_{2,R}}{\omega_{3,R}} F_3 E_1 E_2^2. \tag{3.37}$$

These equations describe the physical picture of the dissipation processes caused by the $(\omega', m') = (\omega_0, 0)$ and $(\omega_3, 3)$ modes. The process involving $(\omega', m') = (\omega_0, 0)$ causes the dissipation of the energy of the $l = m = 1$ cloud and feeds some energy to the $l = m = 2$ cloud. The case with $(\omega', m') = (\omega_3, 3)$ is the opposite, reducing the energy of the $l = m = 2$ cloud and feeding the $l = m = 1$ cloud. We show these processes schematically in Fig. 3.2.

3.3   Acceleration of the instability

We treat the superradiant bound modes in this section. Since the dissipation appears from the second order in λ, we will calculate the effect of the fourth class up to the second order in λ. Also, we consider the effect sourced only by the $l = m = 1$ cloud. If the source involves the higher multipole $l = m = 2$ cloud, its effect on the evolution should be subdominant, since the large spatial extension of the $l = m = 2$ cloud reduces the strength of the interaction.

3.3.1   First order perturbation

We start with the first order perturbation. When we focus on the source composed solely of the $l_1 = m_1 = 1$ cloud, the first order particular solution is given by

$$
\phi^{(1)} = -\sum_{l \geq l_1} \Big[A^3 e^{-3i(\omega_1 t - m_1 \varphi)} S_{l3m_13\omega_1}(\theta) f^{(1)}_{l3m_13\omega_1}(r)
$$

$$
+ 3A|A|^2 e^{2\omega_{1,I} t} e^{-i(\omega_1 t - m_1 \varphi)} S_{lm_1\omega_1 + 2i\omega_{1,I}}(\theta) f^{(1)}_{lm_1\omega_1 + 2i\omega_{1,I}}(r) \Big] + \text{c.c.}
$$

$$
+ \text{(homogeneous solution)} , \tag{3.38}
$$

where $A(t_0)$ is the amplitude of the $l_1 = m_1 = 1$ cloud at the reference time t_0 defined by

$$
A \equiv \sqrt{E_1} e^{-i\Theta} , \tag{3.39}
$$

where we included the phase for later convenience. Here, $f^{(1)}_{l3m_13\omega_1}(r)$ and $f^{(1)}_{lm_1\omega_1 + 2i\omega_{1,I}}(r)$ are defined by

$$
f^{(1)}_{l3m_1\omega}(r) \equiv \int dr' d\cos\theta' \ (r'^2 + a^2 \cos^2\theta') S_{l3m_1\omega}(\theta') G^{\omega}_{l3m_1}(r, r')
$$

$$
\times S_1(\theta')^3 R_1(r')^3 , \tag{3.40}
$$

$$
f^{(1)}_{lm_1\omega}(r) \equiv \int dr' d\cos\theta'(r'^2 + a^2 \cos^2\theta') S_{lm_1\omega}(\theta') G^{\omega}_{lm_1}(r, r')
$$

$$
\times |S_1(\theta')|^2 S_1(\theta') |R_1(r')|^2 R_1(r') . \tag{3.41}
$$

The perturbative solution (3.38) grows exponentially, and thus the amplitude of the perturbation quickly becomes large, breaking the assumption of perturbative expansion (3.5). In the following, we apply the renormalization group (RG) method to avoid the breakdown of the perturbation theory. The RG method is the technique to eliminate the secular divergence that appears in a singular perturbation theory [57, 58, 59, 60].

The first step of the RG method, is to identify the term that diverges in $\omega_{1,I} \to 0$ limit and subtracts them by choosing the appropriate homogenous solution in Eq. (3.21). The

divergent part comes from the factor $W_{l_1m_1}^{-1}(\omega_1 + 2i\omega_{1,I})$ contained in $f_{l_1m_1\omega_1+2i\omega_{1,I}}^{(1)}(r)$. As mentioned earlier, the boundary conditions of the cloud lead to $W_{l_1m_1}(\omega_1) = 0$, which implies $f^{(1)}$ is divergent in the limit $\omega_{1,I} \to 0$. Therefore, the leading term of $f_{l_1m_1\omega_1+2i\omega_{1,I}}^{(1)}(r)$ in the limit $\omega_{1,I} \to 0$ is given by

$$f_{l_1m_1\omega_1+2i\omega_{1,I}}^{(1)}(r) \sim C_{l_1m_1\omega_1}^{(1)} R_{l_1m_1\omega_1}(r) , \tag{3.42}$$

$$C_{l_1m_1\omega_1}^{(1)} \equiv \frac{1}{2i\alpha_{\omega_1}\sqrt{\omega_1^2 - \mu^2}2i\omega_{1,I}A_{\text{out}}(\omega_1)} \int dr'd\cos\theta'$$
$$\times (r'^2 + a^2\cos^2\theta')|S_{l_1m_1\omega_1}(\theta')|^2 S_{l_1m_1\omega_1}(\theta')^2$$
$$\times R_{l_1m_1\omega_1}(r')|R_{l_1m_1\omega_1}(r')|^2 R_{l_1m_1\omega_1}(r') , \tag{3.43}$$

where we defined α_{ω_1} by the leading term in the Taylor expansion of $W_{lm}(\omega)$:

$$W_{lm}(\omega) \sim 2i\sqrt{\omega_1^2 - \mu^2}\alpha_{\omega_1}(\omega - \omega_1) + \cdots . \tag{3.44}$$

We utilize the relation, $R_{lm\omega}^{\text{in}} = A_{\text{out}}(\omega)R_{lm\omega}^{\text{up}}$ for $(l, m, \omega) = (l_1, m_1, \omega_1)$. We call Eq. (3.42) a divergent term, although it is not strictly divergent since $\omega_{1,I}$ is small but not vanishing.

Before choosing the appropriate homogeneous solution, we show

$$\text{Re}\left[C_{l_1m_1\omega_1}^{(1)}\right] = \mathcal{O}(\omega_{1,I}^0) , \tag{3.45}$$

$$\text{Im}\left[C_{l_1m_1\omega_1}^{(1)}\right] = \mathcal{O}(\omega_{1,I}^{-1}) , \tag{3.46}$$

which state that the divergence only comes from the imaginary part of $C^{(1)}$. To prove Eqs. (3.45) and (3.46), notice that most of the quantities, except for $\sqrt{\omega_1^2 - \mu^2}$, involved in $C_{l_1m_1\omega_1}^{(1)}$ are related to the mode functions $R_{l_1m_1\omega_1}$ and $S_{l_1m_1\omega_1}$. We can choose these mode functions to be real in the limit, $\omega_{1,I} \to 0$, since the radial and the angular equations (2.12) and (2.11) are both real in this limit. Therefore, the leading term in $C_{l_1m_1\omega_1}^{(1)}$ is real except for the factor $\sqrt{\omega_1^2 - \mu^2}$. Since the unstable modes are bounded, i.e., $\omega_{1,R} < \mu$, the factor $\sqrt{\omega_1^2 - \mu^2}$ is purely imaginary in the limit under consideration. Therefore, only $\text{Im}\left[C_{l_1m_1\omega_1}^{(1)}\right]$ is divergent in the limit $\omega_{1,I} \to 0$.

Since the divergent part is proportional to the original unstable mode, we only need to choose an appropriate amplitude to cancel the divergence. Note that there is still freedom of choosing the non-divergent part. The appropriate choice of the amplitude leads to the first order perturbative solution

$$\phi = \left(A + 3\lambda\tilde{C}_{l_1m_1\omega_1}^{(1)}A|A|^2e^{2\omega_{1,I}t_0}\right)e^{-i(\omega_1t-m_1\varphi)}S_{l_1m_1\omega_1}(\theta)R_{l_1m_1\omega_1}(r)$$

$$- \lambda\left(\sum_{l=3m_1}^{\infty}\left[A^3e^{-3i(\omega_1t-m_1\varphi)}S_{l3m_13\omega_1}(\theta)f_{l3m_13\omega_1}^{(1)}(r)\right]\right.$$

$$+ \sum_{l=m_1}^{\infty}\left[3A|A|^2e^{2\omega_{1,I}t}e^{-i(\omega_1t-m_1\varphi)}S_{lm_1\omega_1+2i\omega_{1,I}}(\theta)f_{lm_1\omega_1+2i\omega_{1,I}}^{(1)}(r)\right]\right)$$

$$+ \text{c.c.} , \tag{3.47}$$

where $\tilde{C}^{(1)} = C^{(1)} + \delta C^{(1)}$ and $\delta C^{(1)}$ denotes the finite part $(\mathcal{O}(\omega_{1,I}^0))$ which represents the arbitrariness in the choice of the non-divergent part. Actually, this ambiguity is related to

27

the choice of the definition of the amplitude [52]. In the expression (3.47), we introduced a reference time t_0, which is arbitrary. The divergent term is canceled only at $t = t_0$.

To remove the divergence globally, we impose the RG equation

$$\frac{\partial \phi}{\partial t_0} = 0 \;, \tag{3.48}$$

on the solution (3.47). Taking care of dependence of the amplitude on t_0, we obtain the evolution equation for the amplitude as

$$\frac{dA(t_0)}{dt_0} = -6\lambda\omega_{1,I}\tilde{C}^{(1)}_{l_1m_1\omega_1}A(t_0)|A(t_0)|^2 e^{2\omega_{1,I}t_0} + \mathcal{O}(\lambda^2) \;. \tag{3.49}$$

We redefine the amplitude A to include the exponentially growing factor owing to the superradiant instability, which is accomplished by rewriting A in terms of $\mathcal{A} \equiv Ae^{\omega_{1,I}t}$. Then, the evolution equation for the redefined amplitude is

$$\frac{d\mathcal{A}}{dt} = \omega_{1,I}\mathcal{A} - 6\lambda\omega_{1,I}\tilde{C}^{(1)}_{l_1m_1\omega_1}\mathcal{A}|\mathcal{A}|^2 \;. \tag{3.50}$$

Substituting the solution of Eq. (3.50) to Eq. (3.47), and setting $t_0 = t$, we obtain the renormalized first order perturbative solution

$$\begin{aligned}
\phi =& \mathcal{A}(t)e^{-i(\omega_{1,R}t - m_1\varphi)}S_{l_1m_1\omega_1}(\theta)R_{l_1m_1\omega_1}(r) \\
&- \lambda \Bigg(\sum_{l=3m_1}^{\infty} \mathcal{A}^3(t)e^{-3i(\omega_{1,R}t-m_1\varphi)}S_{l3m_13\omega_1}(\theta)f^{(1)}_{l3m_13\omega_1}(r) \\
&+ \sum_{l>m_1}^{\infty} \left[3\mathcal{A}(t)|\mathcal{A}(t)|^2 e^{-i(\omega_{1,R}t-m_1\varphi)}S_{lm_1\omega_1+2i\omega_{1,I}}(\theta)f^{(1)}_{lm_1\omega_1+2i\omega_{1,I}}(r) \right] \\
&+ 3\mathcal{A}(t)|\mathcal{A}(t)|^2 e^{-i(\omega_{1,R}t-m_1\varphi)}\delta\phi_{(1)} \Bigg) + \text{c.c.} \;, \tag{3.51}
\end{aligned}$$

where

$$\delta\phi^{(1)} \equiv S_{l_1m_1\omega_1+2i\omega_{1,I}}(\theta)f^{(1)}_{l_1m_1\omega_1+2i\omega_{1,I}}(r) - \tilde{C}^{(1)}_{l_1m_1\omega_1}S_{l_1m_1\omega_1}(\theta)R_{l_1m_1\omega_1}(r) \;, \tag{3.52}$$

is the non-divergent part of $f^{(1)}_{l_1m_1\omega_1+2i\omega_{1,I}}(r)$. Now, the solution does not have a divergent term which breaks the validity of the perturbation theory.

3.3.2 Second order perturbation

We move to the second order perturbation. The second order equation is given by

$$(\Box_g - \mu^2)\phi^{(2)} = -3\left(\phi^{(0)}\right)^2\phi^{(1)} \;. \tag{3.53}$$

Same as the first order perturbation, we solve Eq. (3.53) by the Green's function method, which gives

$$\begin{aligned}
\phi^{(2)} =& -3\int \sqrt{-g(x')}d^4x' G_{\text{ret}}(x,x')\left(\phi^{(0)}\right)^2\phi^{(1)} \\
&+ \text{(homogeneous solution)} \;. \tag{3.54}
\end{aligned}$$

Here, $\phi^{(1)}$ is given by the $\mathcal{O}(\lambda)$ part in Eq. (3.47). As we see in the first order perturbation, the divergent term in the limit $\omega_{1,I} \to 0$ originates from the Wronskian $W_{l_1 m_1}(\omega_1)$. Therefore, the term contained in $\phi^{(2)}$ that has the potentially divergent Wronskian is

$$\phi^{(2)} \supset 3A|A|^4 \sum_{l,l'} \int d\cos\theta' \int dr' (r'^2 + a^2 \cos^2\theta') e^{4\omega_{1,I}t} e^{-i(\omega_1 t - m_1\varphi)}$$

$$\times S_{lm_1\omega_1 + 4i\omega_{1,I}}(\theta) S_{lm_1\omega_1 + 4i\omega_{1,I}}(\theta') G_{lm_1}^{\omega_1 + 4i\omega_{1,I}}(r, r')$$

$$\times \left(S_{l_1 m_1\omega_1}^*(\theta')^2 R_{l_1 m_1\omega_1}^*(r')^2 S_{l'3m_13\omega_1}(\theta') f_{l'3m_13\omega_1}^{(1)}(r') \right.$$

$$+ 6|S_{l_1 m_1\omega_1}(\theta')|^2 |R_{l_1 m_1\omega_1}(r')|^2 S_{l'm_1\omega_1 + 2i\omega_{1,I}}(\theta') f_{l'm_1\omega_1 + 2i\omega_{1,I}}^{(1)}(r')$$

$$+ 3S_{l_1 m_1\omega_1}(\theta')^2 R_{l_1 m_1\omega_1}(r')^2$$

$$\left. \times S_{l'm_1\omega_1 + 2i\omega_{1,I}}^*(\theta') f_{l'm_1\omega_1 + 2i\omega_{1,I}}^{(1)*}(r') \right) . \tag{3.55}$$

The divergent part in the expression (3.55) is identified to be

$$3C_{l_1 m_1\omega_1}^{(2)} A|A|^4 e^{4\omega_{1,I}t} e^{-i(\omega_1 t - m_1\varphi)} S_{l_1 m_1\omega_1} R_{l_1 m_1\omega_1} , \tag{3.56}$$

where $C^{(2)}$ is defined by

$$C_{l_1 m_1\omega_1}^{(2)} \equiv \frac{1}{2i\alpha_{\omega_1}\sqrt{\omega_1^2 - \mu^2} 4i\omega_{1,I} A_{out}} \sum_{l'} \int d\cos\theta' \int dr'$$

$$\times (r'^2 + a^2 \cos^2\theta') S_{l_1 m_1\omega_1}(\theta') R_{l_1 m_1\omega_1}(r')$$

$$\times \left(S_{l_1 m_1\omega_1}^*(\theta')^2 R_{l_1 m_1\omega_1}^*(r')^2 S_{l'3m_13\omega_1}(\theta') f_{l'3m_13\omega_1}^{(1)}(r') \right.$$

$$+ 6|S_{l_1 m_1\omega_1}(\theta')|^2 |R_{l_1 m_1\omega_1}(r')|^2 S_{l'm_1\omega_1 + 2i\omega_{1,I}}(\theta') f_{l'm_1\omega_1 + 2i\omega_{1,I}}^{(1)}(r')$$

$$+ 3S_{l_1 m_1\omega_1}(\theta')^2 R_{l_1 m_1\omega_1}(r')^2$$

$$\left. S_{l'm_1\omega_1 + 2i\omega_{1,I}}^*(\theta') f_{l'm_1\omega_1 + 2i\omega_{1,I}}^{(1)*}(r') \right) . \tag{3.57}$$

There are two contributions to $C^{(2)}$. One is due to $\omega = 3\omega_1$ modes (the high frequency radiation of the classification in Sec. 3.1), which dissipates energy to infinity. The other is due to $\omega = \omega_1 + 2i\omega_{1,I}$ modes (the superradiant bound modes of the classification in Sec. 3.1), which decays at infinity and does not contribute to the energy dissipation. However, one can numerically confirm that the dissipative effect in $C_{l_1 m_1\omega_1}^{(2)}$ is subdominant [52].

Other than Eq. (3.56), we also have the divergence in the second order solution sourced by the divergent homogeneous solution we added to eliminate the divergent part in the first order solution. The formal solution from this type of source is given by

$$-9|A|^2 e^{2\omega_{1,I}t_0} \int \sqrt{-g(x')} d^4x' G_{\rm ret}(x, x') (\phi^{(0)}(x'))^2$$

$$\times \left(AC_{l_1 m_1\omega_1}^{(1)} e^{-i(\omega_1 t' - m_1\varphi')} S_{l_1 m_1\omega_1}(\theta') R_{l_1 m_1\omega_1}(r') + {\rm c.c.} \right) . \tag{3.58}$$

The divergent part of this expression is identified as

$$-9A|A|^4 e^{2\omega_{1,I}t_0} e^{2\omega_{1,I}t} \left(2C_{l_1 m_1\omega_1}^{(1)} C_{l_1 m_1\omega_1}^{(1)} + C_{l_1 m_1\omega_1}^{(1)*} C_{l_1 m_1\omega_1}^{(1)} \right)$$

$$\times e^{-i(\omega_1 t - m_1\varphi)} S_{l_1 m_1\omega_1}(\theta) R_{l_1 m_1\omega_1}(r) + {\rm c.c.} . \tag{3.59}$$

The appropriate homogeneous solution to eliminate the divergences (3.56) and (3.59) is

$$-3\lambda^2 \left[\left(C^{(2)}_{l_1 m_1 \omega_1} + \delta C^{(2)}_{l_1 m_1 \omega_1} \right) -3 \left(2 C^{(1)}_{l_1 m_1 \omega_1} \tilde{C}^{(1)}_{l_1 m_1 \omega_1} + \tilde{C}^{(1)*}_{l_1 m_1 \omega_1} C^{(1)}_{l_1 m_1 \omega_1} \right) \right]$$
$$\times A|A|^4 e^{4\omega_{1,I} t_1} e^{-i(\omega_1 t - m_1 \varphi)} S_{l_1 m_1 \omega_1} R_{l_1 m_1 \omega_1} . \tag{3.60}$$

Again, we introduced $\delta C^{(2)}$ to represent the non-divergent part.

Since we have identified the divergent terms, the evolution equation of the amplitude can be obtained by imposing the RG equation, as in the first order case. A similar calculation to the first order case leads to

$$\frac{dA}{dt} + 3\lambda \delta C^{(1)}_{l_1 m_1 \omega_1} \left(2|A|^2 \frac{dA}{dt} + A^2 \frac{dA^*}{dt} \right) e^{2\omega_{1,I} t}$$
$$= -6\lambda \omega_{1,I} \tilde{C}^{(1)}_{l_1 m_1 \omega_1} A|A|^2 e^{2\omega_{1,I} t} + 12\lambda^2 \omega_{1,I} \tilde{C}^{(2)}_{l_1 m_1 \omega_1} A|A|^4 e^{4\omega_{1,I} t} , \tag{3.61}$$

where $\tilde{C}^{(2)}_{l_1 m_1 \omega_1}$ and $\hat{C}^{(2)}_{l_1 m_1 \omega_1}$ are defined by

$$\tilde{C}^{(2)}_{l_1 m_1 \omega_1} \equiv \hat{C}^{(2)}_{l_1 m_1 \omega_1} + \delta C^{(2)}_{l_1 m_1 \omega_1} - \frac{3}{2} C^{(1)}_{l_1 m_1 \omega_1} \left(2\delta C^{(1)}_{l_1 m_1 \omega_1} + \delta C^{(1)*}_{l_1 m_1 \omega_1} \right) , \tag{3.62}$$

$$\hat{C}^{(2)}_{l_1 m_1 \omega_1} \equiv C^{(2)}_{l_1 m_1 \omega_1} - \frac{3}{2} C^{(1)}_{l_1 m_1 \omega_1} \left(2 C^{(1)}_{l_1 m_1 \omega_1} + C^{(1)*}_{l_1 m_1 \omega_1} \right) . \tag{3.63}$$

We note that $\hat{C}^{(2)}$ is $\mathcal{O}(\omega_{1,I}^{-1})$ quantity owing to the cancellation of the $\mathcal{O}(\omega_{1,I}^{-2})$ terms in $C^{(2)}$ and $C^{(1)}(2C^{(1)} + C^{(1)*})$.

Let us rewrite the amplitude equation (3.61) in terms of the energy E_1. Recalling the relation (3.39) and incorporating the superradiant instability as in Eq. (3.50), we obtain

$$\frac{1}{2\omega_{1,I}} \frac{dE_1}{dt} = E_1 - 6\lambda \mathrm{Re}\left[C^{(1)} + \delta C^{(1)} \right] E_1^2 + 12\lambda^2 \mathrm{Re}\left[\hat{C}^{(2)} + \delta C^{(2)} \right] E_1^3$$
$$+ 18\lambda^2 \mathrm{Re}\left[\delta C^{(1)} \left(2\delta C^{(1)} + \delta C^{(1)*} \right) \right] E_1^3 , \tag{3.64}$$

$$\frac{\delta\omega}{\omega_{1,I}} = 6\lambda \mathrm{Im}\left[C^{(1)} + \delta C^{(1)} \right] E_1 - 12\lambda^2 \mathrm{Im}\left[\hat{C}^{(2)} + \delta C^{(2)} \right] E_1^2$$
$$+ 18\lambda^2 \mathrm{Im}\left[2C^{(1)} \delta C^{(1)*} - \delta C^{(1)} \left(2\delta C^{(1)} + \delta C^{(1)*} \right) \right] E_1^2 . \tag{3.65}$$

Here, we defined the frequency shift by

$$\delta\omega \equiv \frac{d\Theta}{dt} . \tag{3.66}$$

Equations (3.64) and (3.65) show that the evolution of the energy and the frequency shift is subject to the renormalization group scheme, the choice of the finite part $\delta C^{(1)}$ and $\delta C^{(2)}$. In particular, we should be careful that the meaning of E_1 depends on the prescription we choose. On the other hand, we can show the scheme independence of $\delta\omega$ [52]. However, to obtain the scheme independent evolution equation in terms of $\delta\omega$ up to $\mathcal{O}(\lambda^2)$, we need to proceed our calculation to the next order in λ, which requires tedious calculation. In the following, we fix $\delta C^{(1)}$ and $\delta C^{(2)}$ by requiring the minimal subtraction instead of pushing the perturbation theory to the next order.

We choose the simplest scheme[4]

$$\delta C^{(1)} = \delta C^{(2)} = 0 . \tag{3.67}$$

---

[4]See Ref. [52] for other choice of the scheme.

Table 3.2: The frequency of the mode, $\mathrm{Re}\left[C_{l_1 m_1 \omega_1}^{(1)}\right]$, and $\mathrm{Re}\left[\hat{C}_{l_1 m_1 \omega_1}^{(2)}\right]$ for the $\mu M = 0.42$ and 0.3 with $a/M = 0.99$ is shown.

$(\mu M, l_1, m_1, n_1)$	$M\omega_R$	$M\omega_I$	$\mathrm{Re}\left[C_{l_1 m_1 \omega_1}^{(1)}\right]$	$\mathrm{Re}\left[\hat{C}_{l_1 m_1 \omega_1}^{(2)}\right]$
(0.42,1,1,0)	0.4088	1.504×10^{-7}	-3.29×10^{-3}	2.72×10^{-5}
(0.3,1,1,0)	0.2963	2.681×10^{-8}	-2.54×10^{-3}	1.99×10^{-5}

Under the scheme (3.67), the evolution equations are given by

$$\frac{dE_1}{dt} = 2\omega_{1,I}\left(1 - 6\lambda \mathrm{Re}\left[C_{l_1 m_1 \omega_1}^{(1)}\right]E_1 + 12\lambda^2 \mathrm{Re}\left[\hat{C}_{l_1 m_1 \omega_1}^{(2)}\right]E_1^2\right)E_1 \ , \tag{3.68}$$

$$\frac{\delta\omega}{\omega_{1,I}} = 6\lambda \mathrm{Im}\left[C^{(1)}\right]E_1 - 12\lambda^2 \mathrm{Im}\left[\hat{C}_{l_1 m_1 \omega_1}^{(2)}\right]E_1^2 \ . \tag{3.69}$$

We observe that the self-interaction effect effectively changes the growth rate $\omega_{1,I}$. By numerically calculating the coefficients, we can show $\mathrm{Re}\left[C^{(1)}\right] < 0$ and $\mathrm{Re}\left[\hat{C}^{(2)}\right] > 0$ which indicates the acceleration of the growth. One concern is whether E_1 in the prescription we choose corresponds to the actual energy of the cloud. In Sec. 4.1, we will show the perturbative evolution of E_1 follows almost the same track as the nonlinear evolution when the amplitude is small (see Fig. 4.4). This suggests that E_1 in the current scheme is in good agreement with the actual energy of the condensate.

3.4 Perturbative evolution of the self-interacting condensate

Now, we combine the evolution equations (3.36) and (3.68) by simply replacing the growth rate $\omega_{1,I}$ in (3.36) by

$$\omega_{1,I}\left(1 - 6\lambda \mathrm{Re}\left[C_{l_1 m_1 \omega_1}^{(1)}\right]E_1 + 12\lambda^2 \mathrm{Re}\left[\hat{C}_{l_1 m_1 \omega_1}^{(2)}\right]E_1^2\right) \ . \tag{3.70}$$

Thus, the perturbative equations governing the evolution of the condensate composed of two clouds are

$$\frac{dE_1}{dt} = 2\omega_{1,I}\left(1 - 6\lambda \mathrm{Re}\left[C^{(1)}\right]E_1 + 12\lambda^2 \mathrm{Re}\left[\hat{C}^{(2)}\right]E_1^2\right)E_1$$
$$- \frac{2\omega_{1,R}}{\omega_{0,R}}F_0 E_1^2 E_2 + \frac{\omega_{1,R}}{\omega_{3,R}}F_3 E_1 E_2^2 \ , \tag{3.71}$$

$$\frac{dE_2}{dt} = 2\omega_{2,I}E_2 + \frac{\omega_{2,R}}{\omega_{0,R}}F_0 E_1^2 E_2 - \frac{2\omega_{2,R}}{\omega_{3,R}}F_3 E_1 E_2^2 \ . \tag{3.72}$$

In Fig. 3.3, we show examples of the time evolution for $\mu M = 0.42$ and $\mu M = 0.3$ with the black hole spin $a/M = 0.99$. We also show the actual values of $C^{(1)}$ and $\hat{C}^{(2)}$ for these cases in Table 3.2.[5] Since the cloud should start with extremely small energy, we

---

[5] The values of $\mathrm{Re}\left[C_{l_1 m_1 \omega_1}^{(1)}\right]$, and $\mathrm{Re}\left[\hat{C}_{l_1 m_1 \omega_1}^{(2)}\right]$ are different from our paper [52], since the normalization of the radial mode function is different. In Ref. [52], the normalization is given by

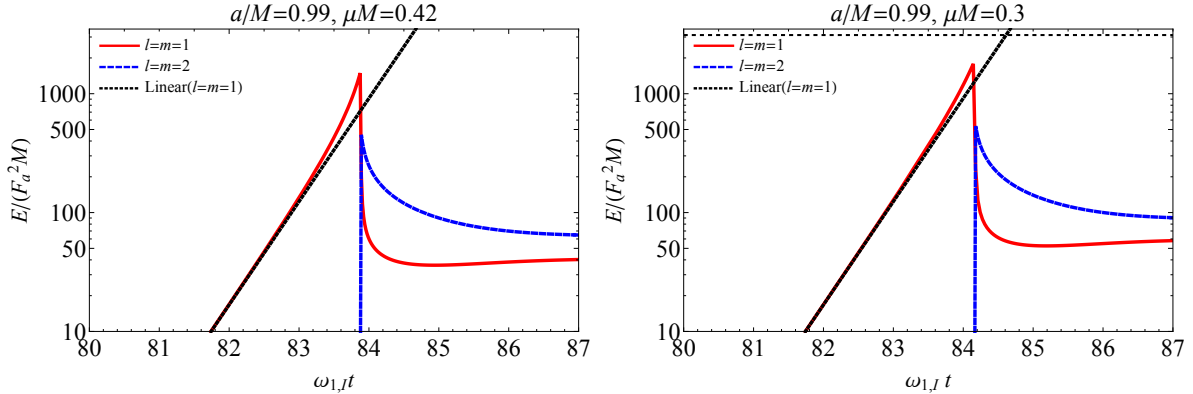$$\int dr \ r^2 |R_{lm\omega}|^2 = M^3 \ . \tag{3.73}$$

31

Figure 3.3: Time evolution of the energy of each mode when the axion cloud is composed of two modes $l = m = 1$ and $l = m = 2$ in the perturbtive approach. The left (right) panel shows the time evolution of the energy of the $l = m = 1$ cloud, E_1(red solid), and that of the $l = m = 2$ cloud, E_2 (blue dotted), with the axion mass $\mu M = 0.42(0.3)$. In both panels, black dotted lines are the time evolution of the $l = m = 1$ cloud energy in the linear approximation. We set the spin of the BH to $a/M = 0.99$. We take the initial energies of the two clouds to be $E_1 = E_2 = 10^{-70} F_a^2 M$. We normalized the time in the horizontal axis by the superradiant growth rate of the $l = m = 1$ cloud, $\omega_{1,I}^{-1}$. The horizontal dashed line in the right panel describes the energy where the dynamical instability sets in (see chapter 4 for detail).

take the initial condition as

$$E_1(t_{\text{ini}}) = E_2(t_{\text{ini}}) = \mu \sim \frac{10^{-70}}{\mu M} \left(\frac{\mu}{10^{-13}\text{eV}} \right)^2 F_a^2 M \ , \tag{3.74}$$

which corresponds to the case in which each axion cloud starts with a single axion particle. Here in Eq. (3.74), The choice of parameter, $\mu M = 0.42$, gives an instability rate close to the maximum value [30]. On the other hand, the axion mass $\mu M = 0.3$, as we will show in the Sec. 4.1, is in the range where bosenova occurs if we consider the evolution of the condensate composed of a single cloud. In both cases, the qualitative behavior of the obtained time evolution is the same. In early times, both $l = m = 1$ and $l = m = 2$ clouds grow owing to the superradiant instability, independently of the effect of self-interaction. Since the instability timescale of the $l = m = 2$ cloud is much longer than that of the $l = m = 1$ cloud, only the $l = m = 1$ cloud grows in practice.

As the cloud grows, the instability is accelerated by the self-interaction. After the energy of the $l = m = 1$ cloud gets close to the maximum value, overshooting the value at which the first and second terms in the right-hand side of Eq. (3.71) balance, in the end the rapid dissipation of $l = m = 1$ cloud and simultaneously the excitation of the $l = m = 2$ cloud happen. Overshooting occurs because the energy dissipation through the non-superradiant dissipative mode (the left panel of Fig. 3.2) is proportional to the energy of the $l = m = 2$ cloud and hence suppressed before the $l = m = 2$ cloud becomes large. After this rapid energy dissipation, eventually, the whole condensate settles into a superposition of the two clouds, sharing comparable energies between them. Interestingly, the excitation of the $l = m = 2$ cloud occurs more rapidly than the initial growth rate of the $l = m = 1$ cloud, which is much faster than the initial rate of the superradiant instability of the $l = m = 2$ cloud.

The overall picture so far is based on the perturbation theory. However, because of the

presence of the overshooting, the cloud inevitably enters the nonlinear regime, where the deformation of the cloud configuration from the linear one cannot be appropriately taken into account perturbatively. In the fully nonlinear description, the numerical coefficients in Eqs. (3.72) and (3.71) are altered, leading to a modification of the time evolution. In the next section, we perform non-perturbative calculations to examine whether a more accurate treatment of the nonlinear effects can qualitatively change the evolution.

Chapter 4

Nonperturbative method to track the evolution of the condensate

In the previous chapter, we found that even if we consider the dissipation by the self-interaction, the condensate inevitably enters the regime where the perturbative method cannot be trusted. To predict the final fate of the condensate, we need to study the evolution taking into account the nonlinear effects that are dismissed by the perturbative method, such as the deformation of the condensate. However, because of the adiabatic nature of the evolution (the instability time scale ≫ the dynamical time scale), we cannot follow the evolution of the condensate by the dynamical simulation. In this chapter, we propose a new method to track the evolution in a strongly nonlinear regime with the aid of the adiabaticity of the evolution. This chapter is based on our works Ref. [54] and [53].

4.1   Single mode calculation

For simplicity, we start with the condensate composed solely of the fastest growing mode $(n_1, l_1.m_1) = (2, 1, 1)$. In the next section, we consider the effect of the second mode $(n_2, l_2, m_2) = (3, 2, 2)$. Our strategy is to use the fact that the cloud grows adiabatically, which means that the dynamical time scale of the cloud is much larger than its growth rate, $i.e.$,

$$\omega_I \ll \omega_R \ . \tag{4.1}$$

In other words, the amplitude and the configuration of the axion field vary only gradually with the long time scale ($\sim \omega_I^{-1}$). Thus, in a short time scale ($\ll \omega_I^{-1}$), we can regard the axion field configuration to be almost stationary with an approximately fixed amplitude A_1. During the adiabatic evolution, it is likely that the symmetry of configuration is preserved. Since the configuration of the cloud in the linear approximation has helical symmetry, we assume an approximately helical symmetric configuration

$$\phi(A_1) = \sum_{k=1}^{\infty} \sum_{l \geq km_1}^{\infty} e^{-ik(\omega_1(A_1)t - m_1\varphi)} \tilde{R}_{kl}(r; A_1) Y_{lkm_1}(\cos\theta) + \text{c.c.} \ , \tag{4.2}$$

as the configuration of the axion field with an arbitrary amplitude A_1. Here, $Y_{lm}(x)$ is defined as

$$Y_{lm}(x) \equiv N_l^m P_l^m(x) \ , \tag{4.3}$$

with $P_l^m(x)$ is the associated Legendre polynomial and

$$N_l^m = \sqrt{\frac{(l-m)!(2l+1)}{2(l+m)!}} \, , \tag{4.4}$$

is the normalization constant such that $Y_{lm}(x)$ satisfies

$$\int_{-1}^{1} dx \, Y_{lm}(x) Y_{l'm}(x) = \delta_{ll'} \, . \tag{4.5}$$

The amplitude A_1 is a parameter that corresponds to the amplitude of the fundamental mode at a large radius, *i.e.*,

$$\tilde{R}_{1l_1}(r; A_1) \to A_1 \frac{e^{-\sqrt{\mu^2 - \omega_1^2} r}}{r/M} \left(\frac{r}{M}\right)^{-M\frac{\mu^2 - 2\omega_1^2}{\sqrt{\mu^2 - \omega_1^2}}} (1 + \mathcal{O}(r^{-1})) \, , \qquad (r \to \infty) \, . \tag{4.6}$$

Since the self-interaction causes the frequency shift, we take the fundamental frequency of the configuration, $\omega_1 = \omega_1(A_1)$, to depend on the amplitude A_1.

We plug in the ansatz (4.2) to the equation of motion (3.3) and obtain

$$\frac{d}{dr}\left(\Delta \frac{d\tilde{R}_{kl}}{dr}\right) + \left[\frac{k^2(\omega_1(r^2 + a^2) - am_1)^2}{\Delta} - \mu^2 r^2 + 2ak^2\omega_1 m_1 - a^2 k^2 \omega_1^2 - l(l+1)\right.$$

$$\left. + a^2(k^2\omega_1^2 - \mu^2)\frac{1 - 2l(l+1) + 2k^2 m_1^2}{3 - 4l(l+1)}\right] \tilde{R}_{kl}$$

$$+ a^2(k^2\omega_1^2 - \mu^2)\left(\frac{(l-1-km_1)(l-km_1)}{(2l-3)(2l-1)}\frac{N_{l-2}^{km_1}}{N_l^{km_1}}\tilde{R}_{kl-2}\right.$$

$$\left. + \frac{(l+2+km_1)(l+1+km_1)}{(2l+3)(2l+5)}\frac{N_{l+2}^{km_1}}{N_l^{km_1}}\tilde{R}_{kl+2}\right)$$

$$+ \int_0^{2\pi} \frac{d\varphi}{2\pi} \int_{-1}^{1} dx \, Y_{lkm_1}(x) e^{-inm_1\varphi}(r^2 + a^2 x^2)V'(\phi) = 0 \, . \tag{4.7}$$

Here, the time derivative of the amplitude A_1 is neglected, since the change of the amplitude is very slow during the adiabatic evolution. The appropriate boundary condition to impose on $\tilde{R}_{kl}$ is the ingoing boundary condition at the event horizon and the outgoing (exponentially decaying) boundary condition for $\omega > \mu$ ($\omega < \mu$) at infinity. In the asymptotic region ($r \to +\infty$ and $r \to r_+$), the nonlinear terms drop sufficiently fast owing to the localized nature of the condensate. Neglecting the nonlinear term in Eq. (4.7), we obtain the asymptotic solutions satisfying these boundary conditions as

$$\tilde{R}_{kl} \longrightarrow A_{kl}^{(\text{in})} \left(\frac{r - r_+}{M}\right)^{-ik\frac{2Mr_+}{r_+ - r_-}(\omega_1 - m\Omega_H)} \, , \qquad (r \to r_+) \, , \tag{4.8}$$

$$\tilde{R}_{kl} \longrightarrow A_{kl}^{(\text{out})} \frac{e^{+i\sqrt{k^2\omega_1^2 - \mu^2} r}}{r/M} \left(\frac{r}{M}\right)^{-iM\frac{\mu^2 - 2k^2\omega_1^2}{\sqrt{k^2\omega_1^2 - \mu^2}}}$$

$$\times \left(1 + \frac{a_1}{r/M} + \frac{a_2}{(r/M)^2} + \cdots\right) \, , \qquad (r \to \infty) \, . \tag{4.9}$$

We determine the coefficients $a_1, a_2, \cdots$ analytically order by order. In our calculation, we take the coefficients up to a_7. Here, $A_{kl}^{(\text{in})}$ and $A_{kl}^{(\text{out})}$ are the parameters describing the asymptotic amplitude of mode specified by k and l, which will be determined by solving the non-linear equation.

The ansatz (4.2) cannot describe the solution which tracks the evolution over the growth time scale $\omega_{1,I}^{-1}$. We obtain a globally valid solution in time by promoting the amplitude A_1 to be time-dependent. To obtain a solution global in time, we demand the amplitude A_1 to vary in time slowly. In particular, we require that the family of solutions parametrized with A_1, $\{\phi(A_1)\}_{A_1}$, is swept to satisfy the energy balance. Specifically, we determine the time evolution of A_1 by

$$\frac{dE(A_1)}{dA_1}\frac{dA_1}{dt} = -F_{\text{tot}}(A_1) \ , \tag{4.10}$$

where we introduce the energy $E(A_1)$ and the net energy flux $F_{\text{tot}}(A_1)$ of the quasi-stationary configuration (4.2). For a given amplitude A_1, $E(A_1)$ and $F_{\text{tot}}(A_1)$ is calculated by

$$E(A_1) = \int dr \, d\cos\theta \, d\varphi \, (r^2 + a^2\cos^2\theta)\sqrt{g^{tt}}T_{\mu\nu}(A_1)\xi_{(t)}^{\mu}n_{(t)}^{\nu} \ , \tag{4.11}$$

$$F_{\text{tot}}(A_1) = F_H(A_1) + F_\infty(A_1) \ , \tag{4.12}$$

$$F_H(A_1) = \int d\cos\theta d\varphi \, 2Mr_+ T_{\mu\nu}(A_1)\xi_{(t)}^{\mu}l^{\nu}|_{r=r_+} \ , \tag{4.13}$$

$$F_\infty(A_1) = \int d\cos\theta d\varphi \, (r^2 + a^2\cos^2\theta)\sqrt{g^{rr}}T_{\mu\nu}(A_1)\xi_{(t)}^{\mu}n_{(r)}^{\nu}|_{r\to\infty} \ . \tag{4.14}$$

Here, the energy-momentum tensor $T_{\mu\nu}(A_1)$ in the one for the axion configuration (4.2). The explicit expressions are given by

$$(r^2 + a^2\cos^2\theta)\sqrt{g^{tt}}T_{\mu\nu}\xi_{(t)}^{\nu}n_{(t)}^{\nu} = \frac{(r^2+a^2)^2 - \Delta a^2\sin^2\theta}{2\Delta}(\partial_t\phi)^2 + \frac{\Delta}{2}(\partial_r\phi)^2$$
$$+ \frac{1}{2}(\partial_\theta\phi)^2 + \frac{\Delta - a^2\sin^2\theta}{2\Delta\sin^2\theta}(\partial_\varphi\phi)^2 + V(\phi) \ , \quad (4.15)$$

$$T_{\mu\nu}\xi_{(t)}^{\mu}l^{\nu}|_{r=r_+} = (\partial_t\phi + \Omega_H\partial_\varphi\phi)\partial_t\phi \ , \tag{4.16}$$

$$(r^2 + a^2\cos^2\theta)\sqrt{g^{tt}}T_{\mu\nu}\xi_{(t)}^{\mu}n_{(r)}^{\nu}|_{r\to\infty} = (r - r_+)(r - r_-)\partial_r\phi\partial_t\phi \ , \tag{4.17}$$

where we omit the argument of ϕ for notational simplicity. The angular momentum $J(A_1)$ can be evaluated by simply replacing $\xi_{(t)}^{\mu}$ in Eq. (4.11) by $-\xi_{(\varphi)}^{\mu} = (0,0,0,-1)$. The explicit formula is

$$J(A_1) = \int dr \, d\cos\theta \, d\varphi \, (r^2 + a^2\cos^2\theta)\sqrt{g^{tt}}T_{\mu\nu}(A_1)\left(-\xi_{(\varphi)}^{\mu}\right)n_{(t)}^{\nu} \ , \tag{4.18}$$

$$(r^2 + a^2\cos^2\theta)\sqrt{g^{tt}}T_{\mu\nu}(A_1)\xi_{(\varphi)}^{\mu}n_{(t)}^{\nu} = \left(\frac{(r^2+a^2)^2 - \Delta a^2\sin^2\theta}{\Delta}\partial_t\phi + \frac{2ar}{\Delta}\partial_\varphi\phi\right)\partial_\varphi\phi \ . \tag{4.19}$$

When the nonlinearity is small, $E(A_1)$ and $J(A_1)$ is related as

$$J(A_1) \sim \frac{m_1}{\omega_{1,R}(A_1)}E(A_1) \ . \tag{4.20}$$

4.1.1 Summary of the numerical calculation

In this subsection, we explain our numerical method to solve the Eq. (4.7) under the boundary conditions (4.8) and (4.9). In our calculation, the infinite summation in Eq. (4.2) is truncated at $l_{\max} = 5, k_{\max} = 5$ (see App. D for the justification of the truncation). Since we start with the $l_1 = m_1 = 1$ mode and the potentials we use (Eqs. (4.21)-(4.23)) are even function of ϕ, only modes with odd l, m appear in our calculation. Specifically, we only need to care with the modes $(l, m) = (1, 1), (3, 1), (5, 1), (3, 3), (5, 3),$ and $(5, 5)$. The modes with $(l, m) = (1, 1), (3, 1),$ and $(5, 1)$ are bounded and represent the $l = m = 1$ cloud[1]. On the other hand, modes with $(l, m) = (3, 3), (5, 3),$ and $(5, 5)$ is unbounded modes which radiate energy to infinity. In particular, they correspond to the high frequency radiation discussed in Sec. 3.1.

To find the nonlinear configuration for a given amplitude A_1 (the amplitude of the fundamental mode at large r), we need to determine the 12 remaining complex parameters consistently. The 12 parameters are the frequency ω_1 and the amplitudes of modes at the horizon $A_{kl}^{(\mathrm{in})}$ ($(k, l) = (1, 1), (1, 3), (1, 5), (3, 3), (3, 5),$ and $(5, 5)$) and at a large radius $A_{kl}^{(\mathrm{out})}$ ($(k, l) = (1, 3), (1, 5), (3, 3), (3, 5),$ and $(5, 5)$). These parameters are obtained by the shooting method. We guess 12 complex parameters and integrate Eq. (4.7) from both ends of the domain $r_* \in [r_{\min}, r_{\max}]$ to $r_* = r_{\mathrm{match}}$. We impose the boundary conditions Eq. (4.8) at $r_* = r_{\min}$ and Eq. (4.9) at $r_* = r_{\max}$. Then, we adjust the parameters until the solution joins smoothly at the $r_* = r_{\mathrm{match}}$. We take $r_{\min} = -100M, r_{\max} = 100M,$ and $r_{\mathrm{match}} = 5M$ in our calculation.

To apply Eq. (4.10), we need to obtain the dependence of the configuration on the amplitude A_1. For this purpose, we gradually increase A_1 from a small amplitude where the linear approximation is valid ($A_1 = 10^{-3}$) and calculate the 12 parameters for each value of A_1. When we solve the coupled nonlinear ordinary differential equations (4.7), we linearize them by expanding around an approximate solution. We guess the approximate solution by extrapolating the configuration from the previous step. The process is then repeated by solving a set of linearized equations expanded around the improved approximate solution until we confirm the convergence of the 12 parameters. The orthogonal collocation method is used when we perform the projection of nonlinear terms to (l, m)-harmonics (see Appendix. D). The θ and φ directions are discretized by 16 and 31points, respectively.

4.1.2 The evolution of a cloud for the fastest growing parameter set

In the following, we show the numerical calculation results with the method presented in the previous section. First, we present the result with the black hole spin $a/M = 0.99$ and axion mass $\mu M = 0.42$. We perform the calculation with three different potentials,

$$V(\phi) = \mu^2 \left(\frac{1}{2}\phi^2 - \frac{1}{4!}\phi^4 \right) , \tag{4.21}$$

$$V(\phi) = \mu^2 \left(\frac{1}{2}\phi^2 - \frac{1}{4!}\phi^4 + \frac{1}{6!}\phi^6 \right) , \tag{4.22}$$

$$V(\phi) = \mu^2 \left(1 - \cos\phi \right) , \tag{4.23}$$

---

[1]Appearance of different l modes comes from the difference between the spheroidal harmonics $S_{lm\omega}$ and spherical harmonics Y_{lm}. The former is written by the superposition of the latter with various l.
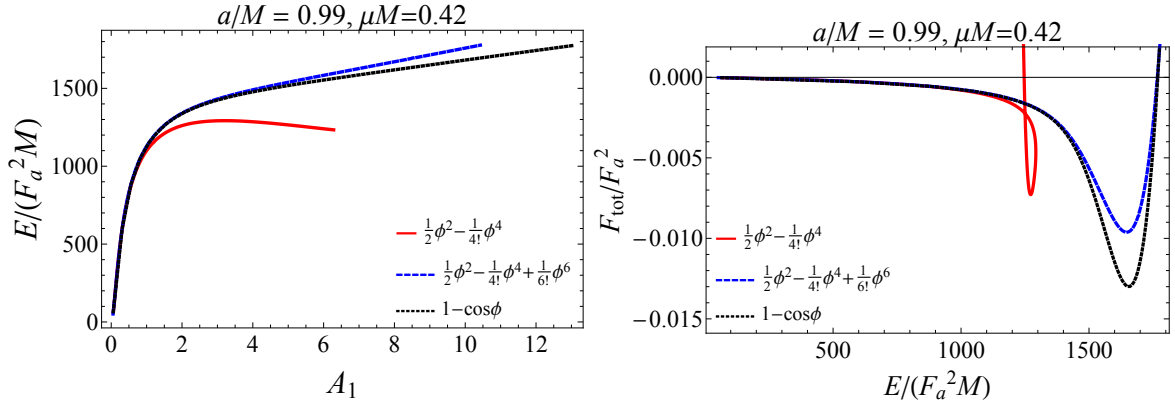
Figure 4.1: (Left) The energy of the configuration as a function of the amplitude A_1. The red solid, blue dashed, and black dotted curves correspond to the cases with the potentials Eqs. (4.21), (4.22), and (4.23), respectively. (Right) Relation between the total flux F_{tot} on the energy E. Same as the left panel, the red solid, blue dashed, and black dotted curves correspond to the respective choices of potential.
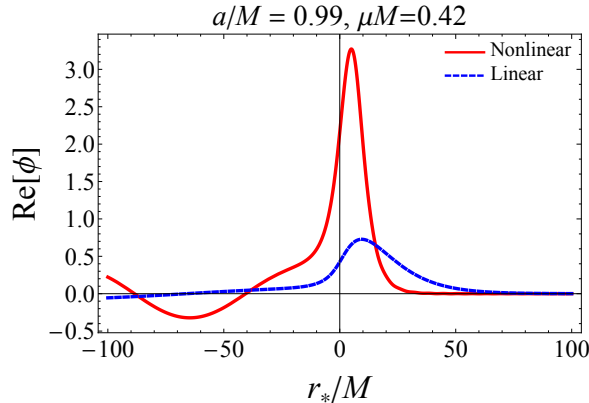

Figure 4.2: The real part of the axion field ϕ on the equatorial plane. The red and blue dashed curves show the nonlinear and the linear case, respectively. For the nonlinear case, we take potential to be the cosine potential (4.23). We fixed the energy to $E = 1768 F_a^2 M$, where the growth of the amplitude due to the superradiance saturates, in both cases,.

to see whether the higher-order terms of the potential have an influence on the result or not.

In Fig. 4.1, we show the energy E (left panel) and the total flux F_{tot} (right panel) of the configuration as a function of the A_1. We observe that the energy with the potential truncated at ϕ^4 (4.21) satisfies $dE/dA_1 = 0$ around $A_1 \sim 3$. As discussed in the context of the stellar instability [61], the appearance of a maximum of E indicates the existence of a dynamical instability at this amplitude. Later in Sec. 4.1.4, we will build a toy model which gives a physical picture of the presence of a maximum of E. This criterion of a dynamical instability implies that the axion condensate with the attractive ϕ^4 potential will become unstable at this amplitude. On the other hand, the condensate with the potential from the higher order terms (4.22) or (4.23) has no maximum, showing no evidence of the instability. Since the leading higher order term in the potential is repulsive, they stabilize the cloud.

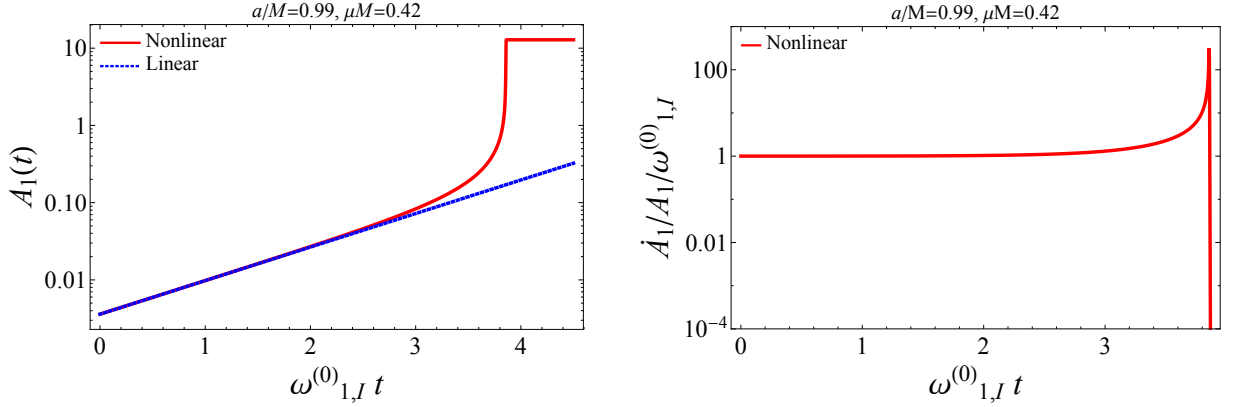In the early epoch, where the energy (amplitude) of the axion is small, the total

Figure 4.3: (Left) The time evolution of the amplitude A_1. The red solid curve and the blue dashed straight line show the nonlinear (cosine-type potential (4.23)) and the linear time evolutions, respectively. The horizontal axis time normalized by the growth rate in the linearized model $\omega_{1,I}^{(0)}$. We should emphasize that $\omega_{1,I}^{(0)}$ is, in general, different from the imaginary part of the frequency ω_1. (Right) The inverse time scale of the cloud evolution $\dot{A}_1/A_1$, normalized by $\omega_{1,I}^{(0)}$. Again, the horizontal axis is the normalized time, $\omega_{1,I}^{(0)}t$.
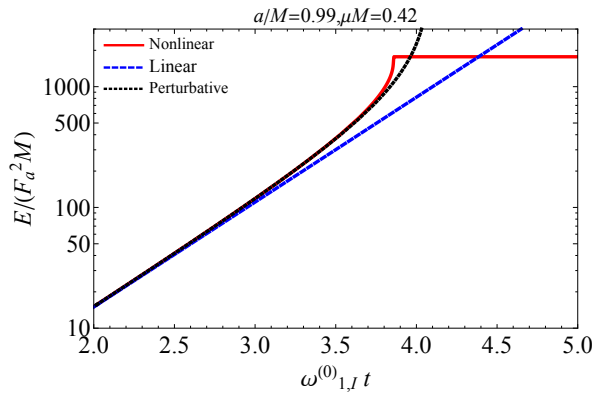
Figure 4.4: The same figure as the left panel of Fig. 4.3 but with the cloud energy E instead of the amplitude A_1. We added the black dashed line which corresponds to the evolution obtained by solving the perturbative equation (3.68).

energy flux is negative, which indicates the growth of the condensate (see Fig. 4.1). This is because the total energy is dominated by the negative energy flux at the horizon, superradiance. As the amplitude grows, the energy flux to the infinity starts to increase faster than the superradiance, and eventually, two fluxes balance to give $F_{\rm tot} = 0$ at $A_1 \sim 12$ or $E \sim 1.8 \times 10^3 F_a^2 M$. Thus the quasi-stationary configuration would be realized since the condensate is stable throughout the evolution for potentials (4.22) and (4.23). In Fig. 4.2, we show the quasi-stationary configuration of the axion field on the equatorial plane. We observe that the nonlinear configuration is more compact than the linear configuration at the same energy. This is because the leading ϕ^4 term in the cosine potential is attractive.

To obtain the time evolution of the amplitude A_1, we solve Eq. (4.10) using the relation between amplitude and the energy and the energy flux that we have just obtained. The time evolution of the amplitude A_1 is shown in the left panel of Fig. 4.3. In the early time, when the amplitude is small, the amplitude follows the linear evolution. When the
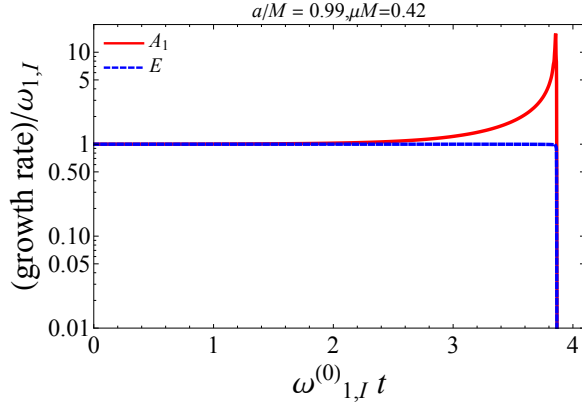
Figure 4.5: Growth rates of the cloud evolution. The Red solid and blue dotted curves correspond to the growth rate defined by $\dot{A}_1/A_1$ and $\dot{E}/2E$, respectively. We normalize the growth rate by the imaginary part of the frequency, $\omega_{1,I}$. Again, we mention that ω_1 is the fundamental frequency of the nonlinear configuration, not the frequency obtained by the linear analysis in Sec. 2.3, $\omega_1^{(0)}$.

amplitude gets larger, the growth is slightly accelerated, which is predicted by the perturbative calculation in Sec. 3.3. We can directly compare to the perturbative calculation by translating amplitude A_1 to the cloud energy E_1 and confirm the good agreement with the perturbative evolution for $E \lesssim 500$ (see Fig. 4.4). Eventually, the energy dissipation to infinity balances the superradiant growth and the acceleration stops. In the right panel of Fig. 4.3, we present the inverse time scale of the amplitude evolution. We observe that the growth rate is at most 100 times larger than the growth rate predicted by the linear analysis. However, our assumption on the adiabatic evolution (4.1) is still valid since there is large discrepancy between the original growth rate $\omega_{1,I}$ and the dynamical timescale $\omega_{1,R}$. There ratio is about $\omega_{1,I}/\omega_{1,R} \lesssim 10^{-7}$.

We further examine the consistency of our numerical method by comparing the imaginary part of ω_1 to the growth rate defined by the amplitude ($\dot{A}_1/A_1$) and the energy ($\dot{E}/2E$). In Fig. 4.5, the time evolution of these two growth rates normalized by the imaginary part of the frequency $\omega_{1,I}$ is shown. These ratios deviate from unity by at most $\mathcal{O}(10)$ until saturation occurs. That is to say, the growth rates defined in different ways differ by a tiny amount $\mathcal{O}(10\omega_{0I})$. This difference represents the error of our calculation scheme which comes from the naive ansatz (4.2). Therefore, when we substitute the solution of the form (4.2) with the time-dependent amplitude $A_1(t)$ into the equation of motion (3.3), the error should be comparable to $\omega_{1,I}$. Note that when we derive Eq. (4.7), we have neglected the time dependence of A_1. Now we can conclude that to correct this error, we only need tiny higher order corrections. We would like to mention that $\dot{E}/2E$ stays close to $\omega_{1,I}$ even when the amplitude is large and the nonlinear effect is not small.

4.1.3 Dependence on the axion mass and black hole spin

Next, we vary the black hole spin a/M and the axion mass μM to see how the variation of these parameters affects the evolution. Table 4.1 presents the parameter sets presented in this section. In the following, the axion potential is fixed to (4.23).

Let us first examine how the dependence of the energy E on amplitude A_1 is altered by changing the axion mass and the black hole spin. In Fig. 4.6, we show the function $E(A_1)$ for $\mu M = 0.29$ (left) and $\mu M = 0.15$ (right). For both cases, a local maximum of

41

Table 4.1: The five parameter set $(a/M, \mu M)$ we show in Sec. 4.1.3. For each parameter set, we show the real and the imaginary part of the frequency, $\omega_{1,R}$ and $\omega_{1,I}$, of the unstable mode when we neglect the self-interaction.

$(a/M, \mu M)$	$M\omega_{1,R}$	$M\omega_{1,I}$
(0.99,0.29)	0.2867	2.154×10^{-8}
(0.9,0.29)	0.2867	1.543×10^{-8}
(0.99,0.15)	0.1496	1.837×10^{-10}
(0.9,0.15)	0.1496	1.737×10^{-10}
(0.7,0.15)	0.1496	1.154×10^{-10}
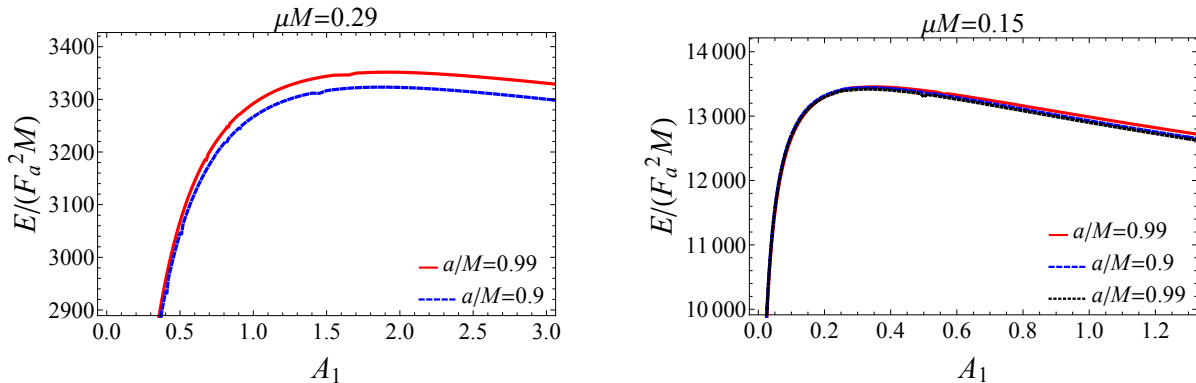
Figure 4.6: The same figure as the left panel of Fig. 4.1 but with different axion mass and black hole spin. The axion potential is fixed to cosine-type (4.23). (Left) The case with $\mu M = 0.29$. The red solid and blue dashed curves correspond to the $a/M = 0.99$ and $a/M = 0.9$ cases, respectively. (Right) The case with $\mu M = 0.15$. The red solid, blue dashed, and black dotted curves correspond to the $a/M = 0.99, a/M = 0.9$, and $a/M = 0.7$ cases, respectively.

E exists for any value of a/M. Therefore, the cloud is expected to be unstable if μM is not very large, independent of the value of a/m. In the next subsection, we introduce the toy model to explain the difference between the case $\mu M = 0.42$ and the cases $\mu M = 0.29$ and 0.15.

Next, we check whether the energy flux is large enough to saturate the condensate. Energy fluxes from the horizon and to infinity are shown in Fig. 4.7 ($\mu M = 0.29$ on the left and $\mu M = 0.15$ on the right). We observe that even when the cloud energy is large enough to cause the instability, the flux to infinity is much smaller than the flux from the horizon to terminate the growth. The suppression of the flux to infinity is explained by similar argument as suppression of the flux due to the high frequency radiation of the classification in Sec. 3.1. The reason is the wavelengths of the radiative modes are much smaller than the size of the flux. To summarize, for the small axion mass, the dissipation to infinity is inefficient to terminate the growth and the cloud becomes unstable at a certain amplitude.

4.1.4 Toy model of the bosenova

In this subsection, we give a toy model that explains the presence (absence) of the sign of instability, that is a local maximum of the energy, in the numerical calculation presented in previous subsection. Our model is based on the effective theory proposed in [37]. We
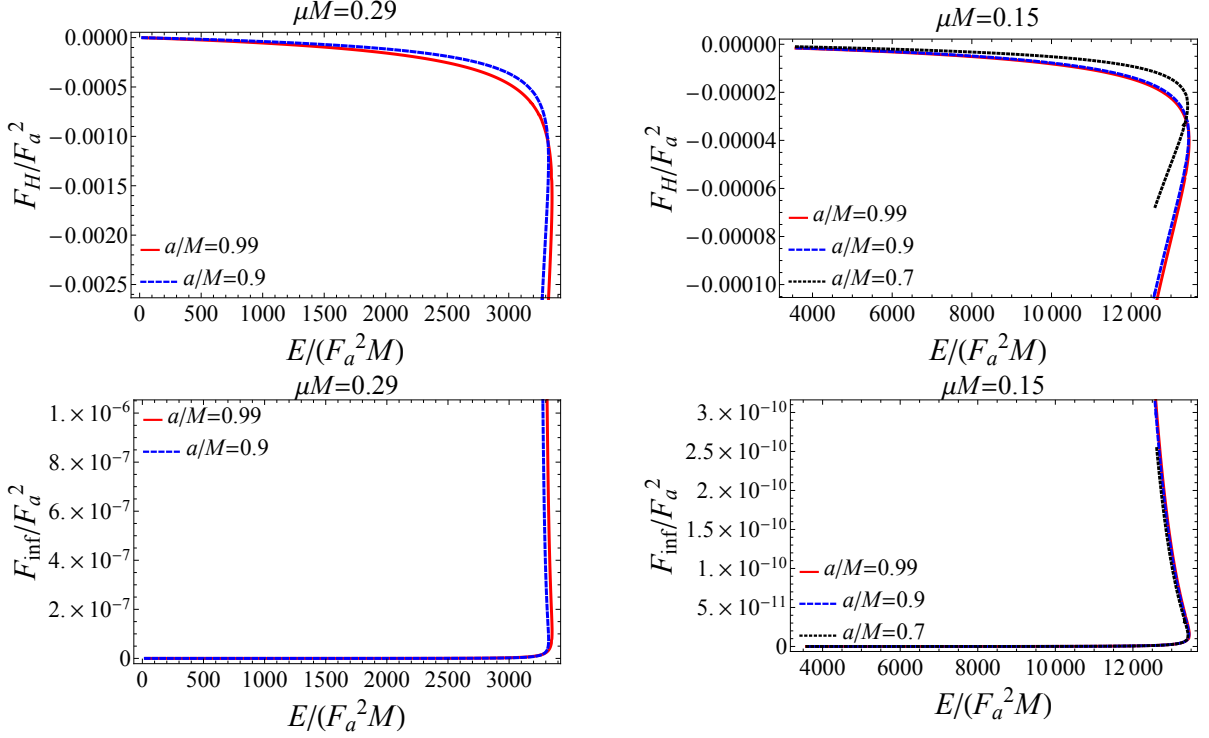
Figure 4.7: The energy fluxes at the horizon (upper panels) and infinity (lower panels) as the function of the energy of the cloud. The left and right panels correspond to the case with $\mu M = 0.29$ and $\mu M = 0.15$, respectively. energy flux at the infinity and the horizon, respectively. In the left panels, the red and the blue curves correspond to $a/M = 0.99$ and 0.9 cases, respectively. In the right panels, the red, blue, and black curves correspond to the $a/M = 0.99, a/M = 0.9$, and $a/M = 0.7$ cases, respectively.

assume the configuration of the axion field to be

$$\phi = \frac{1}{\sqrt{2\mu}} \left(\psi e^{-i\mu t} + \psi^* e^{+i\mu t} \right) \ , \tag{4.24}$$

and requires that the characteristic length scale of the function ψ be much longer than the axion Compton wavelength μ^{-1}. In addition, we ignore the spin of the BH and adopt the non-relativistic approximation $\mu M \ll 1$. Therefore, the first term of the expansion with respect to μM is preserved.

Our goal is to obtain the configuration of ψ and its dependence on μM. Under the above approximations, the action (3.1) recast to

$$S_{\mathrm{NR}} = F_a^2 \int dt\, d^3\boldsymbol{x} \ \left(\frac{i}{2} \left(\psi^* \dot{\psi} - \psi \dot{\psi}^* \right) - \frac{1}{2\mu} |\partial_i \psi|^2 + \frac{\mu M}{r} |\psi|^2 + \mu^2 \sum_{n=2} \frac{(-1/2)^n}{(n!)^2} \frac{|\psi|^{2n}}{\mu^n} \right) . \tag{4.25}$$

This non-relativistic action shows that the potential energy of the condensate is given by

$$V = \int d^3\boldsymbol{x} \ \left(\frac{1}{2\mu} |\partial_i \psi|^2 - \frac{\mu M}{r} |\psi|^2 - \mu^2 \sum_{n=2} \frac{(-1/2)^n}{(n!)^2} \frac{|\psi|^{2n}}{\mu^n} \right) . \tag{4.26}$$

Our numerical calculation in the previous subsection shows that a single spherical harmonics well approximates the configuration of the cloud. For this reason, we take an
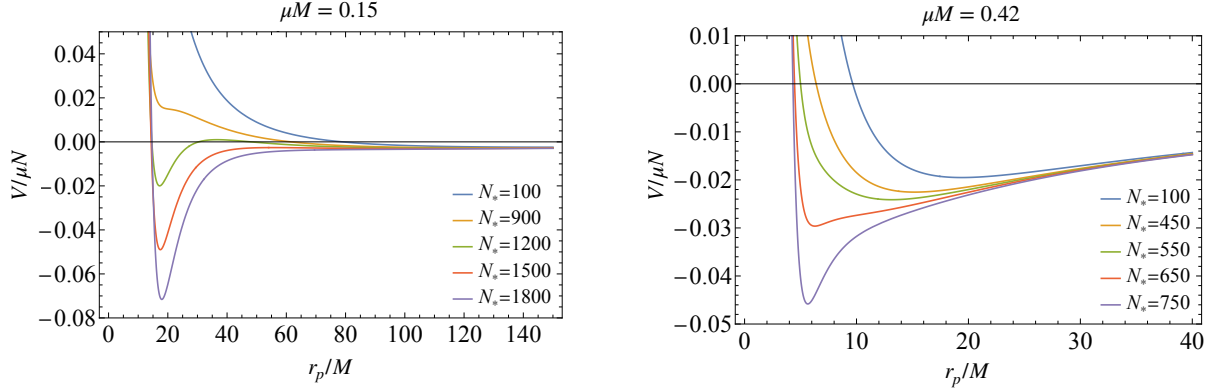
Figure 4.8: The potential $V/\mu N|_{\sigma=\sigma_{eq}}$ for different values of N_*. Each curve corresponds to a different value of N_*. The left and the right panel shows the case with $\mu M = 0.15$ and 0.42, respectively.

ansatz

$$\psi = A_p e^{-\frac{(r-r_p)^2}{4\sigma^2}} Y_{l_1 m_1}(x) e^{+im_1\varphi} \ . \tag{4.27}$$

The configuration (4.27) is characterized by the peak amplitude A_p, the position of the peak r_p, and the radial width of the condensate σ. We evaluate the potential energy (4.26) with the ansatz (4.27) and set $l_1 = m_1 = 1$ to obtain

$$\frac{V}{N} = \frac{r_p^2 + 3\sigma^2}{8\mu\sigma^2(r_p^2 + \sigma^2)} + \frac{1}{\mu(r_p^2 + \sigma^2)} - \frac{\mu M r_p}{r_p^2 + \sigma^2}$$
$$- \mu^2 \left(\frac{N_*}{160\pi\sqrt{2\pi}\mu^4\sigma(r_p^2 + \sigma^2)} - \frac{3N_*^2}{17920\pi^3\mu^7\sigma^2(r_p^2 + \sigma^2)^2} + \cdots \right) \ . \tag{4.28}$$

here, we defined the particle number N of the $l_1 = m_1 = 1$ mode in the condensate as

$$N = \int d^3\boldsymbol{x} \ |\psi|^2 \sim 2\pi\sqrt{2\pi}\sigma(r_p^2 + \sigma^2)A_p^2 \ , \tag{4.29}$$

where the inner cutoff of the radial integration is ignored. The radial integrations in Eq. (4.26) are approximated similarly. We also defined the dimensionless quantity $N_* \equiv \mu^2 N$.[2]

For each particle number N, the shape of the condensate is determined by the extremum of the potential (4.28), *i.e.*,

$$\partial_{r_p} V = \partial_\sigma V = 0 \ . \tag{4.30}$$

By eliminating N_* from these equations and solving for σ, we obtain the radial width of the equilibrium configuration σ_{eq} as

$$\sigma^2 = \sigma_{\text{eq}}^2 \equiv \frac{1}{6\mu^2 M} \left(-2r_p + \mu^2 M r_p^2 + r_p\sqrt{4 + 2\mu^2 M r_p + \mu^4 M^2 r_p^2} \right) \ . \tag{4.31}$$

---

[2]The correct particle number is given by $F_a^2 N$, since the axion field ϕ in our convention is normalized by the decay constant F_a. This normalization eliminated F_a from the equations. We introduced N_* by multiplying N by μ^2 instead of F_a^2 not to reintroduce F_a in the potential.
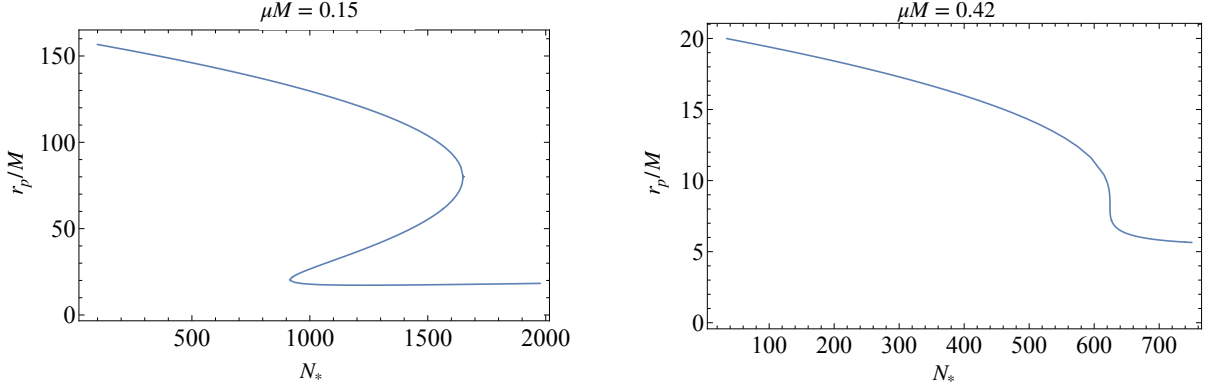
Figure 4.9: Dependence of the peak position r_p at the equilibrium on the N_*. The left and the right panel shows the case with $\mu M = 0.15$ and 0.42, respectively.
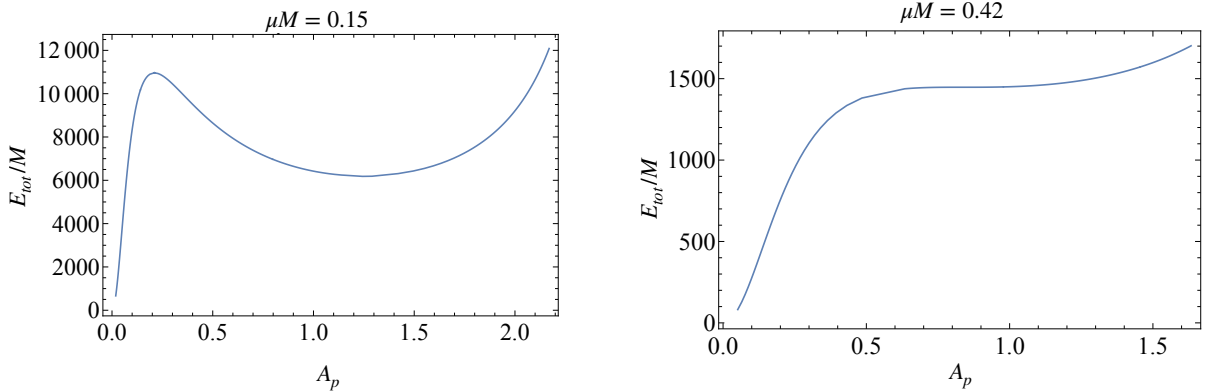

Figure 4.10: The total energy E_{tot} of equilibrium configuration as the function of the peak amplitude A_p. The left and the right panel shows the case with $\mu M = 0.15$ and 0.42, respectively.

After substituting σ_{eq} to Eq. (4.28), the potential energy is regarded as a function of the peak position r_p. In Fig 4.8, we show the dependence of $V/N|_{\sigma=\sigma_{eq}}$ on N_* with $\mu M = 0.15$ (left) and 0.42 (right). The value of r_p at the extremum of $V/N|_{\sigma=\sigma_{eq}}$, $r_{p,\text{eq}}$ shows the peak position of the condensate at the equilibrium. We show $r_{p,\text{eq}}$ as a function of N_* in Fig. 4.9. We also show how the total energy of the equilibrium configuration

$$E_{\text{tot}} = \mu N + V|_{\sigma=\sigma_{eq}} \tag{4.32}$$

depends on the peak amplitude A_p by translating N to A_p by Eq. (4.29), in Fig. 4.10.

First, we consider the case $\mu M = 0.15$. When $N_* \lesssim 900$, the dominant contribution to the potential is from the Newtonian potential and the angular momentum barrier. Thus, there exists a single extremum made by the Newtonian potential and the angular momentum barrier. The self-interaction gives a small correction to the potential. As we increase N_*, the attractive force of the leading ϕ^4 term in the self-interaction decrease r_p. At $900 \lesssim N_* \lesssim 1650$, three extrema appear: two stable points (the outer and the inner points) and one unstable point. The origin of the outer stable point is the same as the extremum in the region where N_* is small. The inner stable point and the unstable point appear due to the self-interaction. The leading attractive ϕ^4 and the sub-leading
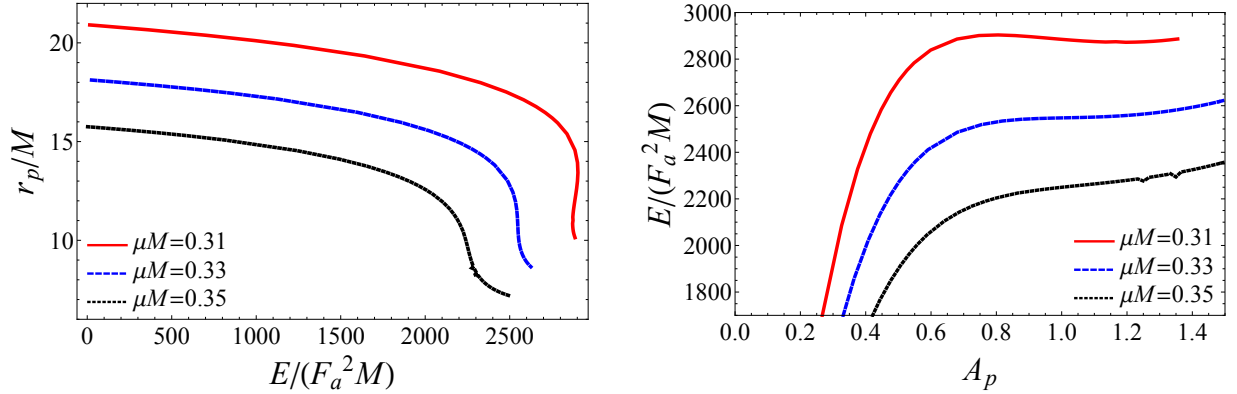
Figure 4.11: (Left) Red solid, blue dashed, and black dotted curves show the position of the peak of the fundamental mode $\tilde{R}_{11}$ as a function of the energy E for $\mu M = 0.31, 0.33$, and 0.35, respectively. The spin of the central black hole is fixed to $a/M = 0.99$. Different configurations with a given E can exist only for $\mu M = 0.31$ case. (Right) Red solid, blue dashed, and black dotted curves show the energy of the configuration at the extremum as a function of the peak amplitude of the fundamental mode $\tilde{R}_{11}$ for $\mu M = 0.31, 0.33$, and 0.35, respectively. A local maximum in this plot appears only for $\mu M = 0.31$ case.

repulsive ϕ^6 terms make the deep potential well in the small r_p region. When we further increase N_* to $N_* \gtrsim 1650$, the outer stable point disappears and only the inner stable point remains. Therefore, the condensate originally resides at the outer stable point in the small N_* jumps to the inner stable point when N_* reaches around $N_* \sim 1650$.

This jump would indicate the onset of a phase transition. Comparing the left panel of Fig. 4.10 with the right panel of Fig. 4.6, we can see that the pattern of instability is the same both in this toy model and in the numerical calculation in the previous subsection. This phase transition might be violent and lead to explosive phenomena such as bosenova. Since our calculation assumes the adiabatic evolution, we need to perform dynamical simulations to study the dynamics of the phase transition or the post-phase transition state.

We now examine the behavior for the case $\mu M = 0.42$. In contrast to the $\mu M = 0.15$ case, a single extremum exists regardless of value of N_*. As μM increases, the contribution of the Newtonian potential becomes larger. As a result, the radius at which gravity and centrifugal force are balanced becomes smaller than the small μM case. Then, it approaches the radius where the secondary minimum due to self-interaction appears. For sufficiently large μM, there is no more range of amplitudes where the two local minima coexist. In such a case, we expect no phase transition to occur. Then the condensate is stable throughout the evolution and eventually, the energy gained by the superradiance is balanced by the energy flux to infinity, which is not included in our toy model, at some N_*. This is consistent with the numerical calculations in the previous subsection.

The above discussion suggests the existence of a critical gravitational coupling $\mu_c M$ below which phase transition is expected. We numerically determine the critical value $\mu_c M$ by solving the nonlinear evolution of the axion condensate with different values of μM. Fig 4.11 shows the relation of the energy of the cloud and the peak position (left panel) and peak amplitude (right panel) of the fundamental mode $\tilde{R}_{11}$ for $\mu M = 0.31, 0.33$, and 0.35 with fixed $a/M = 0.99$. The corresponding figures obtained from the toy modes are Figs. 4.9 and 4.10. We observe from Fig 4.11 that the critical value should be around $\mu_c M \sim 0.32$.

4.2 Extension to the multiple modes

Now we extend our numerical scheme to include the second mode $(n_2, l_2, m_2) = (3, 2, 2)$. We write the axion field composed of the $l = m = 1$ cloud with the amplitude A_1 and the $l = m = 2$ cloud with the amplitude A_2 as

$$\phi(A_1, A_2) = \phi_1(A_1, A_2) + \phi_2(A_1, A_2) + \phi_r(A_1, A_2) . \tag{4.33}$$

Here, ϕ_1 corresponds to the $l = m = 1$ cloud and ϕ_2 corresponds to the $l = m = 2$ cloud. We also include excitations of the radiative modes (e.g. $(\omega, m) = (2\omega_2 - \omega_1^*, 3)$ and $(2\omega_1 - \omega_2^*, 0)$ modes) by ϕ_r.

Since the essential picture obtained from the perturbation theory analysis should be correct, the amplitude of the $l = m = 1$ cloud is larger than the $l = m = 2$ cloud in the situation that we are interested in. In such a situation, the $l = m = 2$ cloud self-interaction is weak and the $l = m = 1$ cloud deformation due to the $l = m = 2$ cloud can be safely neglected. But, of course, the nonlinear effect of $l = m = 1$ cloud cannot be ignored. With these considerations, we approximate the configuration as

$$\phi_1(A_1, A_2) = \phi_1(A_1) , \tag{4.34}$$
$$\phi_2(A_1, A_2) = A_2 \phi_2(A_1) , \tag{4.35}$$

neglecting all the nonlinear effects sourced by the ϕ_2 mode, except for excitations of the radiative modes. Then, the configuration of ϕ_1 is determined by solving

$$\Box_g \phi_1 - \mu^2 \sin \phi_1 = 0 , \tag{4.36}$$

independent of ϕ_2 and ϕ_r. We solve Eq. (4.36) with the method presented in the previous section.

With ϕ_1 given as a background, ϕ_2, and ϕ_r are determined by solving linearized equations of motion,

$$\Box_g \phi_2 - \mu^2 (\cos \phi_1) \phi_2 = 0 , \tag{4.37}$$
$$\Box_g \phi_r - \mu^2 (\cos \phi_1) \phi_r = S_r . \tag{4.38}$$

Here, S_r represents the source terms for the radiative modes given by

$$S_r = \mu^2 (\cos \phi_1) \phi_2 - \frac{\mu^2}{2} (\sin \phi_1) \phi_2^2 + \cdots . \tag{4.39}$$

When solving Eq. (4.37), we take an ansatz for ϕ_2 to be similar to ϕ_1 (see Eq. (4.2)), which is

$$\phi_2 = \sum_l e^{-i(\omega_2 t - m_2 \varphi)} \tilde{R}_l^2(r) Y_{l m_2}(x) + \text{c.c.} . \tag{4.40}$$

Substitution of the ansatz (4.40) to Eq. (4.37) and projection to the (l, m_2) harmonics

give

$$\frac{d}{dr}\left(\Delta \frac{d\tilde{R}_l^2}{dr}\right) + \left[\frac{(\omega_2(r^2+a^2)-am_2)^2}{\Delta} - \mu^2 r^2 + 2a\omega_2 m_2 - a^2\omega_2^2 - l(l+1)\right.$$

$$\left. + a^2(\omega_2^2 - \mu^2)\frac{1 - 2l(l+1) + 2(2m_2)^2}{3 - 4l(l+1)}\right]\tilde{R}_l^2$$

$$+ a^2(\omega_2^2 - \mu^2)\left(\frac{(l-1-2m_2)(l-2m_2)}{(2l-3)(2l-1)}\frac{N_{l-2}^{m_2}}{N_l^{m_2}}\tilde{R}_{l-2}^2\right.$$

$$\left. + \frac{(l+2+2m_2)(l+1+2m_2)}{(2l+3)(2l+5)}\frac{N_{l+2}^{m_2}}{N_l^{m_2}}\tilde{R}_{l+2}^2\right)$$

$$+ \int_0^{2\pi}\frac{d\varphi}{2\pi}\int_{-1}^1 dx\, Y_{lm_2}(x)e^{im_2\varphi}(r^2+a^2x^2)(1-\cos\phi_1)\phi_2 = 0 . \qquad (4.41)$$

This system of ordinary differential equations defines a two-point boundary value problem for finding the eigenvalue ω_2 assuming that the $l = 2$ component is dominant[3]. The boundary conditions are the same as in Eqs. (4.8) and (4.9), but (ω_1, m_1) is replaced by (ω_2, m_2). The normalization of the solution is arbitrary, but for later convenience, we choose a normalization such that the energy computed for ϕ_2 is unity in units of $F_a^2 M$.

Now that $\phi_1(A_1)$ and $\phi_2(A_1)$ are obtained, we can solve the equations for the radiative modes (4.38) in the same way as we obtained $\phi_2(A_1)$. Since we are interested in the excitations of the $m = 0$ and $m = 3$ modes, we project the equations to their respective components. This projection guarantees that ω is given by $2\omega_1 - \omega_2$ and $2\omega_2 - \omega_1$, for the respective modes[4].

The solution $\phi(A_1, A_2)$ obtained above is valid only for a short time and cannot describe the growth due to the superradiant instability. As in the previous section, we promote A_1 and A_2 to the time-dependent variables $A_1(t)$ and $A_2(t)$ to obtain a solution that can describe the instability. We determine the time development of these variables by the equations derived from the energy and angular momentum conservation laws, which are

$$\frac{dE(A_1, A_2)}{dt} = \frac{\partial E(A_1, A_2)}{\partial A_1}\frac{dA_1}{dt} + \frac{\partial E(A_1, A_2)}{\partial A_2}\frac{dA_2}{dt} = -F_E(A_1, A_2) , \qquad (4.42)$$

$$\frac{dJ(A_1, A_2)}{dt} = \frac{\partial J(A_1, A_2)}{\partial A_1}\frac{dA_1}{dt} + \frac{\partial J(A_1, A_2)}{\partial A_2}\frac{dA_2}{dt} = -F_J(A_1, A_2) . \qquad (4.43)$$

Here, the energy $E(A_1, A_2)$ and the energy flux $F_E(A_1, A_2)$ are evaluated by the similar formulas as Eqs. (4.11)-(4.14). The explicit formulas are

$$E(A_1, A_2) = \int dr\, d\cos\theta\, d\varphi\, (r^2 + a^2\cos^2\theta)\sqrt{g^{tt}}\, T_{\mu\nu}(A_1, A_2)\xi_{(t)}^\mu n_{(t)}^\nu , \qquad (4.44)$$

$$F_E(A_1, A_2) = F_E^H(A_1, A_2) + F_E^\infty(A_1, A_2) , \qquad (4.45)$$

$$F_E^H(A_1, A_2) = \int d\cos\theta d\varphi\, 2Mr_+ T_{\mu\nu}(A_1, A_2)\xi_{(t)}^\mu l^\nu|_{r=r_+} , \qquad (4.46)$$

$$F_E^\infty(A_1, A_2) = \int d\cos\theta d\varphi\, (r^2 + a^2\cos^2\theta)\sqrt{g^{rr}}\, T_{\mu\nu}(A_1, A_2)\xi_{(t)}^\mu n_{(r)}^\nu|_{r\to\infty} , \qquad (4.47)$$

---

[3]As mentioned previously, the solution consists of a superposition of various l harmonics, but it only describes a single mode. This is due to the fact that the elevation angle dependence of this mode is not given by a single component of an ordinary spherical harmonic.

[4]Here, we neglect the imaginary part of the frequency because it is much smaller than its real part due to the adiabatic nature of the evolution.
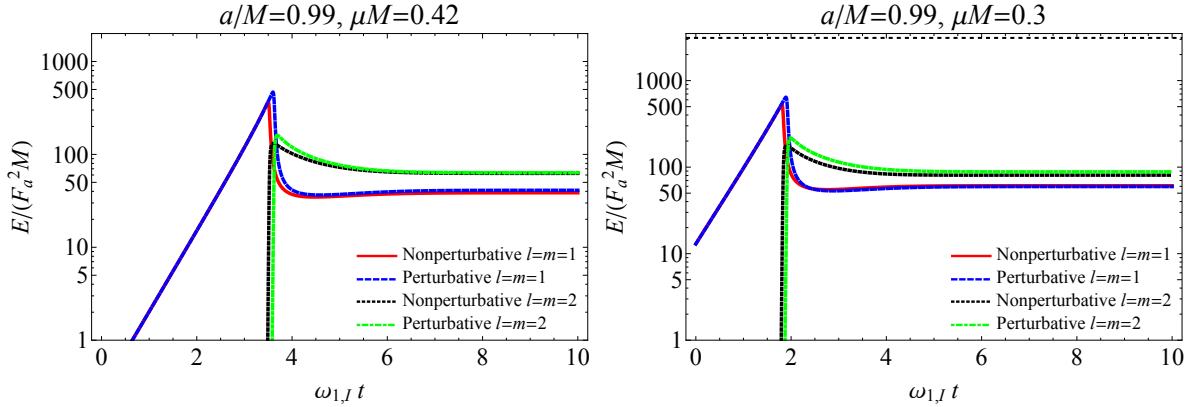
Figure 4.12: Comparison of time evolutions of the energy of the axion cloud in the non-perturbative and perturbative approaches. The left and right panels show the time evolution of the energy of the $l = m = 1$ and $l = m = 2$ cloud with $\mu M = 0.42$ and that with $\mu M = 0.3$, respectively. The red solid and black dotted lines correspond to the nonlinear evolution of the $l = m = 1$ and $l = m = 2$ clouds, respectively. The blue dashed and green dot-dashed lines show the same quantities but calculated with the perturbative method. We take the initial energy of the cloud to be $E_1 \sim 0.27 F_a^2 M$ $(12 F_a^2 M)$ for $\mu M = 0.42$ (0.3), and $E_2 = 10^{-8} F_a^2 M$. Time is normalized by $\omega_{1,I}$, the instability rate calculated from the linear analysis. Black dashed horizontal line around $E = 3000 F_a^2 M$ in the right panel indicates the energy where the $l = m = 1$ cloud is predicted to become unstable by the non-perturbative single mode calculation.

where $T_{\mu\nu}(A_1, A_2)$ is the energy-momentum tensor evaluated for the configuration given by $\phi(A_1, A_2)$. Again, the expressions for the angular momentum $J(A_1, A_2)$ and its flux $F_J(A_1, A_2)$ are obtained by replacing $\xi_{(t)}$ with $-\xi_{(\varphi)}$ in the above formulae for the energy. Note that under the assumptions (4.34) and (4.35), the total energy (4.44) is the summation of the energy of the $l = m = 1$ cloud and $l = m = 2$ cloud

$$E(A_1, A_2) = E_1(A_1) + E_2(A_1, A_2) . \tag{4.48}$$

Here, $E_1(A_1)$ and $E_2(A_1, A_2)$ is calculated from the energy-momentum tensor evaluated with $\phi_1(A_1)$ and $\phi_2(A_1, A_2)$, respectively. The cross term between ϕ_1 and ϕ_2 vanishes since ϕ_1 is superposition of (l, m) harmonics with odd m and ϕ_2 is that with even m. In addition, from the assumption 4.35, $E_2(A_1, A_2)$ is quadratic in A_2, i.e.,

$$E_2(A_1, A_2) = \hat{E}_2(A_1)|A_2|^2 . \tag{4.49}$$

4.2.1 Results

Figure 4.12 shows the time evolution of the amplitude calculated by the non-perturbative method explained in the current section and that by the perturbative method explained in Chapter 3, for $a/M = 0.99$ with $\mu M = 0.42$ and 0.3. The overall qualitative picture obtained from the perturbative method is reproduced in the non-perturbative case. In the early evolutionary phase, when the cloud energy is small, the non-perturbative and perturbative analyses follow the linear evolution track. As the cloud energy increases, the self-interactions begin to alter the evolution. In particular, dissipation by the interaction
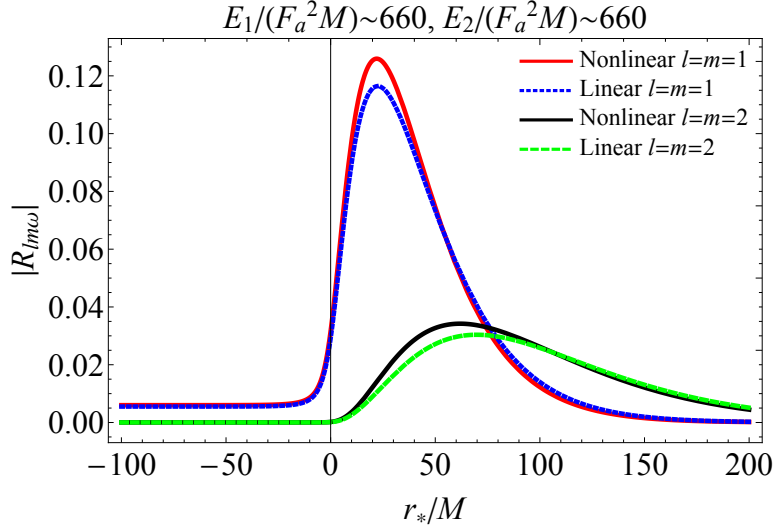
Figure 4.13: Snapshots of the absolute values of the radial mode functions in the perturbative and the non-perturbative evolutions. The red solid and black solid curves, respectively, show the absolute value of the mode function for the $l = m = 1$ mode and that for the $l = m = 2$ mode, when the self-interaction is taken into account non-perturbatively. The blue dotted and green dashed curves represent the same quantities but when the self-interaction is neglected. We set the energy of the cloud to be $E_1 \sim 660 F_a^2 M$, $E_2 = 660 F_a^2 M$, which is close to the peak value of E_1, in the right panel of Fig. 4.12. We choose the energy of the secondary cloud to be the same as the first one, just for convenience. The axion mass and the spin of the BH are set to $\mu M = 0.3$ and $a/M = 0.99$.

between the modes terminates the superradiant growth and eventually, the condensate settles to the quasi-stationary configuration. It should be noted that the amplitude of clouds is sufficiently small in the quasi-stationary state, and hence the entire field configuration is almost the same as that of the quasi-stationary state predicted by the perturbative calculation.

The quantitative difference appears in the peak energy, which is determined by the balance between the energy dissipations and the energy gain due to the superradiance. From Fig. 4.12, we find that the peak energy decreases by fully turning on the self-interaction. The mechanism that promotes this difference is the enhancement of dissipation, which can be understood as follows. Owing to the self-interaction, the two clouds attract each other (see Figure 4.13). The overlap between the two modes then increases. Since the dominant dissipative mode arises from a source composed of the product of these two modes, the increased overlap enhances dissipation in the nonlinear region.

Next, we examine how the time evolution of $l = m = 1$ clouds depends on the $E_2(t_{\rm ini})$, the energy of the $l = m = 2$ cloud at the initial time. Figure 4.14 shows examples of the time evolution of the primary $l = m = 1$ cloud for several values of $E_2(t_{\rm ini})$. As $E_2(t_{\rm ini})$ is reduced, the maximum energy of E_1 increases. Of course, in the limit of $E_2(t_{\rm ini}) \to 0$, the evolution of the $l = m = 1$ cloud is the same as that of the single cloud discussed in Sec. 4.1, and the bosenova can occur. Therefore, we are most interested in how sensitively the maximum energy of E_1 depends on the initial small energy of the secondary cloud $E_2(t_{\rm ini})$.

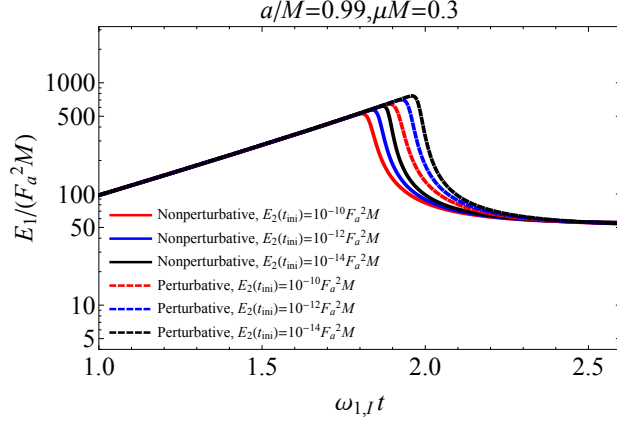There would be no need to consider nonlinear effects rigorously since an extremely

Figure 4.14: Dependence of the time evolution of the energy of the $l = m = 1$ mode on the initial energy of the $l = m = 2$ mode $E_2(t_{\text{ini}})$. The red, blue, and black solid lines show the energies of the $l = m = 1$ cloud, starting with $E_2(t_{\text{ini}})/(F_a^2 M) = 10^{-8}, 10^{-12}$, and 10^{-14}, respectively. The dotted lines with the same color represent the case when the self-interaction is treated perturbatively. The values of the axion mass and the BH spin are set to $\mu M = 0.42$ and $a/M = 0.99$.

small initial amplitude of the secondary cloud is sufficient as a seed. For this reason, we assume that the amplitude of the $l = m = 2$ cloud is kept small when we evaluate the maximum energy of the $l = m = 1$ cloud. By keeping only the leading terms of E_2, the evolution equations (4.42) and (4.43) are approximated as

$$\frac{dE_1}{dt} + \frac{dE_2}{dt} \sim -F_E^{\text{SR},1}(E_1) - F_E^{\text{diss}}(E_1)E_2 \ , \tag{4.50}$$

$$\frac{dJ_1}{dt} + \frac{dJ_2}{dt} \sim -\frac{1}{\omega_{1,R}}F_E^{\text{SR},1}(E_1) \ . \tag{4.51}$$

Here, $F_E^{\text{SR},1}(E_1)$ is the normalized energy flux at the horizon induced by the $l = m = 1$ mode and $F_E^{\text{diss}}(E_1)$ is that at the horizon by the $l = m = 0$ mode, for the unit energy of the $l = m = 2$ cloud ($E_2 = 1$). When the energy is small, we can use the perturbative method to calculate $F_E^{\text{SR},1}$ and $F_E^{\text{diss}}(E_1)$, which gives

$$F_E^{SR,1}(E_1) \sim -2\omega_{1,I}\left(1 - 6\lambda\text{Re}\left[C^{(1)}\right]E_1 + 12\lambda^2\text{Re}\left[\hat{C}^{(2)}\right]E_1^2\right)E_1 \ , \tag{4.52}$$

$$F_E^{\text{diss}}(E_1) \sim F_0 E_1^2 \ . \tag{4.53}$$

We neglect the energy flux at the horizon induced by the $l = m = 2$ mode since the superradiant instability of the $l = m = 2$ mode is much smaller than that of the $l = m = 1$ mode (see Sec. 2.2). Note that $F_E^{\text{SR},1}(E_1) < 0$ because the $l = m = 1$ mode extracts the energy flux from the black hole.

Owing to the helical symmetry of the configuration,

$$\frac{1}{\omega_i}\frac{\partial \phi_i}{\partial t} + \frac{1}{m_i}\frac{\partial \phi_i}{\partial t} = 0 \ , \tag{4.54}$$

we can directly calculate the variation of the energy and the angular momentum of each cloud and show the relation

$$\frac{\delta E_i}{\omega_{i,R}} = \frac{\delta J_i}{m_i} \ , \tag{4.55}$$

51

where we neglected $\omega_{i,I}$ since $\omega_{i,I} \ll \omega_{i,R}$. Then, we can simplify Eqs. (4.50) and (4.51) as

$$\frac{dE_1}{dt} \sim -F_E^{\text{SR},1}(E_1) - 2F_E^{\text{diss}}(E_1)E_2 , \tag{4.56}$$

$$\frac{dE_2}{dt} \sim F_E^{\text{diss}}(E_1)E_2 . \tag{4.57}$$

The maximum value of E_1 is determined by the condition $dE/dt = 0$, which leads to

$$-F_E^{\text{SR},1}(E_1^{\text{max}}) = 2F_E^{\text{diss}}(E_1^{\text{max}})E_2(t_{\text{max}}) , \tag{4.58}$$

where E_1^{max} denotes the maximum value of E_1 and t_{max} is the time when $E_1 = E_1^{\text{max}}$ is reached. Before E_1 gets sufficiently close to E^{max}, the approximation

$$\frac{dE_1}{dt} \sim -F_E^{\text{SR},1}(E_1) , \tag{4.59}$$

should be valid. Then, we can formally integrate Eq. (4.57) and get

$$E_2(t_{\text{max}}) = E_2(t_{\text{ini}}) \exp\left(\int_{E_1(t_{\text{ini}})}^{E_1^{\text{max}}} dE_1 \; g(E_1)\right) , \tag{4.60}$$

where

$$g(E_1) = -\frac{F_E^{\text{diss}}(E_1)}{F_E^{\text{SR},1}(E_1)} . \tag{4.61}$$

When evaluating the integral in , the take $E_1(t_{\text{tini}}) = 12F_a^2 M$, which is the same as the initial condition of Fig. 4.12. We would like to emphasize that taking E_1 below this value do not change the result because $g(E_1) \propto E_1$ for small E_1 (see Eqs. (4.52) and (4.53)). After the substitution of Eq. (4.60) into Eq. (4.2.1), we obtain

$$E_2(t_{\text{ini}}) = \frac{1}{2g(E_1^{\text{max}})} \exp\left(-\int_{E_1(t_{\text{ini}})}^{E_1^{\text{max}}} dE_1 \; g(E_1)\right) , \tag{4.62}$$

which approximates the initial energy of the secondary cloud $E_2(t_{\text{ini}})$ as a function of the maximum energy of the $l = m = 1$ cloud.

We show the relation between $E_2(t_{\text{ini}})$ and E_1^{max} in Fig. 4.15. For the range of initial conditions displayed in Fig. 4.14, our analytical estimate reproduces the peak energy with an error of 3%. As can be seen from Fig. 4.15, the actual peak value of the primary cloud energy is always smaller than the estimate from the perturbation calculation. This indicates that of the two effects of self-interaction, enhanced energy dissipation and accelerated growth, the former effect is always dominant.

To attain bosenova, $E_2(t_{\text{ini}})$ must be set to extremely tiny values. Indeed, when we set $E_1^{\text{max}} = E_1^{\text{BN}} \sim 3100$, which is the threshold for the dynamical instability at $\mu M = 0.3$ and $a/M = 0.99$ obtained by the single mode calculation presented in Sec. 4.1, the integral in the exponent Eq. (4.62) is evaluated as

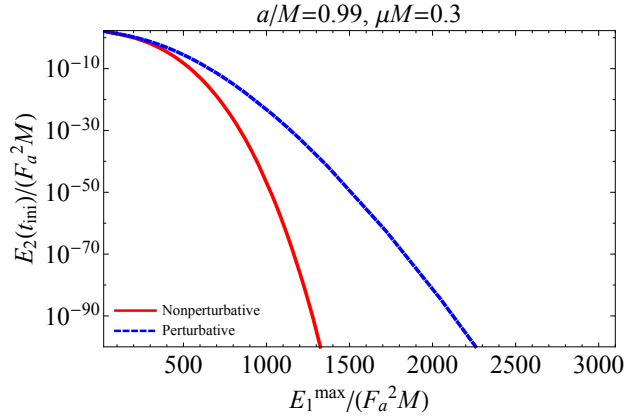$$\int_{E_1(t_{\text{ini}})}^{E_1^{\text{BN}}} dE_1 \; g(E_1) \sim 3.9 \times 10^3 . \tag{4.63}$$

Figure 4.15: Relation between the maximum value of energy of the $l = m = 1$ mode in the time evolution E_1^{max} and the initial energy of the $l = m = 2$ mode $E_2(t_{\mathrm{ini}})$. The red solid and blue dashed curves show the relations obtained by solving Eq. (4.62) under the nonperturbative scheme and the perturbative approximation, respectively. The perturbative curve is calculated with approximate expressions (4.52) and (4.53)

Therefore, $E_2(t_{\mathrm{ini}})$ must be an extremely small quantity multiplied by a factor $\exp(-3.9 \times 10^3)$. Even if the $l = m = 2$ cloud starts with a single axion particle (the number of excited particles is 1), $E_2(t_{\mathrm{ini}}) \sim 10^{-70} F_a^2 M$ (see equation (3.74)). This is far beyond the small upper bound of the initial energy required for the bosenova to happen. Note that the Hawking temperature of the rotating black hole is given by [62]

$$ T_H = \frac{1 - \frac{a^2}{r_+^2}}{8\pi M} \ . \tag{4.64} $$

For the astrophysical black hole, the upper bound of the inverse of the Hawking temperature is given by $T_H^{-1} < 211M$ (we adopted the "Throne limit" $a < 0.998$ [63]). For the axion mass in the range $\mu M \lesssim 1$, the thermal radiation of the axion field from the black hole is not sufficiently suppressed such that the initial cloud to be sufficiently vacant for the bosenova to happen.

Chapter 5

Late-time evolution with various perturbative processes

In the previous section, we confirmed that the axion condensate consisting of two clouds settles into a quasi-stationary state even though nonlinear effects are fully taken into account. In this chapter, we investigate whether or not the quasi-stationary state we have obtained would subsequently disappear due to other effects. These effects include quantum processes and excitation processes of other modes (overtone modes or higher multipole modes), which cannot be captured by the classical two mode analysis in the previous chapters 3 and 4.

5.1 Quantum process

First, let us consider quantum processes. The "quantum processes" here are those that cannot be described by the classical equations of motion (3.3). An example of the simplest quantum process is shown in Fig. 5.1. The important point is that this type of process involves more than two empty states. To see if a quantum process can compete with the classical processes, such as processes in Fig. 3.2, we first identify what is the effective reduced Planck constant in the present context. For a moment, we recover $G = M_{pl}^{-2}$. The action (3.1) in terms of non-dimensional quantities normalized by the length scale GM is given by

$$S = \left(\frac{F_a}{M_{pl}}\right)^2 \left(\frac{M}{M_{pl}}\right)^2 \int d^4\hat{x}\sqrt{-g}\left\{-\frac{1}{2}g^{\mu\nu}\hat{\partial}_\mu\phi\hat{\partial}_\nu\phi - \hat{\mu}^2\left(1 - \cos\phi\right)\right\} . \qquad (5.1)$$

Here, the quantities with "^" are non-dimensional, *i.e.* $\hat{\mu} = G\mu M$, $\hat{x} = x/M$, $\hat{\partial}_\mu = \partial/\partial\hat{x}^\mu$. From the above expression, we find the combination $M_{pl}^4/F_a^2/M^2$ acts as the effective reduced Planck constant. When the nonlinear effects are important, the amplitude of the condensate is $|\phi| \sim 1$. In such a situation, the difference in the amplitude of the classical processes and the quantum processes should be solely determined by the effective Planck constant. Thus, the quantum processes must be suppressed by the factor

$$\left(\frac{M_{pl}}{F_a}\right)^2 \left(\frac{M_{pl}}{M}\right)^2 \sim 10^{-96} \left(\frac{M_{pl}}{F_a}\right)^2 \left(\frac{M_\odot}{M}\right)^2 . \qquad (5.2)$$

In fact, one can directly calculate the rate for the process in Fig. 5.1 and show that this process is suppressed by the factor $F_a^2 M^2/M_{pl}^4$, compared to processes (a) and (b)
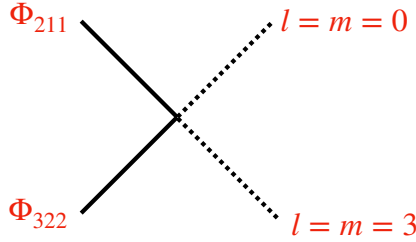
Figure 5.1: The simplest quantum process induced by the self-interaction.

in Fig. 3.2. The quantity (5.2) is extremely small for astrophysical black holes unless F_a takes a significantly small value, which is unlikely for string axions. Hereafter, we only focus on processes that can be described by the classical equations of motion.

5.2 Excitation of other modes

In chapter 4, we confirmed that the quasi-stationary configuration could be well approximated by a linearized solution whose amplitude is determined by the balance between processes (a) and (b) in Fig. 3.2. Therefore, it is safe to neglect the deformation of clouds due to self-interaction when discussing the subsequent evolution. We use the linearized solution to describe the quasi-stationary configuration in the following calculations. For the same reasons as in chapter 3, we will only consider excitations of low-frequency radiation and non-superradiant dissipative modes (see Sec. 3.1 for their definitions).

So far, we have considered an axion condensate that starts with only two component clouds belonging to the $l = m = 1$ and $l = m = 2$ fundamental modes. However, quantum fluctuations should seed all modes with small amplitude. Therefore, the source terms of the nonlinear interaction that contain processes involving other modes, such as overtone modes and higher multipole modes can be relevant. These processes have been extensively studied in Ref. [42] under the non-relativistic approximation $\mu M \ll 1$. Here, we extend the analysis to the relativistic regime $\mu M \sim 1$.

5.2.1 Excitation of $l = m = 1$ overtones

First, let us include an overtone mode $(n > 2)$ of the $l = m = 1$ multipole. We denote the frequency of the overtones as ω_o. We determine the possibly excited modes by writing down the source terms of the first-order perturbation equation with respect to λ (see chapter 3 for a similar discussion on the interaction between the $(\omega, m) = (\omega_1, 1)$ and $(\omega_2, 2)$ modes). As as in Sec. 3.1, we can select the relevant processes for the dissipation of the quasi-stationary configuration by the frequency ω and the angular quantum number m of the excited mode. The conditions for (ω, m) are (i) $\omega \gtrsim \mu$ (low frequency radiation), or (ii) $\omega < \mu$ and $\omega > m\Omega_H$ (non-superradiant dissipative mode). Note that the leading contribution to energy dissipation comes from the case in which the excited mode has the lowest orbital angular momentum in the acceptable range. In the following, we focus on the most dominant modes relevant to energy dissipation. We summarize the processes under consideration in Fig. 5.2.

The essential difference from the interaction between the $l = m = 1$ and $l = m = 2$ fundamental modes is in that no process transfers the energy to the secondary modes, i.e., $l = m = 1$ overtone modes. In particular, process (e) of Fig. 5.2 shows a noticeable
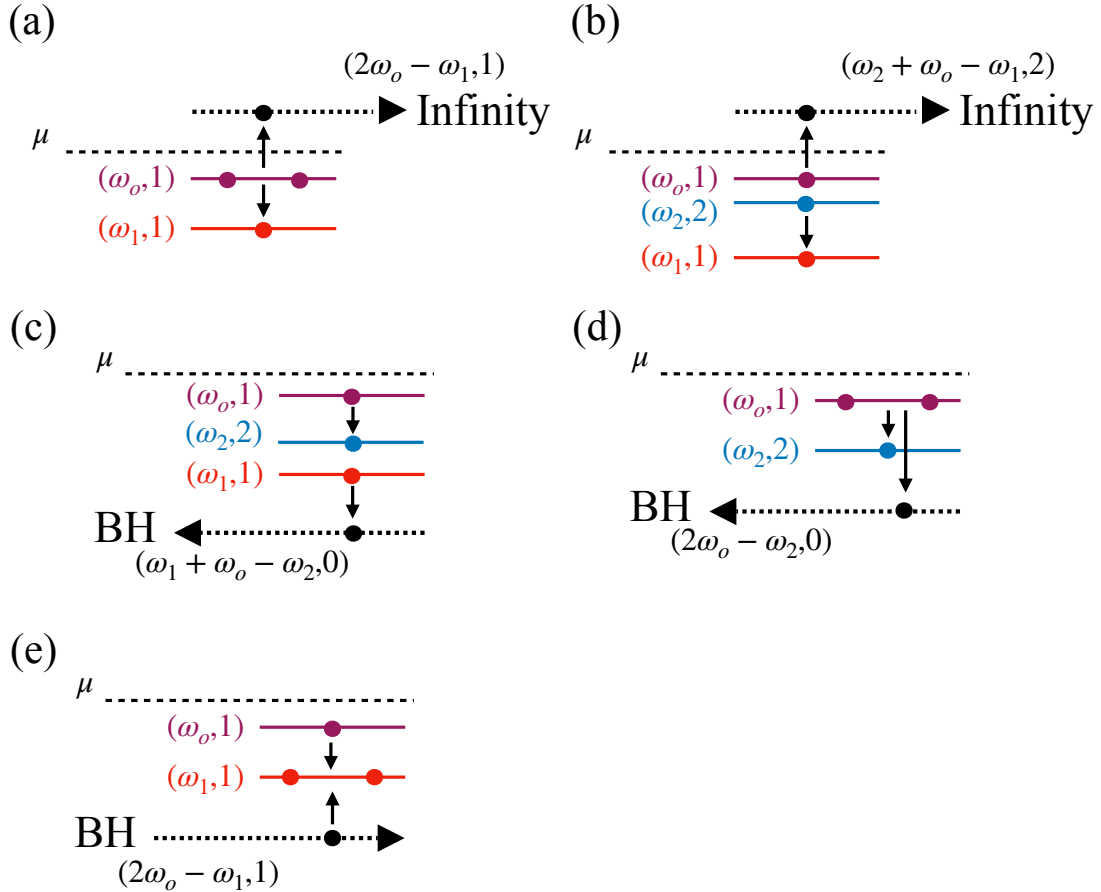
Figure 5.2: The dissipative processes when the $l = m = 1$ overtone modes are taken into account. The top two diagrams ((a) and (b)) correspond to the processes that dissipate energy to infinity. The bottom three diagrams ((c), (d), and (e)) correspond to the processes that dissipate energy to the central black hole. The direction of the flux to the black hole is opposite for process (e), since the excited $(2\omega_o, 1)$ mode satisfies the superradiance condition. As in Fig. 3.2, we only consider the excited modes having the smallest possible l.

difference. The corresponding process in Sec. 3.2 is one described by the left panel of Fig. 3.2, which dissipates the $l = m = 1$ fundamental mode and feeds the $l = m = 2$ fundamental mode. On the other hand, process (e) of Fig. 5.2 generates the $l = m = 1$ fundamental mode from a $l = m = 1$ overtone. This is because the excited mode has $m = 1$ and satisfies the superradiant condition (2.9). Thus, the energy is not lost but extracted from the BH, which indicates that the direction of the transition and hence that of the energy flow is opposite. The presence of this process is why we could have concluded that $l = m = 1$ overtones decay in the two mode approximation adopted in Sec. 3.2.

Here, we should also notice that the production of an overtone mode from the $l = m = 2$ mode is absent, in contrast to the production of the $l = m = 1$ fundamental mode from the $l = m = 2$ mode (see right diagram in Fig. 3.2). The reason is that the other excited modes are bounded, i.e. $2\omega_2 - \omega_o < \mu$. [1] In summary, the interaction between an $l = m = 1$ overtone mode and the $l = m = 1$ or $l = m = 2$ fundamental

[1]Under the non-relativistic approximation, where the real part of the frequency can be approximately
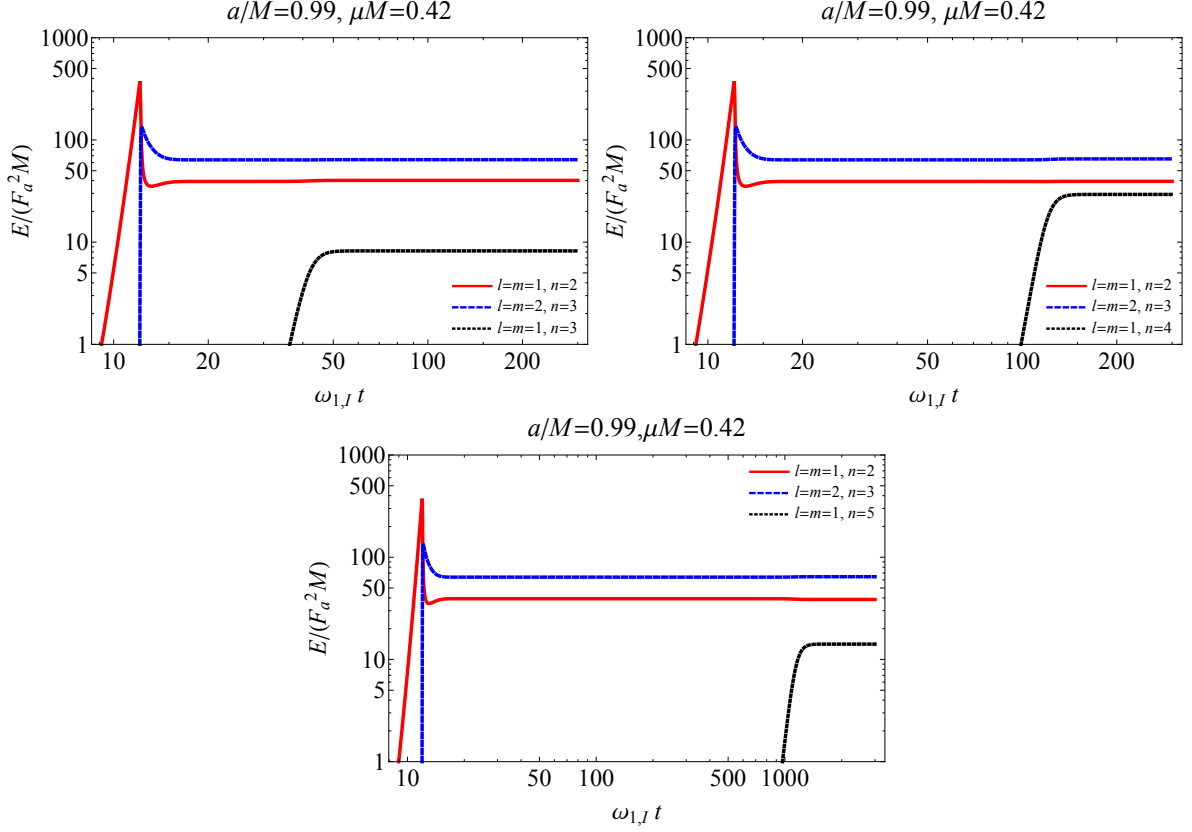
Figure 5.3: Examples of the time evolution including an $l = m = 1$ overtone mode. The red solid and blue dotted lines correspond to the $l = m = 1$ and $l = m = 2$ fundamental modes. The black dashed line corresponds to the overtone mode. From left to right, the label n of the overtone modes is varied from 3 to 5. The horizontal axis is the time normalized by the superradiant instability rate of the $l = m = 1$ fundamental mode. We set the axion mass and the BH spin to $\mu M = 0.42$ and $a/M = 0.99$.

mode always dissipates the overtone mode. Therefore, overtone modes can grow only by the superradiant instability in the early epoch, and eventually, the dissipation due to the mode-mode interaction begins to decelerate the instability.

Similarly to the method in Sec. 3.1, the time evolution equations with an overtone mode can be derived from the local energy and angular momentum conservation laws.

---

estimated by using the well-known result for the hydrogen atom,

$$2\omega_2 - \omega_o = 2\mu\left(1 - \frac{(\mu M)^2}{2\times 3^2}\right) - \mu(1 - \frac{(\mu M)^2}{2n^2}) = \mu\left(1 - (\mu M)^2\left(\frac{1}{3^2} - \frac{1}{2n^2}\right)\right) < \mu\,, \qquad (5.3)$$

for $n \geq 3$.

The coupled evolution equations of the three clouds are given by

$$
\begin{aligned}
\frac{dE_1}{dt} =&\, 2\omega_{1,I}E_1 - \frac{2\omega_{1,R}}{2\omega_{1,R}-\omega_{2,R}}F_0 E_1^2 E_2 + \frac{\omega_{1,R}}{2\omega_{2,R}-\omega_{1,R}}F_3 E_1 E_2^2 \\
&+ \frac{\omega_{1,R}}{2\omega_{o,R}-\omega_{1,R}}F_{1^*oo}E_1 E_o^2 + \frac{\omega_{1,R}}{\omega_{2,R}+\omega_{o,R}-\omega_{1,R}}F_{1^*2o}E_1 E_2 E_o \\
&- \frac{2\omega_{1,R}}{2\omega_{1,R}-\omega_{o,R}}F_{11o^*}E_1^2 E_o - \frac{\omega_{1,R}}{\omega_{1,R}+\omega_{o,R}-\omega_{2,R}}F_{12^*o}E_1 E_2 E_o \;,
\end{aligned}
\tag{5.4}
$$

$$
\begin{aligned}
\frac{dE_2}{dt} =&\, 2\omega_{2,I}E_1 + \frac{\omega_{2,R}}{2\omega_{1,R}-\omega_{2,R}}F_0 E_1^2 E_2 - \frac{2\omega_{2,R}}{2\omega_{2,R}-\omega_{1,R}}F_3 E_1 E_2^2 \\
&- \frac{\omega_{2,R}}{\omega_{2,R}+\omega_{o,R}-\omega_{1,R}}F_{1^*2o}E_1 E_2 E_o \\
&+ \frac{\omega_{2,R}}{2\omega_{o,R}-\omega_{2,R}}F_{2^*oo}E_2 E_o^2 + \frac{\omega_{2,R}}{\omega_{1,R}+\omega_{o,R}-\omega_{2,R}}F_{12^*o}E_1 E_2 E_o \;,
\end{aligned}
\tag{5.5}
$$

$$
\begin{aligned}
\frac{dE_o}{dt} =&\, 2\omega_{o,I}E_o - \frac{2\omega_{o,R}}{2\omega_{o,R}-\omega_{1,R}}F_{1^*oo}E_1 E_o^2 - \frac{\omega_{o,R}}{\omega_{2,R}+\omega_{o,R}-\omega_{1,R}}F_{1^*2o}E_1 E_2 E_o \\
&+ \frac{\omega_{o,R}}{2\omega_{1,R}-\omega_{o,R}}F_{11o^*}E_1^2 E_o - \frac{2\omega_{o,R}}{2\omega_{o,R}-\omega_{2,R}}F_{2^*oo}E_2 E_o^2 \\
&- \frac{\omega_{o,R}}{\omega_{1,R}+\omega_{o,R}-\omega_{2,R}}F_{12^*o}E_1 E_2 E_o \;.
\end{aligned}
\tag{5.6}
$$

Here, E_o is the energy of the overtone mode. The coefficients F_{abc} in Eqs. (5.4) - (5.6) are the values of the energy flux of the diagrams in Fig. 5.2 with the energy of each cloud contained in the source term set to $F_a^2 M$. For example, F_{1^*2o} corresponds to process (b) in Fig. 5.2, given by

$$
\begin{aligned}
F_{1^*2o} =&\, 144\pi\lambda^2 \omega_3' \sqrt{(\omega_3')^2-\mu^2} \sum_{l\geq 2}\Bigg| \frac{1}{W_{l2}(\omega_3')} \int dr' d\cos\theta' (r'^2 + a^2\cos^2\theta') R^{\rm in}_{l2\omega_3'} \\
&\times R_1^*(r')^* R_2(r') R_o(r') S_1^*(\theta') S_2(\theta') S_o(\theta') \Bigg|^2 \;,
\end{aligned}
\tag{5.7}
$$

where $\omega_3' = \omega_2 + \omega_o - \omega_3$.

The time evolution of the three mode system consisting of $(n,l,m) = (2,1,1)$, $(3,2,2)$, and $(n,1,1)$ mode is shown in Fig. 5.3 for $n = 3, 4$, and 5. As expected from the above discussion, the overtone modes initially accumulates by the superradiance, and eventually, the growth saturates at the point where the dissipation balances the superradiance. We observe that the growth of the $n = 5$ cloud delays compared to the $n = 3$ and $n = 4$ overtones. This is because the difference between the growth rate of the superradiance and the dissipation rate caused by the processes involving only one overtone mode in the source term (processes (b) and (c) in Fig. 5.2) becomes small as one increases n. In fact, it can be numerically confirmed that the dissipation rate is faster than the growth rate due to superradiance for $n \geq 6$. In other words, the growth of the $l = m = 1$ overtone as shown in Fig. 5.3 occurs only for $n \leq 5$. Interestingly, the time evolution of the energies of the $l = m = 1$ and $l = m = 2$ fundamental modes is almost unchanged. This is because the dissipation of $l = m = 1$ overtones is so strong that the overtones do not dominate the entire condensate.
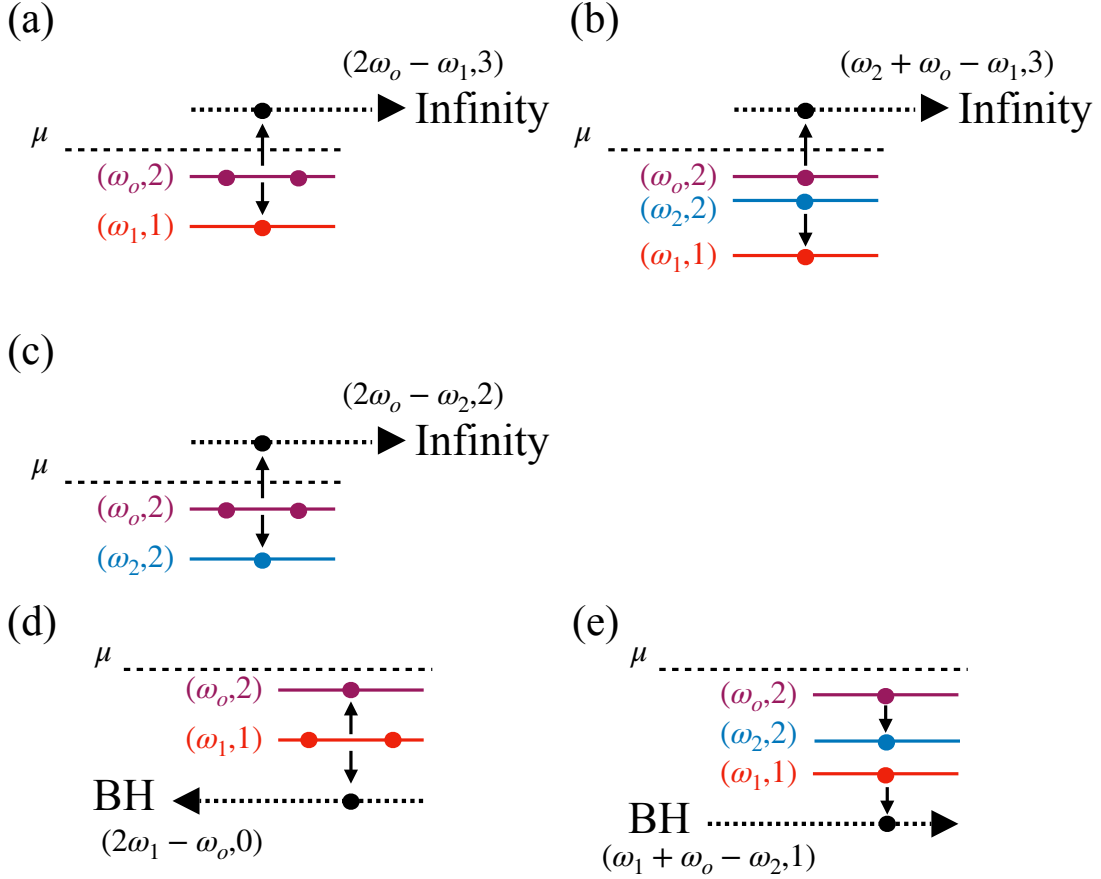
Figure 5.4: The processes involved when overtone modes of $l = m = 2$ are included. The top three diagrams ((a), (b), and (c)) correspond to the processes which dissipate energy to infinity. The bottom two diagrams ((d) and (e)) correspond to the processes that dissipate energy to the BH. Since $2\omega_o - \omega_2 > \mu$ holds only for $n \geq 5$, the process specified by the diagram (c) can dissipate energy only for $n \geq 5$.

5.2.2 Excitation of $l = m = 2$ overtones

Next, we consider the excitation processes of $l = m = 2$ overtones. We summarize the relevant processes in Fig. 5.4. The main difference from $l = m = 1$ overtones in that there is a process that excites the $l = m = 2$ overtones from the $l = m = 1$ fundamental mode (process (d) in Fig. 5.4). This process is the same as the generation process of the $l = m = 2$ fundamental mode (left panel in Fig. 3.2). However, owing to the smaller overlap between the $l = m = 1$ fundamental mode and the $l = m = 2$ overtones compared to that between the $l = m = 1$ and $l = m = 2$ fundamental modes, the growth of $l = m = 2$ overtones is suppressed compared to the growth of $l = m = 2$ fundamental modes. Thus, the condensate first reaches a quasi-stationary configuration consisting of $l = m = 1$ and $l = m = 2$ fundamental modes. At this point, the energy of the $l = m = 2$ overtones is much smaller than that of the fundamental modes.

For $l = m = 2$ overtones to continue to grow even after the fundamental modes reach the quasi-stationary configuration, the growth rate of $l = m = 2$ overtones must remain larger than its dissipation rate. Since the energy of $l = m = 2$ overtones is small even after the growth of the fundamental modes saturates, it is sufficient to consider the terms linear in E_o in Eq. (5.6). Keeping only the terms linear in E_o, the evolution equation for
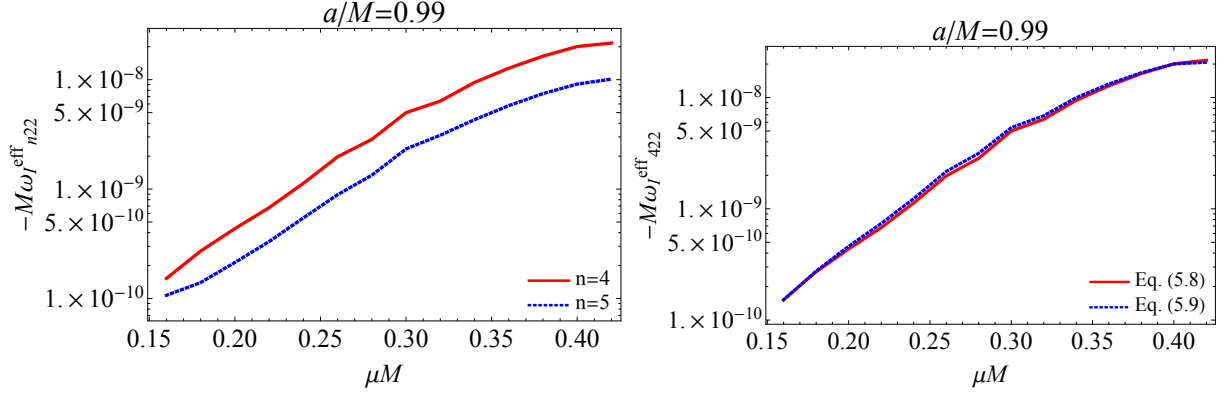
Figure 5.5: (Left) The dependence of $\omega_{n22,I}^{\text{eff}}$ on the axion mass μM. The red solid and blue dotted lines correspond to the case with $n = 4$ and $n = 5$, respectively. The spin of the central BH is set to $a/M = 0.99$. (Right) The same figure but taking into account the correction by the $l = m = 1$ overtone mode. The red solid line is same as that in the left panel. The blue dotted lines show $\omega_{422,I}^{\text{eff}}$ calculated by Eq. (5.9), respectively. When calculating $\omega_{422,I}^{\text{eff}}$ with Eq. (5.9), we take into account the cloud composed of the $l = m = 1, n = 4$ mode that has the largest energy in the quasi-stationary configuration at a late time among clouds composed of $l = m = 1$ overtones.

an $l = m = 2$ overtone takes the form of

$$
\begin{aligned}
\frac{dE_o}{dt} &\sim \left[2\omega_{o,I} - \left(\frac{\omega_{o,R}}{\omega_{2,R} + \omega_{o,R} - \omega_{1,R}} F_{1^*2o} + \frac{\omega_{o,R}}{\omega_{1,R} + \omega_{o,R} - \omega_{2,R}} F_{12^*o} \right) E_1^{\text{qs}} E_2^{\text{qs}} \right. \\
&\quad \left. + \frac{\omega_{o,R}}{2\omega_{1,R} - \omega_{o,R}} F_{11o^*} \left(E_1^{\text{qs}} \right)^2 \right] E_o \\
&\equiv 2\omega_{n22,I}^{\text{eff}} E_o \ .
\end{aligned}
\tag{5.8}
$$

Here, E_1^{qs} and E_2^{qs} are the energies of the $l = m = 1$ and $l = m = 2$ clouds in the quasi-stationary state, which can be determined by the perturbative analysis in chapter 3 in a good approximation. If $\omega_{o,I}^{\text{eff}} < 0$ holds, the $l = m = 2$ overtone cannot grow. In Fig. 5.5, we show the behavior of $\omega_{o,I}^{\text{eff}}$ for $n = 4$ and 5. The figure shows that $\omega_{n22,I}^{\text{eff}}$ is always negative, indicating that no accumulation of $l = m = 2$ overtones occurs. We present examples of the time evolution for the three mode system composed of $(n, l, m) = (2, 1, 1), (3, 2, 2)$, and $(n, 2, 2)$ with $n = 4$, and 5 in Fig. 5.6. As expected from the above discussion, the $l = m = 2$ overtone clouds decrease after the $l = m = 1$ and $l = m = 2$ fundamental modes reach the quasi-stationary configuration.

However, it is premature to conclude that there is no growth of $l = m = 2$ overtones. As shown in Sec. 5.1, $l = m = 1$ overtones can grow after the growth of the fundamental modes saturates (see Fig. 5.3). In this case, the other processes caused by the interaction involving both the $l = m = 1$ and the $l = m = 2$ overtones come into play. The relevant processes for the $n = 4, l = m = 2$ mode are shown in Fig. 5.7. These processes modify
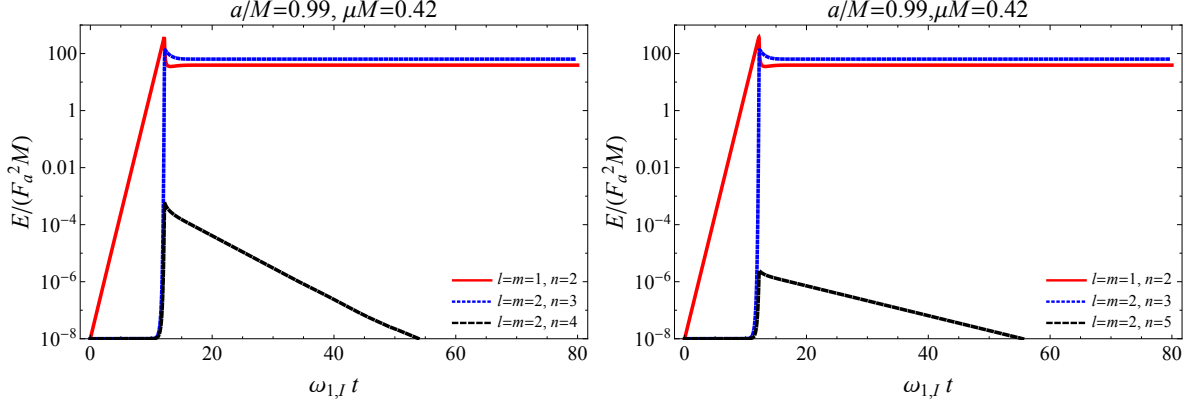
Figure 5.6: The same figures as Fig. 5.3, but with $l = m = 2$ overtones instead of $l = m = 1$ overtones. The black dashed lines in the left and right panels correspond to the $l = m = 2$ overtone with $n = 4$ and $n = 5$, respectively.

the $\omega_{n22,I}^{\mathrm{eff}}$ defined in Eq. (5.8) to

$$
\begin{aligned}
2\omega_{n22,I}^{\mathrm{eff}} =\ & 2\omega_{o_2,I} - \left(\frac{\omega_{o_2,R}\, F_{1^*2o_2}}{\omega_{2,R} + \omega_{o_2,R} - \omega_{1,R}} + \frac{\omega_{o_2,R}\, F_{12^*o_2}}{\omega_{1,R} + \omega_{o_2,R} - \omega_{2,R}} \right) E_1^{\mathrm{qs}} E_2^{\mathrm{qs}} \\
& + \frac{\omega_{o_2,R}\, F_{11o_2^*}}{2\omega_{1,R} - \omega_{o_2,R}} \left(E_1^{\mathrm{qs}} \right)^2 + \frac{\omega_{o_2,R}\, F_{o_1 o_1 o_2^*}}{2\omega_{o_1,R} - \omega_{o_2,R}} \left(E_{o_1}^{\mathrm{qs}} \right)^2 \\
& + \left(\frac{\omega_{o_2,R}\, F_{1o_1 o_2^*}}{\omega_{1,R} + \omega_{o_1,R} - \omega_{o_2,R}} - \frac{\omega_{o_2,R}\, F_{1^*o_1 o_2}}{\omega_{o_1,R} + \omega_{o_2,R} - \omega_{1,R}} \right) E_1^{\mathrm{qs}} E_{o_1}^{\mathrm{qs}} ,
\end{aligned}
\tag{5.9}
$$

where the subscripts o_1 and o_2 correspond to overtones of $l = m = 1$ and $l = m = 2$, respectively. In addition, $E_1^{\mathrm{qs}}, E_2^{\mathrm{qs}}$, and $E_{o_1}^{\mathrm{qs}}$ represent the energies of the $(n, l, m) = (2, 1, 1), (3, 2, 2), (n, 1, 1)$ modes in the quasi-stationary configuration of the system consisting of these three modes. If the terms involving $E_{o_1}^{\mathrm{qs}}$ in Eq (5.9) is larger than the negative contribution from Eq. (5.8), the $l = m = 2$ overtone can overcome the dissipation and grow. The right panel of Fig 5.5 shows that even with the $l = m = 1$ overtone, $\omega_{422,I}^{\mathrm{eff}}$ is also always negative which indicates that the $l = m = 2$ overtone does not grow. This result can be explained by the fact that the energy of the $l = m = 1$ overtone $E_{o_1}^{\mathrm{qs}}$ is smaller than that of the fundamental modes E_1^{qs} and E_2^{qs}. The fluxes with the source involving the $l = m = 1$ overtone are small compared to the fluxes sourced by the fundamental modes.

5.2.3 Excitation of higher multipole modes

Finally, we consider the excitation of higher multipole modes. The analysis is performed in parallel with the excitation of overtone modes. Specifically, we focus on higher-order multipole modes with $l = m = 3$ and $n = 4$. Figure 5.8 shows the relevant processes incorporated in the numerical evolution that is presented below. Similar to $l = m = 2$ overtone modes, the $l = m = 3$ fundamental mode is generated by the interaction between $l = m = 1$ and $l = m = 2$ fundamental modes (processes (c) and (e) in Fig. 5.8). At the same time, the $l = m = 3$ mode dissipates through the process shown in diagram (a).

The $l = m = 3$ fundamental mode can grow only in the parameter region where the production is more efficient than the dissipation. In a similar manner to $\omega_{n22,I}^{\mathrm{eff}}$ in Eq.
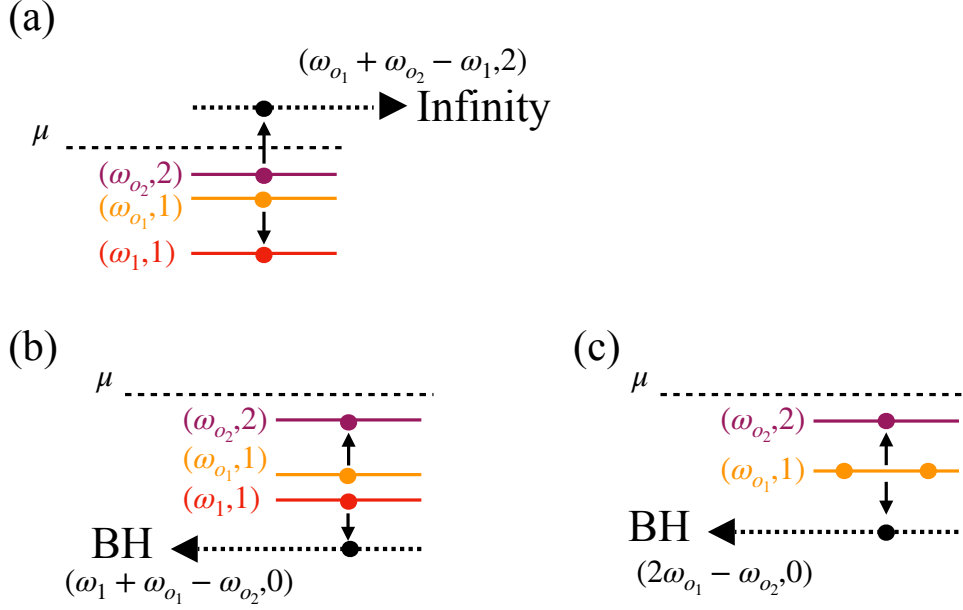
Figure 5.7: Processes for the interaction between the $l = m = 1$ overtone modes (subscript o_1) and the $l = m = 2$ overtone modes (subscript o_2) . The top diagram (a) describes a process that dissipates energy to infinity. The bottom two diagrams ((b) and (c)) describe processes that dissipate energy to the BH.

(5.8), we define the effective growth rate of the $l = m = 3$ fundamental mode $\omega_{433,I}^{\mathrm{eff}}$ as

$$
\begin{aligned}
2\omega_{433,I}^{\mathrm{eff}} \equiv {} & 2\omega_{h_3,I} + \frac{\omega_{h_3,R}}{2\omega_{1,R} - \omega_{h_3,R}} F_{11h_3^*} E_1^{\mathrm{qs}2} \\
& + \left(-\frac{\omega_{h_3,R}}{\omega_{2,R} + \omega_{h_3,R} - \omega_{1,R}} F_{1^*2h_3} + \frac{\omega_{h_3,R}}{\omega_{1,R} + \omega_{2,R} - \omega_{h_3,R}} F_{12h_3^*} \right) E_1^{\mathrm{qs}} E_2^{\mathrm{qs}} .
\end{aligned}
\tag{5.10}
$$

Here, the subscript h_3 stands for the $l = m = 3$ fundamental mode. In the left panel of Fig. 5.9, we show the value of $\omega_{433,I}^{\mathrm{eff}}$ as a function of μM. The sign of $\omega_{433,I}^{\mathrm{eff}}$ is determined as a result of competition between the leading two comparable contributions represented by processes (a) and (c) ($F_{1^*2h_3}$ and $F_{12h_3^*}$). We present dependence of $F_{1^*2h_3}$ and $F_{12h_3^*}$ on μM in the right panel of Fig. 5.9. For most of the axion mass μM, the dissipative process of the $l = m = 3$ fundamental mode (process (a) in Fig. 5.8, correspondingly $F_{1^*2h_3}$) dominates resulting in $\omega_{433,I}^{\mathrm{eff}} < 0$. In such cases, the $l = m = 3$ cloud cannot be excited (see, for example, the right panel of Fig. 5.10). On the other hand, for $0.12 \lesssim \mu M \lesssim 0.24$, the excitation process of the $l = m = 3$ fundamental mode (process (c) in Fig. 5.8, correspondingly $F_{12h_3^*}$) dominates and we have $\omega_{433,I}^{\mathrm{eff}} > 0$. Hence, the growth of the $l = m = 3$ cloud is expected. In the left panel of Fig. 5.10, we show the evolution of cloud energies for $\mu M = 0.16$. We observe that the $l = m = 3$ cloud eventually dominates the whole condensate.

The behavior of $\omega_{433,I}^{\mathrm{eff}}$ comes from the enhancement of $F_{1^*2h_3}$ around $0.12 \lesssim \mu M \lesssim 0.15$ and relative suppression for $\mu M \gtrsim 0.15$ (see right panel of Fig. 5.9). In particular, pivot around the $\mu M \sim 0.15$ is the key. Since $F_{1^*2h_3}$ is the flux by $m = 0$ mode, its behavior can be understood by looking at the effective potential of the $m = 0$ mode function. We define the effective potential V_{eff} by transforming the radial equation (2.12) to the Schrödinger
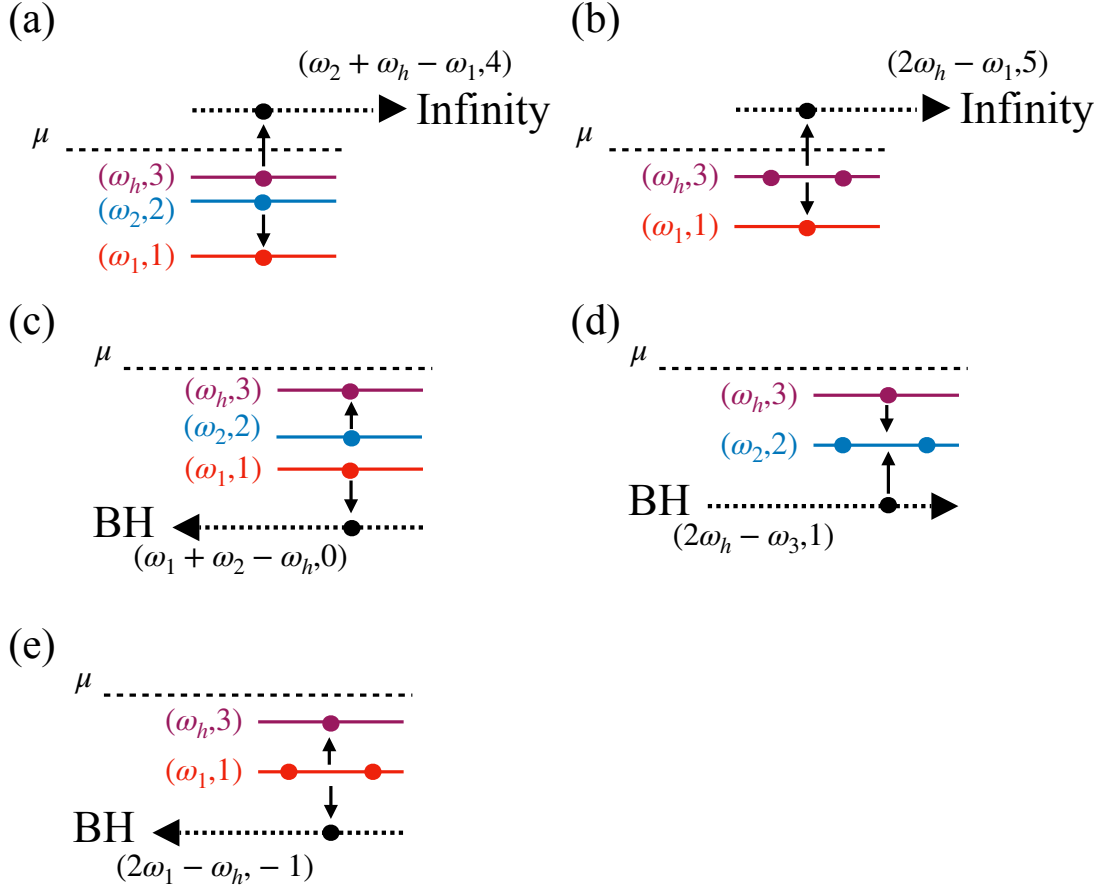
Figure 5.8: Relevant processes involving the $l = m = 1$, the $l = m = 2$ and the $l = m = 3$ fundamental modes. The subscript h denotes the $l = m = 3$ fundamental mode. The top two diagrams ((a) and (b)) describe the processes in which the energy of the excited unbounded modes are dissipated to infinity, and the bottom three ((c), (d), and (e)) describe the ones in which the excited modes are absorbed by the horizon.

form

$$\frac{d^2 u}{dr_*^2} + (\omega^2 - V_{\text{eff}})u = 0 \ . \tag{5.11}$$

Here, u is related to the radial mode function $R_{lm\omega}$ by

$$u \equiv \sqrt{r^2 + a^2} R_{lm\omega} \ . \tag{5.12}$$

The actual expression of V_{eff} is given by

$$V_{\text{eff}} = \frac{-a^2 m^2 + 4amMr\omega}{(a^2 + r^2)^2} + \frac{\Delta \mu^2}{a^2 + r^2} + \frac{\Delta \left(a^2 \left(\omega^2 - \mu^2\right) + \Lambda_{lm}(\omega)\right)}{(a^2 + r^2)^2}$$
$$+ \frac{\Delta \left(a^2 - 4Mr + 3r^2\right)}{(a^2 + r^2)^3} - \frac{3\Delta^2 r^2}{(a^2 + r^2)^4} \ . \tag{5.13}$$

Figure 5.11 shows the effective potential of the $l = m = 0$ mode excited by process (c) of Fig. 5.8 for various values of μM. For $\mu M \lesssim 0.1$, the frequency of this $m = 0$ mode is much smaller than the potential barrier. Thus, the energy flux to the horizon
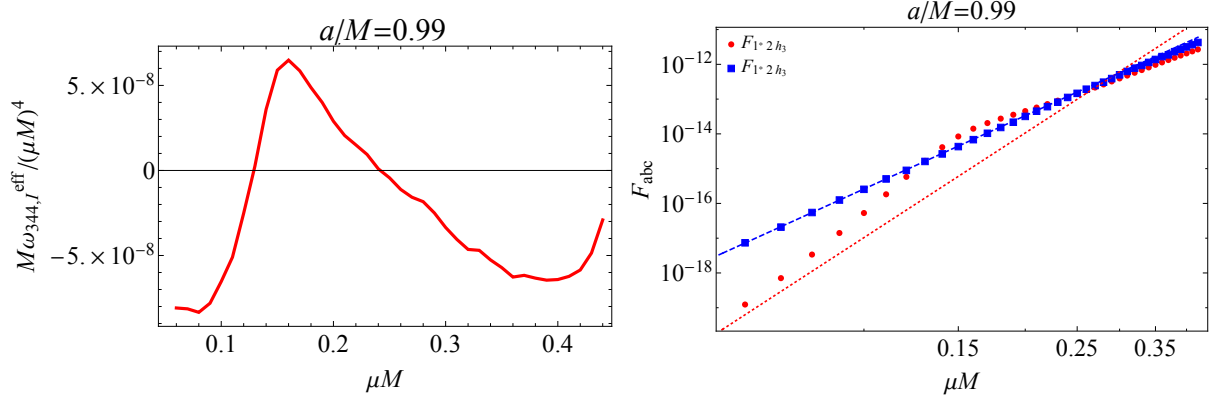
Figure 5.9: (Left) Dependence of $\omega_{433,I}^{\mathrm{eff}}/(\mu M)^4$ on μM, as shown in Fig. 5.5 for $\omega_{422,I}^{\mathrm{eff}}$. We fixed the spin of the central BH to $a/M = 0.99$. (Right) Dependence of $F_{1^*2h_3}$ and $F_{12h_3^*}$ on μM. The red circle and the blue square correspond to the numerically evaluated values of $F_{1^*2h_3}$ and $F_{12h_3^*}$, respectively. The red dotted and blue dashed lines correspond to $F_{1^*2h_3}$ and $F_{12h_3^*}$, evaluated in the non-relativistic limit $\mu M \ll 1$ (see Appendix C for its evaluation).
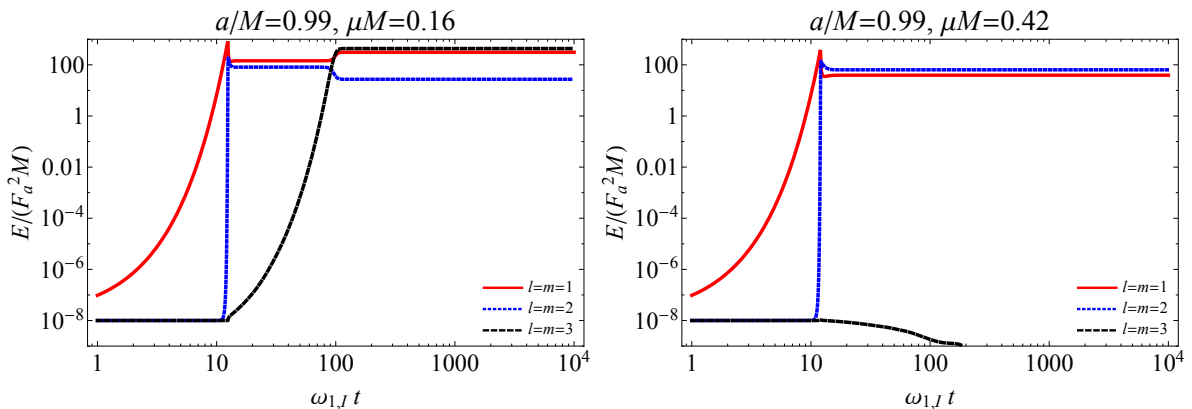
Figure 5.10: The same figures as Fig. 5.3, but with the fundamental $l = m = 3$ mode as the third mode, instead of $l = m = 1$ overtones. The left and right panels correspond to the case with $\mu M = 0.16$ and 0.42, respectively.

is suppressed. On the other hand, when $\mu M \gtrsim 0.1$, the axion mass begins to lower the potential barrier. [2] Thus the dissipative process involving the $m = 0$ mode becomes relatively faster as one increases μM. However, beyond $\mu M \sim 0.16$, the potential barrier goes below the frequency of the $m = 0$ mode. Therefore, significant enhancement of the flux does not occur even if we increase the axion mass. This explains the pivot of $F_{12h_3^*}$ around the $\mu M \sim 0.15$.

In a similar manner, we study the excitation of the $l = m = 4$ fundamental mode. The relevant processes are shown in Fig. 5.12. The main difference from interaction with the $l = m = 3$ fundamental mode is the presence of the process that dissipates the $l = m = 4$ mode and excites the $l = m = 2$ mode (process (d) in Fig. 5.12), owing to $\omega_R^{(544)} > \omega_R^{(433)}$.

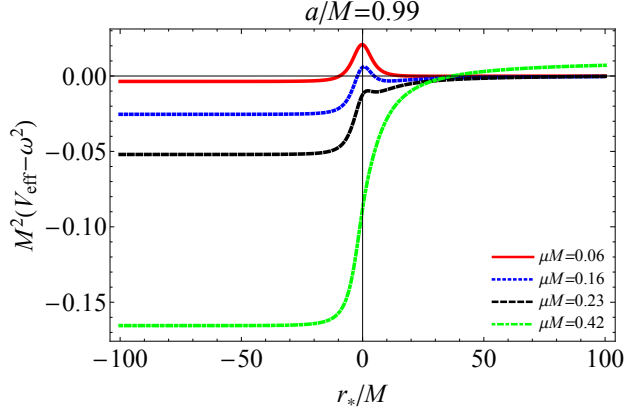[2]Note that frequency of the $m = 0$ mode varies with the axion mass μ.

65

Figure 5.11: The effective potential for the $l = m = 0$ mode function. The red solid, blue dotted, black dashed, and green dotted-dashed lines corresponds to the effective potential of the $l = m = 0$ mode function with $\mu M = 0.06, 0.16, 0.23$, and 0.42. The spin of the central BH is set to $a/M = 0.99$.

The effective growth rate for the $l = m = 4$ fundamental mode is given by

$$
2\omega_{544,I}^{\text{eff}} \equiv 2\omega_{h_4,I} + \frac{\omega_{h_4,R}}{2\omega_{1,R} - \omega_{h_4,R}} F_{11h_4^*} E_1^{\text{qs2}} + \frac{\omega_{h_4,R}}{2\omega_{2,R} - \omega_{h_4,R}} F_{22h_4^*} E_2^{\text{qs2}}
$$
$$
+ \left(-\frac{\omega_{h_4,R}}{\omega_{2,R} + \omega_{h_4,R} - \omega_{1,R}} F_{1^*2h_4} + \frac{\omega_{h_4,R}}{\omega_{1,R} + \omega_{2,R} - \omega_{h_4,R}} F_{12h_4^*} \right) E_1^{\text{qs}} E_2^{\text{qs}} .
$$

$$(5.14)$$

In Fig. 5.13, we show the $\omega_{544,I}^{\text{eff}}$ as a function of μM. We observe that $\omega_{544,I}^{\text{eff}} < 0$ for $\mu M \lesssim 0.2$. Therefore, the $l = m = 4$ fundamental mode decay in this range of the axion mass. On the other hand, for $\mu M \gtrsim 0.2$, we have $\omega_{544,I}^{\text{eff}} > 0$, which indicates the growth of the $l = m = 4$ fundamental mode. The example of the time evolution for $\mu M = 0.16$ and 0.42 are shown in Fig. 5.13. We see a behavior expect from the sign of $\omega_{544,I}^{\text{eff}}$, for $\mu M = 0.16$, the $l = m = 4$ fundamental mode decays and for $\mu M = 0.42$, it grows.

We have some overlapping regions where both the $l = m = 3$ and $l = m = 4$ modes can grow, $0.2 \gtrsim \mu M \lesssim 0.24$. For this case, we need to perform the calculation by considering 4-state at the same time. Of course, the number of interaction processes gets more significant, and thus the calculation becomes more and more complicated. Hence, we leave the examination in this region for future work.

Lastly, we consider the multipole with $m \geq 5$. The key process for the excitation of the additional mode is the excitation of the $m = 0$ mode since this process has a large flux owing to a small angular momentum barrier. However, the interaction between the $l = m = 1, l = m = 2$ and $m \geq 5$ modes cannot generate the $m = 0$ mode. Therefore, these modes cannot be excited, at least in the 3-state approximation adopted in the current chapter. After the $l = m = 3$ or $l = m = 4$ modes are excited, it might be possible for them to excite. Again, to analyze such a situation, we need to handle four or more clouds simultaneously. We also leave this case for future work.
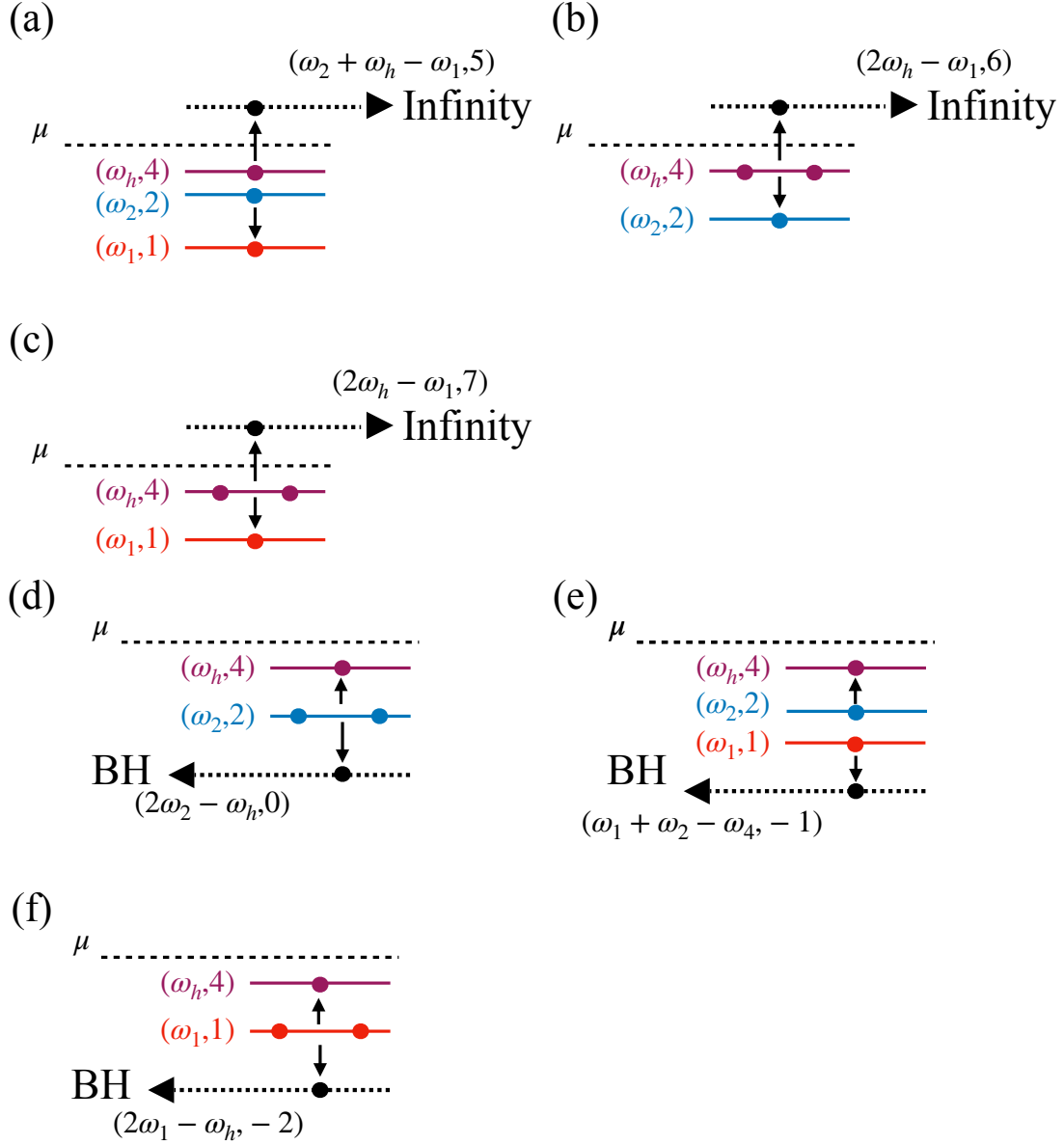
Figure 5.12: Relevant processes involving the $l = m = 1$, the $l = m = 2$ and the $l = m = 4$ fundamental modes. In this figure, the subscript h stands for the $l = m = 4$ fundamental mode. The top two diagrams ((a) and (b)) describe the processes in which the energy of the excited unbounded modes are dissipated to infinity, and the bottom three ((c), (d), and (e)) describe the ones in which the excited modes are absorbed by the horizon.
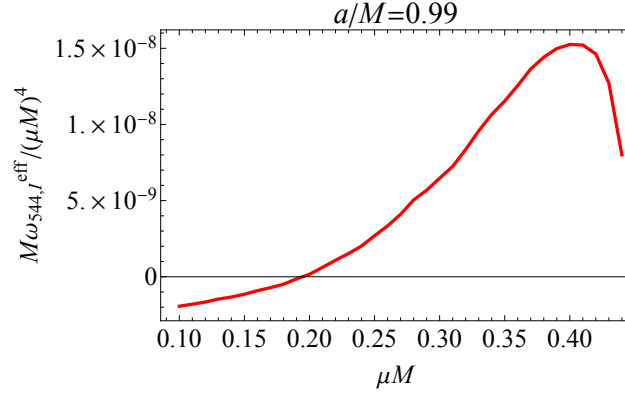
Figure 5.13: Same figure as the left panel of Fig. 5.5, but with $\omega_{544,I}^{\text{eff}}$.
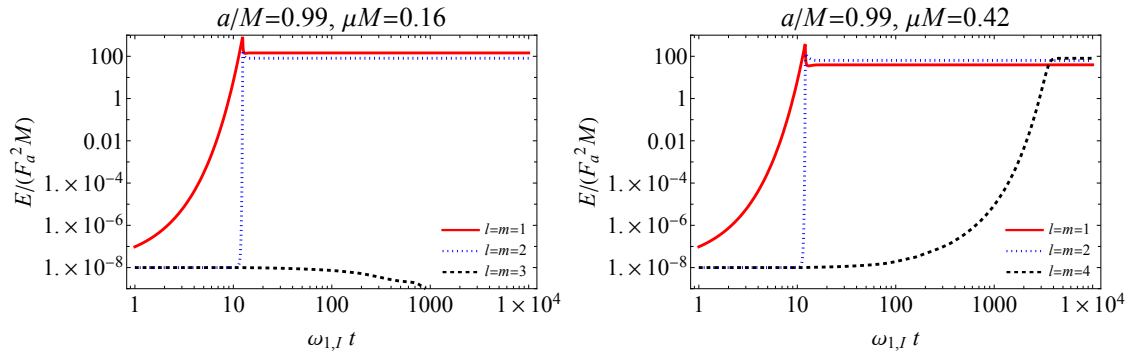
Figure 5.14: The same figures as Fig. 5.3, but with the fundamental $l = m = 4$ mode as the third mode, instead of $l = m = 1$ overtones. The left and right panels correspond to the case with $\mu M = 0.16$ and 0.42, respectively.

Chapter 6

Primary cloud composed of a higher multipole mode

So far, we have focused on the axion condensate dominated by the $l = m = 1$ fundamental mode. This is the case when axion mass is in the range $\mu M \lesssim 0.45$ (see Fig. 2.2). In this chapter, we discuss the case with the condensate starting with the $l = m = 2$ fundamental mode, which corresponds to the parameter range, $0.45 \lesssim \mu M \lesssim 0.92$. All of our formulations can be straightforwardly applied to current case by setting $(l_1, m_1) = (2, 2)$.

In parallel with the case with the dominance of the $l = m = 1$ fundamental mode, we choose the secondary cloud to be the next higher multipole mode, i.e., $(l_2, m_2) = (3, 3)$. The relevant process is shown in Fig. 6.1. Whether or not process (b) in Fig. 6.1 contributes to the energy dissipation depends on the axion mass μ. This is because the binding energies of different modes depend on μ in a slightly complicated manner. As a reference, let us consider the well-known energy levels in the non-relativistic approximation ($\mu M \ll 1$). Then, the real part of the axion cloud frequency is approximated by Eq. (2.24), which gives

$$\omega_1|_{l_1 = m_1 = 2} \sim \mu \left(1 - \frac{(\mu M)^2}{2 \times 3^2} \right) \ , \tag{6.1}$$

$$\omega_2|_{l_1 = m_1 = 3} \sim \mu \left(1 - \frac{(\mu M)^2}{2 \times 4^2} \right) \ . \tag{6.2}$$

The frequency of the mode excited by process (b) in Fig. 6.1 is given by

$$2\omega_2 - \omega_1 \sim \mu - \mu \frac{(\mu M)^2}{144} < \mu \ . \tag{6.3}$$

Therefore, this mode is bounded by the gravitational potential and cannot carry the energy to infinity. In addition, the mode is superradiant and thus contributes to the dissipation of the $l = m = 2$ mode. In Fig. 6.2, we show the frequency of the excited mode obtained by the numerical calculation. We observe that the excited mode is bounded for $\mu M \lesssim 0.8$. Therefore, saturation of superradiance cannot be expected for an axion mass in this range, and the $l = m = 3$ cloud keeps growing. The interesting point is that the growth of the $l = m = 3$ cloud is accelerated by the presence of the $l = m = 2$ cloud.

On the other hand, for $\mu M \gtrsim 0.8$ everything is parallel to the case of the $l_1 = m_1 = 1$ mode dominance. The condensate settles into a quasi-stationary configuration composed
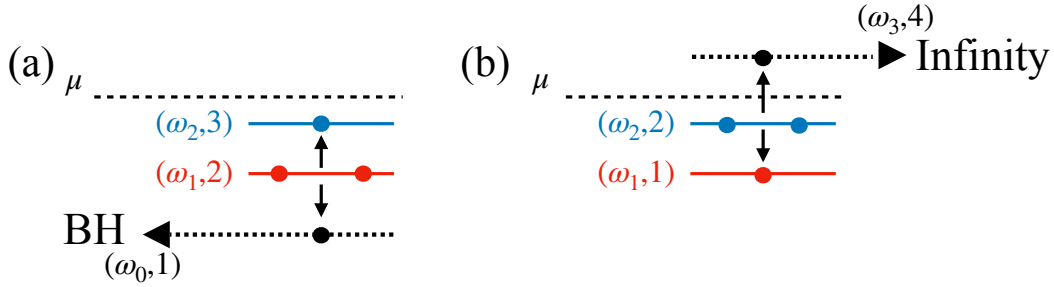
Figure 6.1: The interaction between the $l = m = 2$ and the $l = m = 3$ clouds when the primary cloud is the $l = m = 2$ mode. In this figure, $\omega_1 = \omega^{(322)}$ and $\omega_2 = \omega^{(433)}$. The frequencies ω_0 and ω_3 is defined as $\omega_0 \equiv 2\omega_1 - \omega_2$ and $\omega_3 \equiv 2\omega_2 - \omega_1$.
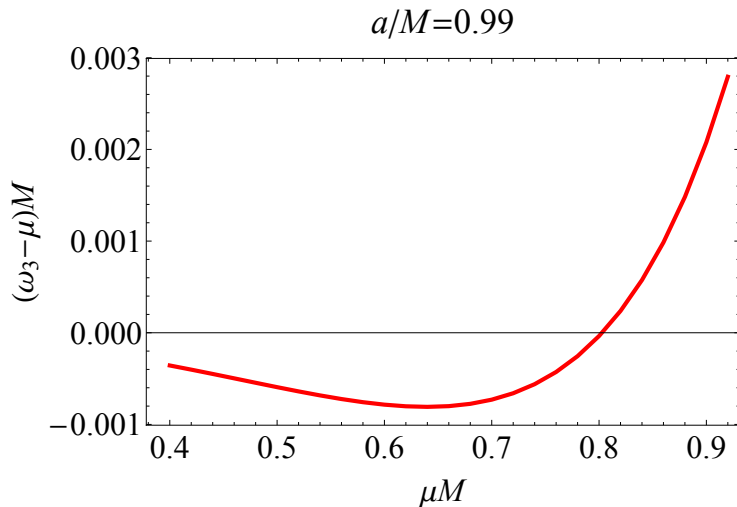

Figure 6.2: The frequency of the excited mode presented in the right diagram (b) of Fig. 6.1.

of the $l_1 = m_1 = 2$ and $l_2 = m_2 = 3$ clouds. In Fig. 6.3, we show examples of the time evolution, setting $\mu M = 0.6$ and $\mu M = 0.88$ with $a/M = 0.99$.

The qualitative picture presented above does not change even if we include the $l = m = 4$ mode (see Fig. 6.3). In fact, the $l = m = 4$ mode cannot be excited. This is because the processes producing the $l = m = 4$ fundamental mode are smaller than the processes dissipating the $l = m = 4$ mode. The situation is similar to the decay of the $l = m = 2$ overtones for condensate starting with the $l = m = 1$ fundamental mode (see Sec. 5.2).

In summary, the condensate starting from the dominance of a higher multipole mode with $l \geq 2$ would terminate the growth due to the superradiant instability only when the axion mass marginally satisfies the superradiance condition. In the case of initial $l = m = 2$ dominance, only when the axion mass falls in the range, $0.8 \lesssim \mu M \lesssim 0.92$, the superradiant instability is regulated by dissipation. For the case $\mu M \lesssim 0.8$, the $l = m = 3$ fundamental mode will grow to a large amplitude. In this case, explosive phenomena such as bosenova can occur. In principle, whether bosenova happens or not can be studied by the method in Sec. 4.1 by taking $l_1 = m_1 = 3$ there. However, we need to determine the imaginary part of the frequency, which is much smaller than the case for the $l = m = 1$ or $l = m = 2$ (see Fig. 2.2). Therefore, the calculation with the $l = m = 3$ mode requires
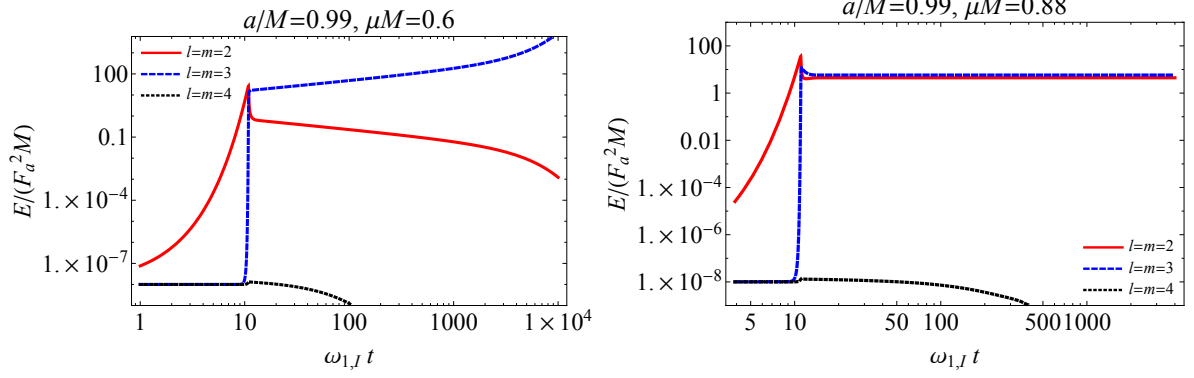
Figure 6.3: Time evolution of energy of the modes $l = m = 2$, $l = m = 3$, and $l = m = 4$ when the primary cloud is composed of the $l = m = 2$ mode. The red solid, blue dashed, and black dotted lines correspond to the fundamental mode of $l = m = 2$, $l = m = 3$, and $l = m = 4$, respectively. The left and the right panels show the cases with $\mu M = 0.6$ and 0.88, respectively. We set the BH spin to $a/M = 0.99$.

a high computational cost. For this reason, we leave the investigation of the $l = m = 3$ mode in the large amplitude regime to future works.

Chapter 7

Summary and Discussion

In this thesis, we studied the evolution of the self-interacting axion condensate around rotating black holes, targeting the detection of the axion by future gravitational wave observations. In particular, we focused on tracking the whole evolution of the condensate, starting with a small amplitude, such as quantum fluctuation, to a large amplitude where the nonlinear effect by the self-interaction is not negligible. For this purpose, we formulated the perturbative method (chapter 3) and nonlinear numerical method (chapter 4) to track the evolution in the two mode approximation. Our formalism is capable of tracking the evolution for any value of the gravitational coupling μM.

Using our method, we extensively studied the case with a condensate starting from the dominance of the $l = m = 1$ fundamental mode, corresponding to a gravitational coupling in the range $\mu M \lesssim 0.45$. With the perturbative RG method, we revealed that an acceleration of instability by the self-interaction is the first effect that influences the evolution (chapter 3). In addition, we showed that the condensate inevitably enters the nonlinear regime where perturbation theory cannot be trusted. Then using the nonlinear numerical method, we clarified the condition of bosenova occurrence with neglecting clouds other than the $l = m = 1$ fundamental mode (Sec. 4.1). For this case, the bosenova can occur only for $\mu M \lesssim 0.32$ and when the energy of the $l = m = 1$ cloud reaches

$$E_1 \sim 3 \times 10^2 (\mu M)^{-2} F_a^2 M \ . \tag{7.1}$$

For the gravitational coupling in the range $0.32 \lesssim \mu M \lesssim 0.45$, the gravitational potential is deep enough to prevent the occurrence of the bosenova. In this case, the condensate settles into a quasi-stationary configuration, and the radial profile becomes much more compact than the original configuration because of the attractive self-interaction (see Fig. 4.2).

Then, we studied whether the inclusion of the secondary $l = m = 2$ mode can change the above picture (Sec. 4.2). In this case, the dissipation due to the interaction between the $l = m = 1$ and $l = m = 2$ fundamental modes is sufficiently strong to overcome the superradiant growth much before the primary cloud approaches the critical energy (7.1). In particular, since the self-interaction is attractive for a typical cosine-type potential, the different modes attract each other, leading to the significant enhancement of energy dissipation due to the mode-mode interaction. Thus, even if the secondary $l = m = 2$ cloud begins to grow from the tiny amplitude expected by quantum fluctuations, the dissipation will inevitably become strong and the primary cloud will stop growing. As a result, the condensate settles to a quasi-stationary configuration, determined by the balance between the energy gain by the superradiance and the energy dissipation by the

interaction between the modes. Interestingly, the saturation occurs in the small amplitude regime where the self-interaction can be treated perturbatively.

We further investigated whether the quasi-stationary state is stable under the influence of other self-interaction effects (chapter 5). For example, there could be dissipation due to processes involving modes other than the two fundamental modes or quantum mechanical processes. However, these processes are much slower than the classical processes between the $l = m = 1$ and $l = m = 2$ fundamental modes and in many cases do not significantly alter the quasi-stationary state composed of these two modes. As a result, the final cloud configuration consists mainly of $l = m = 1$ and $l = m = 2$ fundamental modes, accompanied by $l = m = 1$ overtones with subdominant amplitude. The $l = m = 2$ overtones do not grow due to dissipation by interaction.

The higher multipole modes with $l = m = 3$ and $l = m = 4$ can grow when the axion mass satisfies $0.12 \lesssim \mu M \lesssim 0.24$ and $0.2 \lesssim \mu$, respectively. In these exceptional cases, the $l = m = 3$ and/or the $l = m = 4$ fundamental mode could be the dominant mode, and further interactions involving the $l = m = 3$ and the $l = m = 4$ mode could significantly change the configuration. In this case, calculations beyond the 3-state approximation employed in this thesis would be required. However, the number of possible processes due to the interaction between the modes becomes tediously large. For this technical reason, we leave the investigation for the future.

We also studied the case in the case in which the $l = m = 2$ fundamental mode is dominant in the initial stage of the evolution. This corresponds to the axion mass in the range $0.45 \lesssim \mu M \lesssim 0.92$. In this case, the evolution of the condensate depends qualitatively on the axion mass. When the axion mass is smaller than 0.8, a quasi-stationary state cannot be achieved, unlike the case starting from the $l = m = 1$ fundamental mode. This is because the dissipative processes at work in the $l = m = 1$ case are prohibited owing to the change in the size of the energy level differences. In this case, the $l = m = 3$ mode grows to have a very large amplitude, requiring nonlinear calculations to track the evolution. Unfortunately, due to the high computational cost, we could not present results for this case and leave it for future studies.

On the other hand, when the mass is larger than 0.8, the shift of the energy spectrum due to the relativistic effect is sufficiently large to open the dissipation channel, which was absent for $\mu M \lesssim 0.8$. In this case, the final state is a superposition of clouds consisting of the $l = m = 2$ and $l = m = 3$ fundamental modes. We summarized our results in Tab. 7.1.

We should mention that the calculations in Chapters 5 and 6 are done with the spin of the central black hole fixed to $a/M = 0.99$. One concern is the possibility that the spin of the central black hole may affect the result. However, we expect that our results are robust under the change of the BH spin since we showed that nonlinear calculation in Sec. 4.1 black hole spin only has a small effect on the evolution of the self-interacting cloud, except for the presence of the superradiant instability and its rate. However, as we will discuss below, a detailed analysis of the dependence on the BH spin is necessary for the actual application to observations.

Finally, we discuss the future directions of our study. In this thesis, we treated the axion as a test field and fixed the background to the Kerr spacetime. Our treatment misses two important effects for future observations: the gravitational wave emission by the condensate and the spin-down of the central black hole. Quantitative studies on these effects are needed. In the followings, we briefly comment on them.

First, we discuss gravitational wave emissions from the condensate. As we showed in

Table 7.1: Summary of our results classified by the size of the gravitational coupling. The first two low corresponds to the single mode calculation in Sec. 4.1. Others correspond to the case when the excitation of the several modes is considered. Note that in the overlapping region $0.2 \lesssim \mu M \lesssim 0.24$, our analysis is not enough to conclude the dominant modes in the quasi-stationary configuration.

The range of gravitational coupling μM	occurrence of bosenova	Example of time evolution
$\mu M \lesssim 0.32$	bosenova	need dynamical simulation
$\mu M \gtrsim 0.32$	no bosenova	Fig. 4.4
The range of gravitational coupling μM	Dominant modes (n, l, m) in the quasi-stationary configuration	Example of time evolution
$\mu M \lesssim 0.12$	Dominant:$(2, 1, 1) + (3, 2, 2)$ Subdominant:$(n, 1, 1), n \leq 5$	Fig. 5.3
$0.12 \lesssim \mu M \lesssim 0.24$	$(2, 1, 1) + (3, 2, 2) + (4, 3, 3)$	Fig. 5.10(left panel)
$0.2 \lesssim \mu M \lesssim 0.45$	$(2, 1, 1) + (3, 2, 2) + (5, 4, 4)$	Fig. 5.14 (right panel)
$0.45 \lesssim \mu M \lesssim 0.8$	$(4, 3, 3)$	Fig. 6.3(left panel)
$0.8 \lesssim \mu M \lesssim 0.92$	$(3, 2, 2) + (4, 3, 3)$	Fig. 6.3(right panel)

this thesis, the axion condensate reaches the quasi-stationary state with several modes simultaneously excited. Then we expect two types of gravitational wave emission processes: the pair annihilation and the level transition. These processes emit gravitational waves in the different frequency bands (see Sec. 2.3). Simultaneous detection of these gravitational waves can be strong evidence for the axion. We would like to mention that the strain amplitude of the gravitational waves should be proportional to the square of the axion decay constant F_a^2, since the energy of the configuration we obtained scales as $F_a^2 M$. Therefore, from the detection of the continuous gravitational waves, we can also extract information on the decay constant. Numerical calculations are necessary to precisely estimate the amplitudes and the frequencies of the emitted gravitational waves, and we leave them for future work.

Next, we discuss the black hole spin-down. Owing to the adiabatic nature of the evolution, we can describe the change of the BH spin as

$$\frac{dJ_{BH}}{dt} = -\frac{2m_1\omega_{1,I}}{\omega_{1,R}}E_1 - \frac{2m_2\omega_{2,I}}{\omega_{2,R}}E_2 \sim -\frac{2m_1\omega_{1,I}}{\omega_{1,R}}E_1 \ . \tag{7.2}$$

Then, we can estimate the spin-down timescale τ_{spin} as

$$\tau_{\text{spin}}^{-1} = \frac{1}{J_{BH}}\frac{dJ_{BH}}{dt} \sim 2m_1\omega_{1,I}\frac{E_1^{\text{qs}}}{aM} \sim 10^2 m_1\omega_{1,I}F_a{}^2 \ . \tag{7.3}$$

Here, we take $E_1^{\text{qs}} \sim 10^2 F_a^2 M$ from our numerical calculation. We have $\tau_{\text{spin}} \sim 10^4 \omega_{1,I}^{-1}$ for the string axion ($F_a \sim 10^{-3}$). This is sufficiently long compared to the instability timescale, indicating that the condensate first settles to the quasi-stationary state presented in this paper.

However, we need to carefully examine the effect of the black hole spin-down to discuss the actual observability of gravitational waves. Note that the quasi-stationary state is supported by the superradiant instability. Thus, as a black hole spin down, the instability rate becomes smaller and the overall amplitude of the condensate decreases. As a result,

the amplitudes of gravitational waves gradually drop as the condensate extracts the spin of the black hole. We should also mention that the evolution of the whole system can be altered once multiple modes are excited [64]. We also leave the issues related to the spin-down for future work.

Acknowledgement

Appendix A

Kerr space-time

In this appendix, we show formulas of the Kerr space-time [65] used in the thesis. The metric of the Kerr space-time in the Boyer-Lindquist coordinates is given by

$$ds^2 = -\left(1 - \frac{2Mr}{\rho^2}\right) dt^2 - \frac{4aMr\sin^2\theta}{\rho^2} dtd\varphi$$
$$+ \left[(r^2 + a^2) + \frac{2Mr}{\rho^2} a^2 \sin^2\theta\right] \sin^2\theta d\varphi^2 + \frac{\rho^2}{\Delta} dr^2 + \rho^2 d\theta^2 ,$$

(A.1)

where

$$\Delta = r^2 - 2Mr + a^2 , \qquad\qquad \rho^2 = r^2 + a^2 \cos^2\theta .$$

(A.2)

The two roots of $\Delta = 0$, which are

$$r_\pm = M \pm \sqrt{M^2 - a^2} ,$$

(A.3)

correspond to the position of the event horizon ($r = r_+$) and the Cauchy horizon ($r = r_-$). When we consider the behavior of the fields around the event horizon, tortoise coordinates r_* defined by

$$dr_* = \frac{(r^2 + a^2)}{\Delta} dr ,$$

(A.4)

is more convenient than r. Integration of Eq. (A.4) gives

$$r_* = r + \frac{2M}{r_+ - r_-} \left(r_+ \log\frac{r - r_+}{r_+} - r_- \log\frac{r - r_-}{r_-}\right) .$$

(A.5)

The volume form and the inverse of the metric are given by

$$\sqrt{-g} = \rho^2 \sin^2\theta ,$$

(A.6)

$$g^{\mu\nu}\partial_\mu\partial_\nu = -\frac{1}{\Delta}\left[(r^2 + a^2) + \frac{2Mr}{\rho^2} a^2 \sin^2\theta\right] \partial_t^2 - \frac{4aMr}{\rho^2\Delta}\partial_t\partial_\varphi$$
$$+ \frac{1}{\Delta\sin^2\theta}\left(1 - \frac{2Mr}{\rho^2}\right)\partial_\varphi^2 + \frac{\Delta}{\rho^2}\partial_r^2 + \frac{1}{\rho^2}\partial_\theta^2 .$$

(A.7)

The d'Alembertian takes the form

$$\Box_g = \frac{1}{\rho^2}\left[\frac{\partial}{\partial r}\left(\Delta\frac{\partial}{\partial r}\right) + \frac{1}{\sin\theta}\frac{\partial}{\partial\theta}\left(\sin\theta\frac{\partial}{\partial\theta}\right) - \frac{4Mar}{\Delta}\frac{\partial^2}{\partial t\partial\varphi}\right.$$
$$\left. - \left[\frac{(r^2 + a^2)^2}{\Delta} - a^2\sin^2\theta\right]\frac{\partial^2}{\partial t^2} + \frac{1}{\sin^2\theta}\left(1 - \frac{a^2\sin^2\theta}{\Delta}\right)\frac{\partial^2}{\partial\varphi^2}\right] .$$

(A.8)

Another important property of the Kerr space-time is that it is stationary and axisymmetric. Therefore, there exist two killing vectors ξ_t and ξ_φ. In the Boyer-Lindquist coordinates, they are $\xi_t = (1, 0, 0, 0)$ and $\xi_\varphi = (0, 0, 0, 1)$.

Another coordinate system used in the thesis is the ingoing Kerr coordinates $(\tilde{t}, r, \theta, \tilde{\varphi})$. The metric in the ingoing Kerr coordinates takes the following form,

$$ds^2 = -\left(1 - \frac{2Mr}{\rho^2}\right) d\tilde{t}^2 + 2dr d\tilde{t} - 2a \sin^2\theta dr d\tilde{\varphi} + \rho^2 d\theta^2$$
$$- \frac{4Mar}{\rho^2} \sin^2\theta d\tilde{\varphi} d\tilde{t} + \frac{1}{\rho^2} \left[(r^2 + a^2)^2 - \Delta a^2 \sin^2\theta\right] \sin^2\theta d\tilde{\varphi}^2 . \qquad \text{(A.9)}$$

The transformation of the Boyer-Lindquist coordinates to the ingoing Kerr coordinates is given by

$$d\tilde{t} = dt + \frac{r^2 + a^2}{\Delta} dr , \qquad\qquad d\tilde{\varphi} = d\varphi + \frac{a}{\Delta} dr . \qquad \text{(A.10)}$$

Note that in the ingoing Kerr coordinate, ingoing null geodesics pass through the event horizon in a finite coordinate time $\tilde{t}$. In addition, they become a straight line $dr = d\tilde{t}$.

Appendix B

Numerical construction of the mode functions

In this appendix, we show the numerical methods to accurately solve the angular and the radial equations

$$\frac{\mathrm{d}}{\mathrm{d}x}\left((1-x^2)\frac{\mathrm{d}S_{lm\omega}}{\mathrm{d}x}\right) + [c^2(\omega)x^2 - \frac{m^2}{1-x^2}]S_{lm\omega} = -\Lambda_{lm}(\omega)S_{lm\omega} \ , \qquad (\text{B.1})$$

$$\frac{\mathrm{d}}{\mathrm{d}r}\left(\Delta\frac{\mathrm{d}R_{lm\omega}}{\mathrm{d}r}\right) + \left[\frac{K^2(\omega)}{\Delta} - \mu^2 r^2 - \lambda_{lm}(\omega)\right]R_{lm\omega} = 0 \ , \qquad (\text{B.2})$$

with

$$c^2(\omega) = a^2(\omega^2 - \mu^2) \ , \qquad\qquad K(\omega) = (r^2 + a^2)\omega - am \ ,$$
$$\lambda_{lm}(\omega) = -2am\omega + a^2\omega^2 + \Lambda_{lm}(\omega) \ , \qquad\qquad x = \cos\theta \ . \qquad (\text{B.3})$$

We set $GM = 1$ in this appendix for notational simplicity. The mode functions used in this thesis are constructed by the method presented here.

It is known that Eqs. (B.1) and (B.2) can be transformed to the generalized spheroidal wave equation [66]

$$z(z - z_0)\frac{d^2y}{dz^2} + (B_1 + B_2 z)\frac{dy}{dz} + \left(\tilde{\omega}^2 z(z - z_0) - 2\eta\tilde{\omega}(z - z_0) + B_3\right)y = 0 \ , \qquad (\text{B.4})$$

or the confluent Heun equation[1] [67, 68]

$$z(z - 1)\frac{d^2y}{dz^2} + (\gamma(z - 1) + \delta z + \epsilon z(z - 1))\frac{dy}{dz} + (\alpha z - q)y = 0 \ . \qquad (\text{B.5})$$

A general property of these equations is that they have two regular singular points and one irregular singular point. It is worth mentioning that the solution to the Confluent Heun equation with a regular behavior around regular singular point is implemented in the MATHEMATICA as HeunC$[q, \alpha, \gamma, \delta, \epsilon, z]$. In the following, we transform Eqs. (B.1) and (B.2) to the generalized spheroidal wave equation or the confluent Heun equation and solve them.

---

[1]The confluent Heun equation and the generalized spheroidal wave equation is related by replacing y in the generalized spheroidal wave equation by $e^{i\omega z}y$ and rescaling z by z_0.

B.1 Angular equation

We start with solving the angular equation (B.1). The boundary conditions are the regularity at $x = \pm 1$. Let us transform the angular function as

$$S_{lm\omega}(x) = (1+x)^{k_1}(1-x)^{k_2}e^{c(1+x)}g(x) \; . \tag{B.6}$$

Then Eq. (B.1) transforms to

$$(1+x)(1-x)\frac{\mathrm{d}^2 g}{\mathrm{d}x^2} + \left(2c(1-x^2) - 2(k_1+k_2+1)x + 2(k_1-k_2)\right)\frac{\mathrm{d}g}{\mathrm{d}x}$$
$$+ \left(\frac{2k_1^2}{1+x} + \frac{2k_2^2}{1-x} - 2c(k_1+k_2+1)x + c^2 + 2c(k_1-k_2)\right.$$
$$\left. -(k_1+k_2)(k_1+k_2+1) - \frac{m^2}{1-x^2} + \Lambda_{lm}\right)g = 0 \; . \tag{B.7}$$

To obtain the solution regular around $x = \pm 1$, we chose $k_{1,2} = |m|/2$. Now, we transform the variable x to $u = x + 1$. Then Eq. (B.7) recast to

$$u(u-2)\frac{\mathrm{d}^2 g}{\mathrm{d}u^2} + 2\left(cu(u-2) + (|m|+1)u + |m|+1\right)\frac{\mathrm{d}g}{\mathrm{d}u}$$
$$+ \left(2c(|m|+1)u - c^2 - 2c(|m|+1) + |m|(|m|+1) - \Lambda_{lm}\right)g = 0 \; . \tag{B.8}$$

Since g is regular around $u = 0$, we expand g as

$$g(u) = \sum_{n=0}^{\infty} a_n u^n \; , \tag{B.9}$$

with $a_0 = 1$. Substituting Eq. (B.9) to Eq. (B.8), we obtain the three term recurrence relation

$$\alpha_{\theta,n}a_{n+1} + \beta_{\theta,n}a_n + \gamma_{\theta,n}a_{n-1} = 0 \; , \qquad (n = 0, 1, \cdots) \; , \tag{B.10}$$

with $a_{-1} = 0$. Here, the coefficients $\alpha_{\theta,n}, \beta_{\theta,n}$, and $\gamma_{\theta,n}$ are given by

$$\alpha_{\theta,n} = -2(n+1)(n+|m|+1) \; , \tag{B.11}$$
$$\beta_{\theta,n} = n(n-1) + 2n(|m|+1-2c) + |m|(|m|+1) - 2c(|m|+1) - c^2 - \Lambda_{lm} \; , \tag{B.12}$$
$$\gamma_{\theta,n} = 2c(n+|m|) \; . \tag{B.13}$$

The solution (B.9) is guaranteed to be regular at $u = 0$ ($x = -1$). The regularity at $x = 1$ holds only if the summation converges uniformly on $0 \le u \le 2$. The condition for the uniform convergence is

$$\lim_{n\to\infty}\left|\frac{a_{n+1}u^{n+1}}{a_n u^n}\right| < 1 \; . \tag{B.14}$$

for any $0 \le u \le 2$. The asymptotic relation among the ratios $R_n = a_{n+1}/a_n$ is obtained by keeping leading terms in n in Eq. (B.10) as

$$-2n^2 R_n + n^2 + 2cn\frac{1}{R_{n-1}} \sim 0 \; . \tag{B.15}$$

Thus, assuming $R_n \sim R_{n-1}$, the asymptotic form of R_n is

$$R_n \sim \frac{1}{2} \, , \tag{B.16}$$

or

$$R_n \sim -\frac{2c}{n} \, . \tag{B.17}$$

The sequence with the behavior (B.16) as $n \to \infty$ is called dominant. The case with (B.17) is called minimal. [2] The minimal sequence is the one that leads to uniform convergence. The existence of the minimal sequence is possible if and only if the expression for R_0 written by means of continued fraction

$$R_0 = -\frac{\gamma_{\theta,1}}{\beta_{\theta,1}-} \frac{\alpha_{\theta,1}\gamma_{\theta,2}}{\beta_{\theta,2}-} \cdots \equiv -\frac{\gamma_{\theta,n}}{\beta_{\theta,n} - \dfrac{\alpha_{\theta,n}\gamma_{\theta,n+1}}{\beta_{\theta,n+1} - \dfrac{\alpha_{\theta,n+1}\gamma_{\theta,n+2}}{\ddots}}} \, , \tag{B.18}$$

is consistent (see [69] for the proof). It is also shown that the relation

$$R_{n-1} = -\frac{\gamma_{\theta,n}}{\beta_{\theta,n}-} \frac{\alpha_{\theta,n}\gamma_{\theta,n+1}}{\beta_{\theta,n+1}-} \cdots \, , \tag{B.19}$$

holds for the minimal sequence.

The convergence of the continued fraction occurs only for special values of Λ_{lm}. The sufficient condition for the convergence is when Λ_{lm} satisfies the equation

$$-\frac{\beta_{\theta,0}}{\alpha_{\theta,0}} = R_0 = -\frac{\gamma_{\theta,1}}{\beta_{\theta,1}-} \frac{\alpha_{\theta,1}\gamma_{\theta,2}}{\beta_{\theta,2}-} \cdots \, . \tag{B.20}$$

Solving this equation determines the eigenvalue Λ_{lm}. In this thesis, we construct the right-hand side of Eq. (B.20) using the recursion relation

$$R_n = -\frac{\gamma_{\theta,n}}{\beta_{\theta,n} + \alpha_n R_{n+1}} \, . \tag{B.21}$$

At a large enough $n = N_{\max}$ (say 600), we set $R_{N_{\max}} = -2c/N_{\max}$, assuming the convergence to the asymptotic form, and use this relation recursively until we reach R_0. [3] After obtaining the correct value for Λ_{lm}, we solve three-term recurrence relation (B.10) from $a_{-1} = 0, a_0 = 1$ to large enough n to construct the angular mode function. If $l \neq |m|$, solving inversion of Eq. (B.20) at $\tilde{n} = l - |m|$ [71],

$$-\frac{\beta_{\theta,\tilde{n}}}{\alpha_{\theta,\tilde{n}}} + \frac{\gamma_{\theta,\tilde{n}}}{\alpha_{\theta,\tilde{n}}} \frac{\alpha_{\theta,\tilde{n}-1}}{\beta_{\theta,\tilde{n}-1}-} \frac{\alpha_{\theta,\tilde{n}-2}\gamma_{\theta,\tilde{n}-1}}{\beta_{\theta,\tilde{n}-2}-} \cdots \frac{\alpha_{\theta,0}\gamma_{\theta,1}}{\beta_{\theta,0}-} = -\frac{\gamma_{\theta,\tilde{n}+1}}{\beta_{\theta,\tilde{n}+1}-} \frac{\alpha_{\theta,\tilde{n}+1}\gamma_{\theta,\tilde{n}+2}}{\beta_{\theta,\tilde{n}+2}-} \cdots \, , \tag{B.22}$$

---

[2]More precise definition of the dominat and the minimal sequence of three-term recurrence relations is followings [69, 66]. Consider the two independent solutions of any three-term recurrence relation, A_n and B_n. The sequence A_n is called minimal if

$$\lim_{n \to \infty} \frac{A_n}{B_n} = 0 \, .$$

Any non-minimal solution is called dominant.

[3]Another method to construct the continued fraction is *Steed's algorithm* [70]. This algorithm does not require knowledge of the asymptotic form of the sequence.

is numerically more stable. For example, Eq. (B.20) cannot give a correct answer $\Lambda_{lm} \sim l(l+1)$ in the small c limit if $l \neq |m|$. Solving Eq. (B.20) with $c \to 0$ gives $\Lambda_{lm} \sim |m|(|m|+1)$, regardless of a value of l. On the other hand, the inversion at $l - |m|$ (B.22) gives $\Lambda_{lm} \sim l(l+1)$.

Another way to obtain the angular mode function is to use the confluent Heun function implemented in the program, such as MATHEMATICA. Rescaling u in Eq. (B.8) to $u/2$, one obtain the confluent Heun equation with

$$
q = 2c(1+|m|) + c^2 - |m|(|m|+1) + \Lambda_{lm} \ , \quad \alpha = 4c(1+|m|) \ , \quad \gamma = 1 + |m| \ ,
$$

$$
\delta = 1 + |m| \ , \qquad\qquad\qquad\qquad \epsilon = 4c \ , \qquad z = \frac{1+x}{2} \ . \qquad \text{(B.23)}
$$

Thus, the solution guaranteed to be regular at $x = -1$ is given by

$$
S_{lm\omega}^{x=-1} = (1+x)^{|m|/2}(1-x)^{|m|/2}e^{c(1+x)}\text{HeunC}\left[2c(1+|m|)+c^2-|m|(|m|+1)+\Lambda_{lm},\right.
$$

$$
\left. 4c(1+|m|), 1+|m|, 1+|m|, 4c, \frac{1+x}{2}\right] \ .
$$

$$
\text{(B.24)}
$$

Note that this solution is not generally regular at $x = +1$. Similarly, we can perform the same procedure with $z = (1-x)/2$. For this case, we obtained the solution guaranteed to be regular at $x = +1$ as

$$
S_{lm\omega}^{x=+1} = (1+x)^{|m|/2}(1-x)^{|m|/2}e^{c(1-x)}\text{HeunC}\left[2c(1+|m|)+c^2-|m|(|m|+1)+\Lambda_{lm},\right.
$$

$$
\left. 4c(1+|m|), 1+|m|, 1+|m|, 4c, \frac{1-x}{2}\right] \ .
$$

$$
\text{(B.25)}
$$

Again, the solution is not generally regular at $x = -1$. The solution become regular both at $x = \pm$ when two solutions $S_{lm\omega}^{\pm 1}$ is proportional. In other words, Wronskian of two solutions $S_{lm\omega}^{\pm 1}$ is zero

$$
(1-x^2)\left(S_{lm\omega}^{+1}\partial_x S_{lm\omega}^{-1} - S_{lm\omega}^{-1}\partial_x S_{lm\omega}^{+1}\right) = 0 \ . \qquad \text{(B.26)}
$$

Solving (B.26) for Λ_{lm}, we obtain the eigenvalue Λ_{lm} and the eigenfunction $S_{lm\omega}$.

B.2 Radial equation

Now, we solve the radial equation (B.2). First, we transform the radial mode function as

$$
R_{lm\omega} = (r - r_+)^{k_+}(r - r_-)^{k_-}y(r) \ . \qquad \text{(B.27)}
$$

Similarly to the calculation in App. B.1, the function y obeys

$$
(r-r_+)(r-r_-)\frac{d^2 y}{dr^2} + ((2k_+ + 1)(r-r_-) + (2k_- + 1)(r-r_+))\frac{dy}{dr}
$$

$$
+ \left[k_+^2 \frac{r_+ - r_-}{r - r_+} + k_-^2 \frac{r_- - r_+}{r - r_-} + (k_+ + k_-)(k_+ + k_- + 1)\right.
$$

$$
\left. + \frac{K^2}{\Delta} - \mu^2 r^2 - \lambda_{lm}\right]y = 0 \ . \qquad \text{(B.28)}
$$

The behavior of the quantities inside $[\cdots]$ in Eq. (B.28) near the regular singular points $r = r_\pm$ is given by[4]

$$\left[k_+^2 \frac{r_+ - r_-}{r - r_+} + k_-^2 \frac{r_- - r_+}{r - r_-} + (k_+ + k_-)(k_+ + k_- + 1) + \frac{K^2}{\Delta} - \mu^2 r^2 - \lambda_{lm} \right]$$

$$\longrightarrow \begin{cases} \dfrac{1}{r - r_+} \left(\pm 2b k_+^2 \pm \dfrac{(2r_+ \omega - am)^2}{2b} \right) , & (r \to r_+) , \\[3mm] \dfrac{1}{r - r_-} \left(\pm 2b k_-^2 \pm \dfrac{(2r_- \omega - am)^2}{2b} \right) , & (r \to r_-) , \end{cases} \tag{B.29}$$

where we defined $2b = r_+ - r_-$. To eliminate the singular behavior in the Eq. (B.28), we choose $k_\pm$ to be

$$k_+ = \pm i \frac{2r_+ \omega - am}{2b} , \qquad\qquad k_- = \pm i \frac{2r_- \omega - am}{2b} . \tag{B.30}$$

The choice of $k_\pm$ determines the behavior of the mode functions at the event horizon and the Cauchy horizon. For example, near the event horizon, $(r - r_+)^{k_+}$ behave as

$$(r - r_+)^{k_+} \sim \exp\left(\pm i(\omega - m\Omega_H) r_* \right) , \tag{B.31}$$

where we used the fact $r_* \sim r_+/b \log(r - r_+)$ if $r \sim r_+$. Clearly, $+$ sign corresponds to the outgoing wave and $-$ sign corresponds to the ingoing wave near the event horizon, for $\omega > m\Omega_H$. Actually, this is true even when the wave satisfies the superradiance condition $\omega < m\Omega_H$ (see Appendix B of [72] for a detailed explanation).

B.2.1   Unstable mode

First, we solve Eq. (B.2) with an ingoing boundary condition at the event horizon and exponentially decaying boundary condition at the infinity. This boundary condition corresponds to the superradiant unstable mode in Sec. 2.2. Regarding the boundary condition, we take $k_\pm$ to be

$$k_+ = -i \frac{2r_+ \omega - am}{2b} , \qquad\qquad k_- = +i \frac{2r_- \omega - am}{2b} . \tag{B.32}$$

After changing variable to $z = r - r_-$, Eq. (B.28) takes the form

$$z(z - 2b) \frac{d^2 y}{dz^2} + \left(-2b(2k_- + 1) + 2(k_+ + k_- + 1)z \right) \frac{dy}{dz}$$
$$+ \left((\omega^2 - \mu^2)z(z - 2b) - 2(\mu^2 - 2\omega^2)(z - 2b) + (k_+ + k_-)(k_+ + k_- + 1) \right.$$
$$\left. + 4\omega^2(2 + b) - 2\mu^2(1 + b) - a^2(\omega^2 - \mu^2) - \Lambda_{lm} \right) y = 0 , \tag{B.33}$$

which is the generalized spheroidal wave equation with

$$z_0 = 2b , \qquad\qquad \tilde{\omega} = \sqrt{\omega^2 - \mu^2} ,$$
$$\eta = \frac{(\mu^2 - 2\omega^2)}{\tilde{\omega}} , \qquad\qquad B_1 = -2\left(b + i(2\omega r_- - am) \right) ,$$
$$B_2 = 2(1 - 2i\omega) , \qquad\qquad B_3 = -2(1 + b)\eta\tilde{\omega} - 2i\omega - \Lambda_{lm} - a^2\tilde{\omega}^2 . \tag{B.34}$$

---

[4]Note that

$$\frac{K^2}{\Delta} = \Delta\omega^2 + 4\omega^2 r - 2am\omega + 4\omega^2 + \frac{(2\omega r_+ - am)^2}{2b(r - r_+)} - \frac{(2\omega r_- - am)^2}{2b(r - r_-)} .$$

We take the branch $\text{Im}\,[\tilde{\omega}] > 0$ for $\omega^2 < \mu^2$, so that $\tilde{\omega} = i\sqrt{\mu^2 - \omega^2}$ for bounded modes.

Since we want to impose the exponentially decaying boundary condition at infinity, we transform y by

$$y = e^{i\tilde{\omega}z} z^{-B_2/2 - i\eta} f(z) \,, \tag{B.35}$$

and bring $z = +\infty$ to a finite point by $u = (z - z_0)/z$. Then Eq. (B.33) transform into

$$u(1-u)^2 \frac{\mathrm{d}^2 f}{\mathrm{d}u^2} + (c_1 + c_2 u + c_3 u^2)\frac{\mathrm{d}f}{\mathrm{d}u} + (c_4 + c_5 u)f = 0 \,, \tag{B.36}$$

with

$$c_1 = \frac{B_1}{z_0} + B_2 \,, \qquad\qquad c_2 = -2(1 + i\eta - i\tilde{\omega}z_0 + c_1) \,,$$

$$c_3 = c_1 + 2(1 + i\eta) \,, \qquad\qquad c_4 = \left(i\tilde{\omega}z_0 - \left(\frac{B_2}{2} + i\eta \right) \right)c_1 + B_3 \,,$$

$$c_5 = \left(\frac{B_2}{2} + i\eta \right)\left(\frac{B_2}{2} + i\eta + \frac{B_1}{z_0} + 1 \right) \,. \tag{B.37}$$

In the same way as Sec. B.1, we expand f as

$$f(u) = \sum_{n=0}^{\infty} b_n u^n \,,$$

and obtain the three term recurrence relation

$$c_1 b_1 + c_4 b_0 = 0 \,,$$
$$\alpha_n b_{n+1} + \beta_n b_n + \gamma_n b_{n-1} = 0 \,, \tag{B.38}$$

where

$$\alpha_n = (n+1)(n+c_1) \,,$$
$$\beta_n = -2n(n-1) + nc_2 + c_4 \,,$$
$$\gamma_n = (n-1)(n-2+c_3) + c_5 \,. \tag{B.39}$$

The appropriate sequence which satisfies the boundary condition at $r \to \infty (u = 1)$ is the minimal sequence (see Appendix B.1). The minimal solution exists only for special ω, which is the solution to

$$-\frac{\beta_0}{\alpha_0} = -\frac{\gamma_1}{\beta_1 -}\frac{\alpha_1 \gamma_2}{\beta_2 -} \cdots \,. \tag{B.40}$$

Eq. (B.40) can be solved by the usual root finding method[5]. After obtaining ω, the

---

[5]We construct the continued fraction in right-hand-side of Eq. (B.40) in a similar way as explained in Appendix B.1. To speed up the calculation, we expand the asymptotic form of $U_n = a_{n+1}/a_n$ up to

$$U_n = 1 + \frac{x_1}{\sqrt{n}} + \frac{x_2}{n} + \frac{x_3}{n^{3/2}} + \mathcal{O}(n^{-2}) \,.$$

The coefficients x_i is given by

$$x_1 = \pm i\sqrt{c_1 + c_2 + c_3} \,,$$
$$x_2 = i(\eta - \tilde{\omega}z_0) - \frac{3}{4} \,,$$
$$x_3 = -\frac{x_1}{2}(c_1 + \frac{3}{2}) - \frac{x_2}{2x_1}\left(-i(\eta - \tilde{\omega}z_0) - \frac{7}{4} \right) - \frac{c_4 + c_5 - 2i\eta}{2x_1} \,.$$

The $\pm$ in x_1 must be chosen such that the real part of x_1 is negative. For the bounded modes $|\omega| < \mu$, $+$ sign is appropriate one. This type of expansion is also used to determine the quasi-normal modes [73].

coefficients b_n is obtained from the three term recurrence relation (B.40) with $b_{-1} = 0, b_0 = 1$.

B.2.2   Up-mode and Down-mode

Next, we solve for both up-mode and down-mode. The boundary conditions are

$$
R^{\text{up}}_{lm\omega} \longrightarrow
\begin{cases}
B_{\text{in}}(\omega)(r - r_+)^{-i\frac{2r_+}{r_+ - r_-}(\omega - m\Omega_H)} + B_{\text{out}}(\omega)(r - r_+)^{+i\frac{2r_+}{r_+ - r_-}(\omega - m\Omega_H)} , & (r \to r_+) \\
r^{-i\frac{\mu^2 - 2\omega^2}{\sqrt{\omega^2 - \mu^2}}} \frac{e^{+i\sqrt{\omega^2 - \mu^2}r}}{r} , & (r \to +\infty)
\end{cases}
$$
$$\tag{B.41}$$

for up-mode and

$$
R^{\text{down}}_{lm\omega} \longrightarrow
\begin{cases}
B^*_{\text{out}}(\omega)(r - r_+)^{-i\frac{2r_+}{r_+ - r_-}(\omega - m\Omega_H)} + B^*_{\text{in}}(\omega)(r - r_+)^{+i\frac{2r_+}{r_+ - r_-}(\omega - m\Omega_H)} , & (r \to r_+) \\
r^{+i\frac{\mu^2 - 2\omega^2}{\sqrt{\omega^2 - \mu^2}}} \frac{e^{-i\sqrt{\omega^2 - \mu^2}r}}{r} , & (r \to +\infty)
\end{cases},
$$
$$\tag{B.42}$$

for down-mode. To obtain the solution, we further transform Eq. (B.33) by $y = z^{-B_2/2} h(z)$ and $v = \tilde{\omega}z$, which results in

$$
v(v - \tilde{\omega}z_0) \left(\frac{d^2 h}{dv^2} + \left(1 - \frac{2\eta}{v}\right) h \right) + d_1 \tilde{\omega} \frac{dh}{dv} + \left(d_2 + d_3 \frac{\tilde{\omega}}{v}\right) h = 0 ,
\tag{B.43}
$$

with

$$
d_1 = B_1 + z_0 B_2 , \qquad\qquad d_2 = B_3 - \frac{B_2}{2}\left(\frac{B_2}{2} - 1\right) ,
$$
$$
d_3 = -\frac{B_2}{2}\left(B_1 + z_0\left(\frac{B_2}{2} + 1\right)\right) .
\tag{B.44}
$$

We expand h by the coulomb wave function $u_{L+\nu}$ as

$$
h = \sum_{L=-\infty}^{+\infty} b_L^{(c)} u_{L+\nu} .
\tag{B.45}
$$

Here, ν is an undetermined constant which will be determined below. The coulomb wave functions are the solution to the coulomb wave equation

$$
\frac{d^2 u_{L+\nu}}{dv^2} + \left(1 - \frac{2\eta}{v} - \frac{(L+\nu)(L+\nu+1)}{v^2}\right) u_{L+\nu} = 0 ,
\tag{B.46}
$$

and the satisfy recurrence relations

$$
\frac{du_{L+\nu}}{dv} = -\frac{L+\nu+1}{2L+2\nu-1} u_{L+\nu-1} - Q_L u_{L+\nu} - \frac{L+\nu}{2L+2\nu+3}\left[1 + \frac{\eta^2}{(L+\nu+1)^2}\right] u_{L+\nu-1} ,
\tag{B.47}
$$

$$
\frac{1}{v} u_{L+\nu} = \frac{1}{2L+2\nu-1} u_{L+\nu-1} - Q_L u_{L+\nu} + \frac{1}{2L+2\nu+3}\left[1 + \frac{\eta^2}{(L+\nu+1)^2}\right] u_{L+\nu+1} ,
\tag{B.48}
$$

87

where

$$Q_L = \frac{\eta}{(L+\nu)(L+\nu+1)} \ . \tag{B.49}$$

After some algebra, we obtain the three-term recurrence relation for $b_L^{(c)}$ as

$$\alpha_{(c)L}^\nu b_{L+1}^{(c)} + \beta_{(c)L}^\nu b_L^{(c)} + \gamma_{(c)L}^\nu b_{L-1}^{(c)} = 0 \ , \tag{B.50}$$

with

$$\alpha_{(c)L}^\nu = -\frac{\tilde{\omega}}{2L+2\nu+1}\left[(L+\nu+1)(L+\nu+2)z_0 - (L+\nu+2)d_1 - d_3\right] \ , \tag{B.51}$$

$$\beta_{(c)L}^\nu = (L+\nu)(L+\nu+1) + d_2 + \omega Q_L[(L+\nu)(L+\nu+1)z_0 - d_1 - d_3] \ , \tag{B.52}$$

$$\gamma_{(c)L}^\nu = -\frac{\tilde{\omega}}{2L+2\nu+1}\left[(L+\nu)(L+\nu-1)z_0 + (L+\nu-1)d_1 - d_3\right]$$
$$\times \left(1 + \frac{\eta^2}{(L+\nu)^2}\right) \ . \tag{B.53}$$

We choose ν such that the sequence $b_L^{(c)}$ becomes the minimal. Let us derive the equation which determines ν. As explained in Appendix B.1, minimal sequence satisfies the relation

$$U(L) \equiv \frac{b_L^{(c)}}{b_{L-1}^{(c)}} = -\frac{\gamma_{(c)L}^\nu}{\beta_{(c)L}^\nu-}\frac{\alpha_{(c)L}^\nu \gamma_{(c)L+1}^\nu}{\beta_{(c)L+1}^\nu-}\cdots \ . \tag{B.54}$$

A similar expression for lowering operator holds:

$$U^\dagger(L) \equiv \frac{b_{L-1}^{(c)}}{b_L^{(c)}} = -\frac{\alpha_{(c)L-1}^\nu}{\beta_{(c)L-1}^\nu-}\frac{\gamma_{(c)L-1}^\nu \alpha_{(c)L-2}^\nu}{\beta_{(c)L-2}^\nu-}\cdots \ . \tag{B.55}$$

These relations imply

$$U(L)U^\dagger(L) = 1 \ . \tag{B.56}$$

We chose ν as a solution of Eq. (B.56) with $L = 0$. We construct the continued fraction following the numerical methods in [74]. After ν is obtained, we determine coefficients $b_L^{(c)}$ by multiplying raising and lowering operators $U(L)$ and $U^\dagger(L)$ to $b_0 = 1$.

The coulomb wave equation (B.46) has two independent solutions. The appropriate solution for the up and down modes are

$$g_{L+\nu}(v) \pm if_{L+\nu}(v) = (-1)^L e^{\pi\eta \mp i\pi(\nu+1/2)} e^{\pm iv}(2L+2\nu+1)\frac{\Gamma(L+\nu+1)}{\Gamma(L+\nu+1\mp i\eta)}$$
$$\times (2v)^{L+\nu+1} U(L+\nu+1\pm i\eta, 2L+2\nu+2, \mp 2iv) \ , \quad \text{(B.57)}$$

where $U(a,b,z)$ is the confluent hypergeometric function [75]. The asymptotic form at $v = \tilde{\omega}(r - r_-) \to \infty$ is given by

$$g_{L+\nu}(v) \pm if_{L+\nu}(v) \xrightarrow{v\to\infty} \exp\left(\pm i\left(v - \eta\log 2v - (L+\nu)\frac{\pi}{2} + \sigma_L^\pm\right)\right) \ , \tag{B.58}$$

$$\sigma_L^\pm = \mp i\log\left[(l+2\nu+1)e^{\pi\eta/2}\frac{\Gamma(L+\nu+1)}{\Gamma(L+\nu+1\mp i\eta)}\right] \ . \tag{B.59}$$

Thus, $+$ sign gives the up mode and $-$ sign gives the down mode. To summarize, the up-mode is given by

$$R_{lm\omega}^{\text{up}} = N_{\text{up}}^{-1}(r-r_+)^{k_+}(r-r_-)^{k_- - B_2/2}e^{+i\tilde{\omega}(r-r_-)+\pi\eta - i\pi(\nu+1/2)}$$

$$\times \sum_{L=-\infty}^{L=+\infty}(-1)^L b_L^{(c)}\frac{(2L+2\nu+1)\Gamma(L+\nu+1)}{\Gamma(L+\nu+1-i\eta)}(2\tilde{\omega}(r-r_-))^{L+\nu+1}$$

$$\times U(L+\nu+1+i\eta, 2L+2\nu+2, -2i\tilde{\omega}(r-r_-)), \qquad \text{(B.60)}$$

where N_{up}^{-1} is the normalization constant given by

$$N_{\text{up}}^{-1} = \frac{e^{+i\eta\log(2\tilde{\omega})}}{\sum_{L=-\infty}^{L=+\infty}(-1)^L b_L^{(c)}\frac{(2L+2\nu+1)\Gamma(L+\nu+1)}{\Gamma(L+\nu+1-i\eta)}}. \qquad \text{(B.61)}$$

The quantities $k_\pm, \tilde{\omega}, \eta$, and B_2 are shown in Eqs. (B.32) and (B.34). The down-mode is given by a similar expression.

B.2.3   In-mode

Finally, we solve for in-mode $R_{lm\omega}^{\text{in}}$, which satisfies the boundary condition

$$R_{lm\omega}^{\text{in}} \longrightarrow \begin{cases} (r-r_+)^{-i\frac{2r_+}{r_+-r_-}(\omega - m\Omega_H)}, & (r\to r_+) \\ A_{\text{in}}(\omega)r^{+i\frac{\mu^2-2\omega^2}{\sqrt{\omega^2-\mu^2}}}(\omega)\frac{e^{-i\sqrt{\omega^2-\mu^2}r_*}}{r} + A_{\text{out}}(\omega)r^{-i\frac{\mu^2-2\omega^2}{\sqrt{\omega^2-\mu^2}}}\frac{e^{+i\sqrt{\omega^2-\mu^2}r_*}}{r}, & (r\to +\infty) \end{cases}. \qquad \text{(B.62)}$$

To obtain the solution, we transform Eq. (B.2) by

$$R_{lm\omega} = (r-r_+)^{k_+}\left(\frac{r-r_-}{r_+-r_-}\right)^{k_-}e^{i\tilde{\omega}(r_+-r)}p(u), \qquad u = \frac{r_+-r}{2b}. \qquad \text{(B.63)}$$

Here, we take $k_\pm$ as

$$k_+ = -i\frac{2\omega r_+ - am}{2b}, \qquad\qquad k_- = -i\frac{2\omega r_- - am}{2b}. \qquad \text{(B.64)}$$

After some calculation, we obtain

$$u(1-u)\frac{d^2 p}{du^2} + (1+2k_+ - (1+2(k_+ + k_-)+1)u)\frac{dp}{du} - (k_+ + k_-)(k_+ + k_- + 1)p$$

$$= e_1 u(1-u)\frac{dp}{du} + (e_2 + e_3 u)p, \qquad \text{(B.65)}$$

with

$$\begin{aligned} e_1 &= -4ib\tilde{\omega}, \\ e_2 &= -a^2\tilde{\omega}^2 - \Lambda_{lm} - 2(1+b)\tilde{\omega}\eta + 4\omega^2 - 2ib\tilde{\omega}(1+2k_+), \\ e_3 &= 4ib\tilde{\omega}(1+k_+ + k_- - i\eta). \end{aligned} \qquad \text{(B.66)}$$

Now, we expand p in terms of hypergeometric functions

$$p = \sum_{n=-\infty}^{+\infty} c_n^\nu p_{n+\nu},$$

$$p_{n+\nu} = {}_2F_1(n+\nu+k_+ + k_- + 1, -n-\nu+k_+ + k_-, 1+2k_+; u). \qquad \text{(B.67)}$$

Here, $p_{n+\nu}$ satisfies the hypergeometric differential equation

$$u(1-u)\frac{\mathrm{d}^2 p_{n+\nu}}{\mathrm{d}u^2} + (1 + 2k_+ - (1 + 2(k_+ + k_-) + 1)u)\frac{\mathrm{d}p_{n+\nu}}{\mathrm{d}u}$$
$$- (-n - \nu + k_+ + k_-)(n + \nu + 1 + k_+ + k_-)p_{n+\nu} = 0 . \qquad (B.68)$$

Furthermore, we introduce a constant ν, which will be determined below.

Using the recurrence relation of hypergeometric functions $_2F_1(a, b, c; u)$

$$u(1-u)\frac{d}{du}{}_2F_1(a, b, c; u) = \frac{b(c-a)}{b-a+1}{}_2F_1(a-1, b+1, c; u)$$
$$+ \left(\frac{(a-c)(b+1)}{b-a;1} + bu\right){}_2F_1(a, b, c; u) , \qquad (B.69)$$

$$u_2F_1(a, b, c; u) = \left(1 + \frac{(c-a)(a-1)}{(a-b)(b-a+1)} - \frac{(c-b)(c-b+1)}{(a-b)(b-a-1)}\right){}_2F_1(a, b, c; u)$$
$$+ \frac{b(c-a)}{(a-b)(b-a+1)}{}_2F_1(a-1, b+1, c; u)$$
$$+ \frac{a(c-b)}{(a-b)(b-a-1)}{}_2F_1(a+1, b-1, c; u) , \qquad (B.70)$$

we obtain the three-term recurrence relation

$$\alpha_n^\nu c_{n+1}^\nu + \beta_n^\nu c_n^\nu + \gamma_n^\nu c_{n-1}^\nu = 0 , \qquad (B.71)$$

where

$$\alpha_n^\nu = -\frac{(n+\nu+1-(k_+ + k_m))(n+\nu+1-(k_+ - k_-))}{2(2(n+\nu)+3)(n+\nu+1)}$$
$$\times (e_1(n+\nu+2) + (k_+ + k_-)e_1 + e_3) , \qquad (B.72)$$

$$\beta_n^\nu = (n+\nu)(n+\nu+1) + e_2 - \frac{e_3}{2}\left(1 + \frac{(k_+ + k_-)(k_+ - k_-)}{(n+\nu)(n+\nu+1)}\right)$$
$$+ \frac{k_+ - k_-}{2}e_1\left(1 + \frac{(k_+ + k_-)(k_+ + k_- + 1)}{(n+\nu)(n+\nu+1)}\right) , \qquad (B.73)$$

$$\gamma_n^\nu = -\frac{(n+\nu+(k_+ + k_m))(n+\nu+(k_+ - k_-))}{2(2(n+\nu)+1)(n+\nu)}$$
$$\times (e_1(n+\nu-1) - (k_+ + k_-)e_1 - e_3) . \qquad (B.74)$$

We determine ν in parallel with the determination of ν in Appendix. B.2.2. Interestingly, ν determined here coincides with the ν determined by Eq. (B.56). This allows one to obtain the reflection and transmission coefficients without numerically integrating the wave equation on the Kerr space-time [76, 77].

The in-mode solution can also be written by the confluent Heun function, implemented in MATHEMATICA. Notice that Eq. (B.65) takes the same form as the confluent Heun equation (B.5). Thus, p can be written by

$$p(u) = \text{HeunC}\left[-(e_2 + (k_+ + k_-)(k_+ + k_- + 1)), e_3, 1 + 2k_+, 1 + 2k_-, -e_1, u\right] . \qquad (B.75)$$

Appendix C

Calculation of the energy flux

In this appendix, we evaluate fluxes at the horizon (3.28) and at infinity (3.29) and show the flux formulas (3.30) and (3.31). Substituting the energy-momentum tensor of the scalar field

$$T_{\mu\nu}(\phi) = \partial_\mu\phi\partial_\nu\phi + g_{\mu\nu}\left(-\frac{1}{2}(\partial\phi)^2 - V(\phi)\right) , \tag{C.1}$$

to (3.28) and (3.29), we obtain

$$F_{\mathcal{H}^+} = 2Mr_+ \int d\cos\theta\, d\varphi\, \partial_t\phi(\partial_t\phi + \Omega_H\partial_\varphi\phi)|_{r\to r_+} , \tag{C.2}$$

$$F_{\mathcal{I}^+} = \int d\cos\theta\, d\varphi\, r^2\partial_t\phi\partial_r\phi|_{r\to\infty} . \tag{C.3}$$

As shown in Sec. 3.2, the axion field ϕ up to the leading order in λ is given by

$$\phi = \sqrt{E_1}\phi_1 + \sqrt{E_2}\phi_2 + E_1\sqrt{E_2}\phi_0^{(1)} + \sqrt{E_1}E_2\phi_3^{(1)} , \tag{C.4}$$

where

$$\phi_0^{(1)} = -3\lambda e^{-i\omega_0 t}\sum_l S_{l0\omega_0}(\theta)\int dr' d\cos\theta'(r'^2 + a^2\cos^2\theta')S_{l0\omega_0}(\theta')$$
$$\times G_{l0\omega_0}(r,r')R_1(r')^2 R_2^*(r')S_1(\theta')^2 S_2^*(\theta') + \text{c.c.} , \tag{C.5}$$

$$\phi_3^{(1)} = -3\lambda e^{-i\omega_3 t + 3\varphi}\sum_l S_{l3\omega_3}(\theta)\int dr' d\cos\theta'(r'^2 + a^2\cos^2\theta')S_{l3\omega_3}(\theta')$$
$$\times G_{l3\omega_3}(r,r')R_1^*(r')R_2(r')^2 S_1^*(\theta')S_2(\theta')^2 + \text{c.c.} . \tag{C.6}$$

The first, second, and third terms in Eq. (C.4) contribute to the flux at the horizon $F_{\mathcal{H}^+}$ and the fourth term contributes to the flux to infinity $F_{\mathcal{I}^+}$.[1]

Let us first calculate the flux at the horizon. The contribution from the first and the second terms is responsible for the superradiant instability of the $l = m = 1$ and the $l = m = 2$ modes. From the calculation in Sec. 2.1.2, their flux at the horizon is simply given by

$$-2\omega_{1,I}E_1 - 2\omega_{2,I}E_2 . \tag{C.7}$$

---

[1]The fourth term can also contribute to the flux at the horizon. However, its contribution is much smaller than that the flux from $m = 0$, so we simply ignore it.

To evaluate the contribution from the third term, $\phi_0^{(1)}$, we need its asymptotic behavior near the horizon. Using the expression (3.11) and the asymptotic behavior of the mode functions (3.12), the behavior of the field close to the horizon is

$$\phi_0^{(1)} \to -3\lambda e^{-i\omega_0 t - i\omega_0 r_*} \sum_l Z_l^{\mathcal{H}^+} S_{l0\omega_0}(\theta) + \text{c.c.} , \tag{C.8}$$

with

$$Z_l^{\mathcal{H}^+} = \frac{1}{W_{l0}(\omega_0)} \int dr' d\cos\theta' (r'^2 + a^2\cos^2\theta') S_{l0\omega_0}(\theta') R_{l0\omega_0}^{\text{up}}(r')$$
$$\times R_1(r')^2 R_2^*(r') S_1(\theta')^2 S_2^*(\theta') . \tag{C.9}$$

From the orthogonality relation

$$\int d\cos\theta \, S_{lm\omega} S_{l'm\omega}^* = \delta_{ll'} , \tag{C.10}$$

we obtain

$$F_{\mathcal{H}^+} \supset 2Mr_+ \int d\cos\theta d\varphi \, \partial_t\phi_0^{(1)}(\partial_t\phi_0^{(1)} + \Omega_H\partial_\varphi\phi_0^{(1)})|_{r\to r_+}$$
$$= \left(72\pi M\lambda^2 r_+ \omega_0^2 \sum_l |Z_l^{\mathcal{H}^+}|^2\right) E_1^2 E_2$$
$$\equiv F_0 E_1^2 E_2 . \tag{C.11}$$

The energy flux to infinity is calculated similarly. The asymptotic behavior of $\phi_3^{(1)}$ near infinity $r \to +\infty$ is

$$\phi_3^{(1)} \to -\frac{\mu^2}{2} \frac{e^{-i\omega_3 t + 3i\varphi + i\sqrt{\omega_3^2 - \mu^2} r_*}}{r} \sum_l Z_l^{\mathcal{I}^+} S_{l3\omega_3}(\theta) + \text{c.c.} , \tag{C.12}$$

with

$$Z_l^{\mathcal{I}^+} = \frac{1}{W_{l3}(\omega_3)} \int dr' d\cos\theta' (r'^2 + a^2\cos^2\theta') R_{l3\omega_3}^{\text{in}}$$
$$\times R_1^*(r') R_2(r')^2 S_1^*(\theta') S_2(\theta')^2 . \tag{C.13}$$

Substituting Eq. (C.12) to Eq. (C.3), we obtain

$$F_{\mathcal{I}^+} = \left(36\pi\lambda^2\omega_3\sqrt{\omega_3^2 - \mu^2} \sum_l |Z_l^{\mathcal{I}^+}|^2\right) E_1 E_2^2$$
$$\equiv F_3 E_1 E_2^2 . \tag{C.14}$$

The net energy flux is obtained by summing up all the fluxes, which gives

$$F_{\text{tot}}^E = F_{\mathcal{H}^+} + F_{\mathcal{I}^+}$$
$$= -2\omega_{1,I}E_1 - 2\omega_{2,I}E_2 + F_0 E_1^2 E_2 + F_3 E_1 E_2^2 . \tag{C.15}$$

The angular momentum flux can be calculated from the energy fluxes calculated above. Note that the ratio between the angular momentum flux and the energy flux of the wave

with given (ω, m) is m/ω [25]. Using this relation and noting that the respective terms in Eq. (C.15) have $(\omega, m) = (\omega_1, 1), (\omega_2, 2), (\omega_0, 0)$, and $(\omega_3, 3)$, we obtain the total angular momentum flux as

$$F^J_{\text{tot}} = -2\omega_{1,I}\frac{1}{\omega_{1,R}}E_1 - 2\omega_{2,I}\frac{2}{\omega_{2,R}}E_2 + \frac{3}{\omega_3}F_3 E_1 E_2^2 \ . \tag{C.16}$$

Other fluxes relevant in Chapter 5 can be calculated in a similar manner. For example, the energy flux by the $m = 0$ mode excited by the process involving the $l = m = 1$ and $l = m = 2$ fundamental modes and the $l = m = 2$ overtone mode is given by

$$\begin{aligned} F_{12o^*} =& 288\pi M\lambda^2 r_+(\omega_0')^2 \\ &\times \sum_{l \geq 0}\left|\frac{1}{W_{l0}(\omega_0')}\int dr' d\cos\theta'(r'^2 + a^2\cos^2\theta')R^{\text{up}}_{l0\omega_0'}\right. \\ &\left. \times R_1(r')R_2(r')R_o^*(r')S_1(\theta')S_2(\theta')S_o^*(\theta')\right| \ , \end{aligned} \tag{C.17}$$

where o stands for the $l = m = 2$ overtone mode, and $\omega_0' = \omega_1 + \omega_2 - \omega_o$. Factor 4 difference from Eq. (C.11) comes from the fact that there is no symmetric factor for this case.

C.1 Non-relativistic estimation

Here, we estimate the values of F_0 and F_3 in the non-relativistic limit $\mu M \ll 1$. In the non-relativistic limit, the frequency $\omega^{(lmn)}$ can be approximated as [28]

$$\omega^{(lmn)} \sim \mu\left(1 - \frac{(\mu M)^2}{2n^2}\right) \ , \tag{C.18}$$

thus $M\omega^{(lmn)} \to 0$ as $\mu M \to 0$. Then the spheroidal harmonics $S_{lm\omega}$ can be simply approximated by the spherical harmonics

$$S_{lm\omega} \sim Y_{lm}(\theta) \ . \tag{C.19}$$

The radial mode functions, the superradiant unstable mode, in-, and up- mode are given by the wave function of the hydrogen atom in the region far from the horizon $r \gg r_+$ [28],

$$\begin{aligned} R_{lm\omega^{(lmn)}} \sim &(\mu M)^2\sqrt{\frac{(-l + n - 1)!}{\pi n^4(l + n)!}} \\ &\times \left(\frac{2\mu^2 Mr}{n}\right)^l e^{-\frac{\mu^2 Mr}{n}}L^{2l+1}_{-l+n-1}\left(\frac{2\mu^2 Mr}{n}\right) \ , \end{aligned} \tag{C.20}$$

$$R^{\text{in}}_{lm\omega} \sim (2kr)^l e^{-ikr}{}_1F_1\left(\frac{i\mu^2}{k} + l + 1; 2l + 2; 2ikr\right) \ , \tag{C.21}$$

$$\begin{aligned} R^{\text{up}}_{lm\omega} \sim &(-2ikM)^{-\frac{i\mu^2}{k}+1}(-2ikr)^l e^{ikr} \\ &\times U\left(-\frac{i\mu^2 M}{k} + l + 1, 2l + 2, -2ikr\right) \ , \end{aligned} \tag{C.22}$$

where $k = \sqrt{\omega^2 - \mu^2}$. We took the normalization of R^{in} to put $R^{\text{in}}(r = 0) = 1$ for $l = 0$ modes. In parallel to the fact that the radial extension of the hydrogen wave function is

given by the Bohr radius, Equation (C.20) shows that the radial extension of the cloud is $\sim nM/(\mu M)^2$ [17].

From the asymptotic form of the confluent Hypergeometric functions $_1F_1$ and U [75], asymptotic behavior of the in- and up-mode near infinity are given by

$$R_{lm\omega}^{\text{in}} \rightarrow \frac{(-2ik)^{-1-\frac{i\mu^2 M}{k}}\Gamma(2l+2)e^{il\frac{\pi}{2}}}{\Gamma\left(-\frac{i\mu^2 M}{k}+l+1\right)}r^{-\frac{i\mu^2 M}{k}}\frac{e^{-ikr}}{r}$$

$$+ \frac{(2ik)^{-1+\frac{i\mu^2 M}{k}}\Gamma(2l+2)e^{-il\frac{\pi}{2}}}{\Gamma\left(\frac{i\mu^2 M}{k}+l+1\right)}r^{+\frac{i\mu^2 M}{k}}\frac{e^{+ikr}}{r} \; , \tag{C.23}$$

$$R_{lm\omega}^{\text{up}} \rightarrow r^{\frac{i\mu^2 M}{k}}\frac{e^{ikr}}{r} \; , \tag{C.24}$$

We can also evaluate their Wronskian as

$$W_{lm}(\omega) \sim 2ikM\frac{(-2ikM)^{-1-\frac{i\mu^2 M}{k}}\Gamma(2l+2)e^{il\frac{\pi}{2}}}{\Gamma\left(-\frac{i\mu^2 M}{k}+l+1\right)} \; . \tag{C.25}$$

We first evaluate $Z_0^{\mathcal{H}^+}$ and $Z_3^{\mathcal{I}^+}$ that gives dominant contribution in the l summation of F_0 and F_3, respectively. Since the cloud resides in the region very far from the black hole, we can approximate all the mode functions involved in $Z_0^{\mathcal{H}^+}$ and $Z_3^{\mathcal{I}^+}$ by the expressions (C.20) - (C.22), we obtain

$$Z_0^{\mathcal{H}^+} \sim \frac{1}{W_{00}(\omega_0)}C_{0;112}\int dr' r'^2 R_{00\omega_0}^{\text{up}}(r')R_1(r')^2 R_2^*(r') \; , \tag{C.26}$$

$$Z_3^{\mathcal{I}^+} \sim \frac{1}{W_{33}(\omega_3)}C_{0;221}\int dr' r'^2 R_{33\omega_3}^{\text{in}}(r')R_2(r')^2 R_1^*(r') \; , \tag{C.27}$$

with

$$\omega_0 \sim \mu\left(1 - \frac{7}{36}(\mu M)^2\right) \; , \tag{C.28}$$

$$\omega_3 \sim \mu\left(1 + \frac{1}{72}(\mu M)^2\right) \; , \tag{C.29}$$

$$C_{0;112} = \int d\cos\theta' Y_{00}(\theta')Y_{11}(\theta')^2 Y_{22}^*(\theta') \; , \tag{C.30}$$

$$C_{3;112} = \int d\cos\theta' Y_{33}(\theta')Y_{22}(\theta')^2 Y_{11}^*(\theta') \; . \tag{C.31}$$

Let us examine the μM dependence of $Z_l^{\mathcal{H}^+}$ and $Z_l^{\mathcal{I}^+}$. From Eqs. (C.28) and (C.29), we observe

$$k_0 = \sqrt{\omega_0^2 - \mu^2} \sim i\sqrt{\frac{7}{18}}\mu(\mu M) \; , \tag{C.32}$$

$$k_3 = \sqrt{\omega_3^2 - \mu^2} \sim \frac{1}{6}\mu(\mu M) \; . \tag{C.33}$$

Therefore, k in the expressions in the non-relativistic limit is proportional to $\mu(\mu M)$. By changing integration variable r' to $\tilde{r}' = \mu(\mu M)r'$, one can confirm that leading μM dependence of the coefficients $Z_0^{\mathcal{H}^+}$ and $Z_3^{\mathcal{I}^+}$ are

$$Z_0^{\mathcal{H}^+} \propto (\mu M)^2 M^3 \; , \qquad\qquad Z_3^{\mathcal{H}^+} \propto M^3 \; . \tag{C.34}$$

Therefore, leading μ dependence of the fluxes F_0 and F_3 are

$$F_0 \sim 2\pi M r_+ \mu^6 |Z_0^{\mathcal{H}^+}|^2 \sim 4.2 \times 10^{-7} \times \frac{r_+}{M}(\mu M)^{10} \ , \tag{C.35}$$

$$F_3 \sim \pi \frac{\mu^6(\mu M)}{6} |Z_3^{\mathcal{I}^+}|^2 \sim 1.1 \times 10^{-8} \times (\mu M)^7 \ . \tag{C.36}$$

Here, we numerically evaluated the radial and angular integration to obtain the μM independent factor. Other fluxes F_{abc} can be calculated similarly.

Appendix D

Details of nonlinear calculation

In this appendix, we show the details of the numerical calculation in Sec. 4.

D.1 Discrete orthogonality of spherical harmonics

Here, we show the discrete orthogonal property of the spherical harmonics, which is used to efficiently compute the projection of the nonlinear terms in Eq. (4.7). The discrete orthogonality is the following:

$$\sum_{j=1}^{J} \sum_{i=1}^{I} Y_{lm}(\mu_j) Y_{l'm'}(\mu_j) e^{im\lambda_i} e^{-im'\lambda_i} \omega_j = I \delta_{ll'} \delta_{mm'} \ , \tag{D.1}$$

where

$$\lambda_i = 2\pi \frac{i-1}{I} \ , \tag{D.2}$$

and μ_j is the j-th zero of the J-th order Legendre polynomial $P_J(x)$, $P_J(\mu_j) = 0$. Here, ω_j is the weight given by

$$\omega_j = \frac{2(1-\mu_j^2)}{J^2(P_{J-1}(\mu_j))^2} \ . \tag{D.3}$$

In addition, I and J must satisfy $I > |m - m'|$ and $l + l' < 2J - 1$. These conditions determine the number of grid points in the φ and θ directions.

One can easily confirm that the summation over i in Eq. (D.1) gives the factor $I\delta_{mm'}$. The summation over j can be performed using the property

$$\int_{-1}^{+1} f(x) dx = \sum_{j=1}^{J} f(\mu_j) \omega_j \ , \tag{D.4}$$

for polynomial $f(x)$ with degree smaller than $2J - 1$. Using Eq. (D.4), the summation with j is evaluated as

$$\sum_{j=1}^{J} Y_{lm}(\mu_j) Y_{l'm}(\mu_j) \omega_j = \int Y_{lm}(x) Y_{l'm}(x) = \delta_{ll'} \ . \tag{D.5}$$

Let us prove Eq. (D.4).

Proof. We first approximate $f(x)$ by the Lagrange interpolation

$$L(x) = \sum_{j=1}^{J} f(\mu_j) \prod_{k=1,k\neq j}^{J} \frac{x - \mu_k}{\mu_j - \mu_k} . \tag{D.6}$$

At $x = \mu_j (j = 1, 2, \cdots, J)$,

$$L(\mu_j) = f(\mu_j) . \tag{D.7}$$

Suppose that the degree of $f(x)$ is K. If $K \leq J - 1$, Eq. (D.7) immediately implies

$$f(x) = L(x) , \tag{D.8}$$

for any x.

Now consider the case with $J \leq K \leq 2J - 1$. Since the $f(x) - L(x)$ has the same zeros as $P_J(x)$, it must be written as,

$$f(x) - L(x) = P_J(x)S(x) , \tag{D.9}$$

where $S(x)$ is the polynomial with degree $K - J(\leq J - 1)$, which can be written as a sum of $P_n(x)(n < J)$. Then the orthogonality of the Legendre polynomial implies the right-hand side of Eq. (D.9) to vanish after integration over $(-1, 1)$. Therefore, for $K < 2J - 1$, we have

$$\int_{-1}^{+1} f(x)dx = \int_{-1}^{+1} L(x)dx . \tag{D.10}$$

The right-hand side of Eq. (D.10) is evaluated as follows:

$$\int_{-1}^{+1} L(x)dx = \sum_{j=1}^{J} f(\mu_j) \int dx \frac{\prod_{k=1}^{J}(x - \mu_k)}{(\mu - \mu_j)\prod_{k=1,k\neq j}^{J}(\mu_j - \mu_k)}$$
$$= \sum_{j=1}^{J} f(\mu_j) \int dx \frac{P_J(x)}{(x - \mu_j)P_J'(\mu_j)} . \tag{D.11}$$

From the recurrence relation

$$(n + 1)P_{n+1}(x) = (2n + 1)xP_n(x) - nP_{n-1}(x) , \tag{D.12}$$

we have

$$(n + 1) \det \begin{pmatrix} P_{n+1}(x) & P_n(x) \\ P_{n+1}(y) & P_n(y) \end{pmatrix} - n \det \begin{pmatrix} P_n(x) & P_{n-1}(x) \\ P_n(y) & P_{n-1}(y) \end{pmatrix}$$
$$= (2n + 1)(x - y)P_n(x)P_n(y) . \tag{D.13}$$

By summing up this relation from $n = 0$ to $n = J - 1$, we obtain

$$J(P_J(x)P_{J-1}(y) - P_J(y)P_{J-1}(x)) = \sum_{n=0}^{J-1}(2n + 1)(x - y)P_n(x)P_n(y) , \tag{D.14}$$
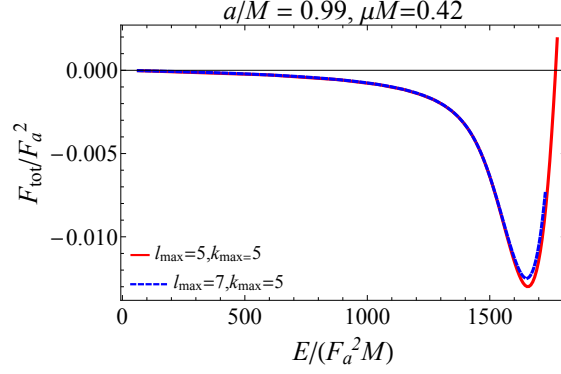
98

Figure D.1: The Same figure as Fig. 4.1, but added the blue dotted curve corresponds to the calculation with additional higher multipole modes $(l, m) = (7, 1)$ and $(7, 3)$. Dependence of the total flux $F_{\text{tot}}(A_1)$ on the energy E. The red solid curve in this figure shows the same line as the blue solid curve in the right panel of Fig. 4.1. Owing to the high computational cost to include the additional modes, blue dotted curve is ended around $A_1 \sim 11$.

which implies

$$\frac{P_J(x)}{x - \mu_j} = \sum_{n=0}^{J-1} (2n+1) \frac{P_n(\mu_j)}{J P_{J-1}(\mu_j)} P_n(x) , \tag{D.15}$$

for $y = \mu_j$. Thus, we can further evaluate the integral in Eq. (D.11) as

$$\int dx \frac{P_J(x)}{(x - \mu_j) P_J'(\mu_j)} = \int dx \sum_{n=0}^{J-1} (2n+1) \frac{P_n(\mu_j)}{J P_{J-1}(\mu_j) P_J'(\mu_j)} P_n(x)$$
$$= \frac{2}{J P_{J-1}(\mu_j) P_J'(\mu_j)}$$
$$= \frac{2(1 - \mu_j^2)}{(J P_{J-1}(\mu_j))^2} . \tag{D.16}$$

Here, we used the relation

$$(1 - x^2) \frac{dP_J(x)}{dx} = J P_{J-1}(x) - J x P_J(x) . \tag{D.17}$$

Combining Eqs. (D.10), (D.11), and (D.16), we obtain

$$\int_{-1}^{1} dx f(x) = \int_{-1}^{+1} dx L(x) = \sum_{j=1}^{J} \frac{2(1 - \mu_j^2)}{(J P_{J-1}(\mu_j))^2} f(\mu_j) . \tag{D.18}$$

$\square$

D.2 Justification of the truncation of l and k

In this appendix, we show that the truncating l and n at $l_{\max} = 5, k_{\max} = 5$, which is adopted in our numerical calculation values does not change the results much. In
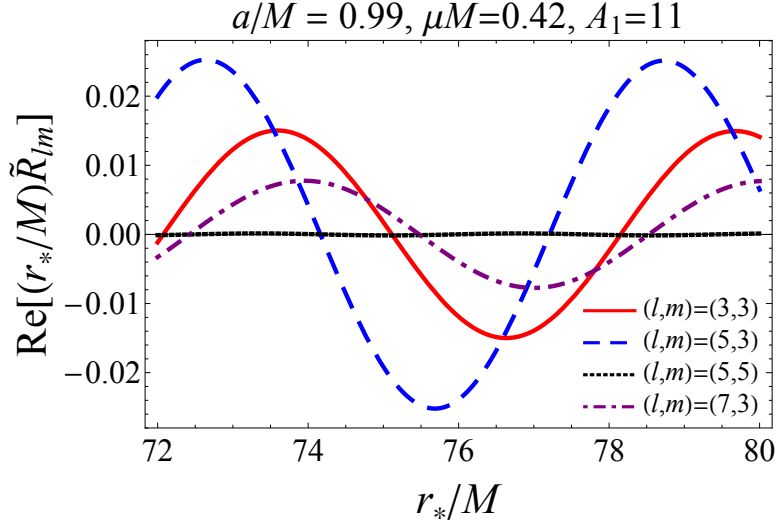
Figure D.2: Each curve shows the real part of $(r_*/M)\tilde{R}_{lm}$ near infinity at the amplitude $A_1 = 11$. Again, $A_1 \sim 11$ is the largest value of the amplitude we could have calculated, owing to the high computational cost. The red solid curve, blue dashed curve, black dotted curve, and purple dashed dotted curves correspond to $(l, m) = (3,3), (5,3), (5,5)$, and $(7,3)$ modes, respectively.

particular, we present the results with two additional modes $(l, m) = (7,1)$, and $(7,3)$. Here, we fix the axion mass and the black hole spin to $\mu M = 0.42$ and $a/M = 0.99$, respectively. We also set the axion potential to be the cosine type (3.2). We do not consider the modes with $m \geq 5$, since our calculation already show that these modes are suppressed compared to the $m = 1$ and 3 modes (see, for example, Fig. D.3). Therefore, the modes $(l, m) = (7,1)$, and $(7,3)$ would be sufficient to justify the truncation at $l_{\max} = 5$ and $k_{\max} = 5$.

We show how the total flux F_{tot} depends on the energy E in Fig. D.1. It can be seen that the total flux differs by a factor of ~ 1.3 when the amplitude is large. This is due to the addition of the radiation mode $(l, m) = (7,3)$, which increases the flux to infinity.

To see the contribution of each mode to the flux to infinity, we show the behavior of the mode function near infinity for $A_1 = 11$ and $m \geq 3$ in Fig. D.2. The figure shows that the $(l, m) = (5,3)$ mode makes the largest contribution, contrary to the naively expected dominance of the $(l, m) = (3,3)$ mode. This large contribution of the higher l modes is similar to the gravitational radiation from the axion cloud [78]. The next dominant mode is the $(l, m) = (3,3)$ mode, while the $(7,3)$ mode is further suppressed but not completely negligible in determining saturated configuration. However, as shown in the figure, including the $(l, m) = (7,3)$ mode has little effect on the configuration of all modes. Therefore, the energy flux through $(l, m) = (7,3)$ can be calculated by the linearized expression from the configuration neglecting the $(l, m) = (7,3)$ mode, as shown in Fig. D.4. Furthermore, we confirmed that the $(l, m) = (5,5)$ mode gives a much smaller contribution than the $m = 3$ mode. Thus, including higher m modes does not change the result, as we noted at the beginning of this section.
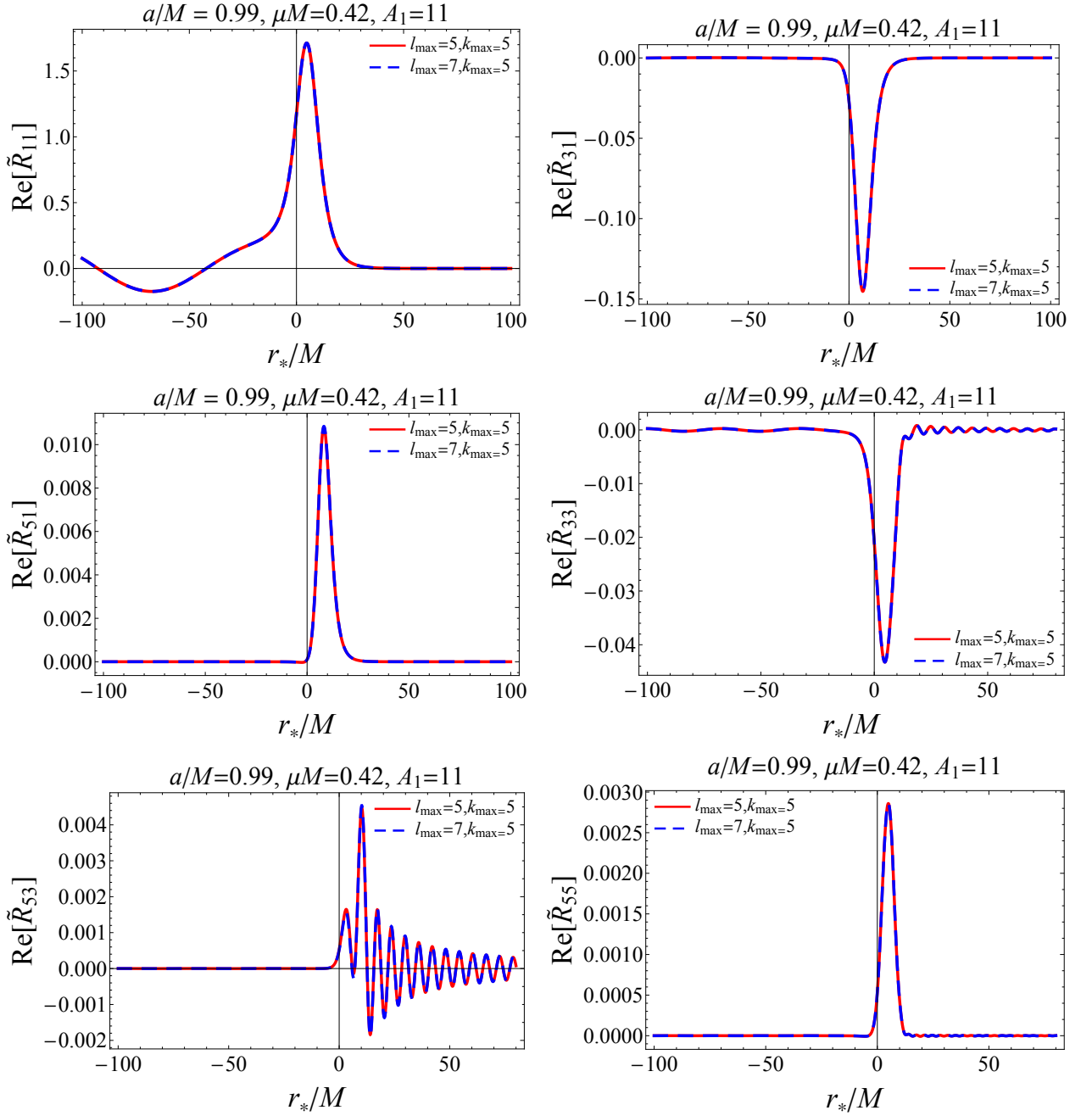
Figure D.3: Each panel shows the real part of mode function $\tilde{R}_{lm}$ at amplitude $A_1 = 11$. From the top left to the bottom right, $\tilde{R}_{11}, \tilde{R}_{31}, \tilde{R}_{51}, \tilde{R}_{33}, \tilde{R}_{53}$ and $\tilde{R}_{55}$ are plotted, respectively. The red solid curve is calculated with six modes $(l, m) = (1, 1), (3, 1), (5, 1), (3, 3), (5, 3),$ and $(5, 5)$, while the blue dashed curve is calculated by adding two more modes $(l, m) = (7, 1)$ and $(7, 3)$.
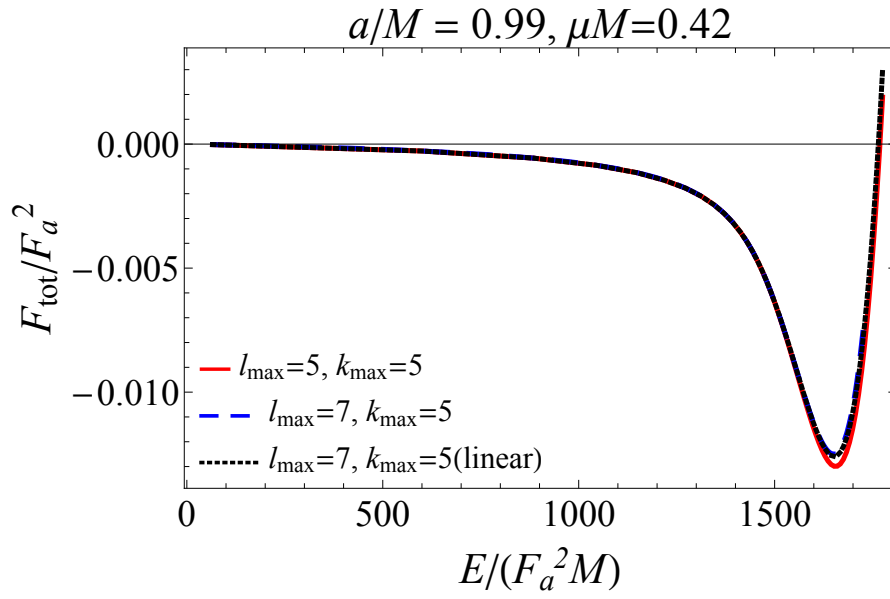
Figure D.4: The same figure as Fig. D.1 but added new black dotted curve calculated by solving the linearized equation from the configuration neglecting the higher l, m modes. . The red solid and blue dashed curves correspond to the respective lines in the right panel of Fig. D.1.

Bibliography

[1] R.D. Peccei and H.R. Quinn, *CP Conservation in the Presence of Instantons*, *Phys. Rev. Lett.* **38** (1977) 1440.

[2] S. Weinberg, *A New Light Boson?*, *Phys. Rev. Lett.* **40** (1978) 223.

[3] F. Wilczek, *Problem of Strong P and T Invariance in the Presence of Instantons*, *Phys. Rev. Lett.* **40** (1978) 279.

[4] J.E. Kim, *Weak Interaction Singlet and Strong CP Invariance*, *Phys. Rev. Lett.* **43** (1979) 103.

[5] M.A. Shifman, A.I. Vainshtein and V.I. Zakharov, *Can Confinement Ensure Natural CP Invariance of Strong Interactions?*, *Nucl. Phys. B* **166** (1980) 493.

[6] A.R. Zhitnitsky, *On Possible Suppression of the Axion Hadron Interactions. (In Russian)*, *Sov. J. Nucl. Phys.* **31** (1980) 260.

[7] M. Dine, W. Fischler and M. Srednicki, *A Simple Solution to the Strong CP Problem with a Harmless Axion*, *Phys. Lett. B* **104** (1981) 199.

[8] M. Dine and W. Fischler, *The Not So Harmless Axion*, *Phys. Lett.* **120B** (1983) 137.

[9] J. Preskill, M.B. Wise and F. Wilczek, *Cosmology of the Invisible Axion*, *Phys. Lett.* **120B** (1983) 127.

[10] L.F. Abbott and P. Sikivie, *A Cosmological Bound on the Invisible Axion*, *Phys. Lett.* **120B** (1983) 133.

[11] L. Hui, J.P. Ostriker, S. Tremaine and E. Witten, *Ultralight scalars as cosmological dark matter*, *Phys. Rev. D* **95** (2017) 043541 [1610.08297].

[12] C.B. Adams et al., *Axion Dark Matter*, in *2022 Snowmass Summer Study*, 3, 2022 [2203.14923].

[13] M.B. Green, J.H. Schwarz and E. Witten, *Superstring Theory Vol. 2*, Cambridge Monographs on Mathematical Physics, Cambridge University Press (2012), 10.1017/CBO9781139248570.

[14] P. Svrcek and E. Witten, *Axions In String Theory*, *JHEP* **06** (2006) 051 [hep-th/0605206].

[15] A. Arvanitaki, S. Dimopoulos, S. Dubovsky, N. Kaloper and J. March-Russell, *String Axiverse*, *Phys. Rev.* **D81** (2010) 123530 [0905.4720].

[16] M. Cicoli, M. Goodsell and A. Ringwald, *The type IIB string axiverse and its low-energy phenomenology*, *JHEP* **10** (2012) 146 [`1206.0819`].

[17] A. Arvanitaki and S. Dubovsky, *Exploring the String Axiverse with Precision Black Hole Physics*, *Phys. Rev.* **D83** (2011) 044026 [`1004.3558`].

[18] R. Penrose, *Gravitational Collapse: the Role of General Relativity*, *Nuovo Cimento Rivista Serie* **1** (1969) 252.

[19] R. Penrose and R.M. Floyd, *Extraction of rotational energy from a black hole*, *Nature* **229** (1971) 177.

[20] W.H. Press and S.A. Teukolsky, *Floating Orbits, Superradiant Scattering and the Black-hole Bomb*, *Nature* **238** (1972) 211.

[21] J.D. Bekenstein, *Extraction of energy and charge from a black hole*, *Phys. Rev. D* **7** (1973) 949.

[22] S.A. Teukolsky and W.H. Press, *Perturbations of a rotating black hole. III. Interaction of the hole with gravitational and electromagnetic radiation.*, *Astrophys. J.* **193** (1974) 443.

[23] J.D. Bekenstein and M. Schiffer, *The Many faces of superradiance*, *Phys. Rev.* **D58** (1998) 064014 [`gr-qc/9803033`].

[24] W.E. East, F.M. Ramazanoğlu and F. Pretorius, *Black Hole Superradiance in Dynamical Spacetime*, *Phys. Rev. D* **89** (2014) 061503 [`1312.4529`].

[25] R. Brito, V. Cardoso and P. Pani, *Superradiance: New Frontiers in Black Hole Physics*, *Lect. Notes Phys.* **906** (2015) pp.1 [`1501.06570`].

[26] T. Damour, N. Deruelle and R. Ruffini, *On Quantum Resonances in Stationary Geometries*, *Lett. Nuovo Cim.* **15** (1976) 257.

[27] T.J.M. Zouros and D.M. Eardley, *INSTABILITIES OF MASSIVE SCALAR PERTURBATIONS OF A ROTATING BLACK HOLE*, *Annals Phys.* **118** (1979) 139.

[28] S.L. Detweiler, *KLEIN-GORDON EQUATION AND ROTATING BLACK HOLES*, *Phys. Rev.* **D22** (1980) 2323.

[29] V. Cardoso and S. Yoshida, *Superradiant instabilities of rotating black branes and strings*, *JHEP* **07** (2005) 009 [`hep-th/0502206`].

[30] S.R. Dolan, *Instability of the massive Klein-Gordon field on the Kerr spacetime*, *Phys. Rev.* **D76** (2007) 084001 [`0705.2880`].

[31] R. Brito, V. Cardoso and P. Pani, *Black holes as particle detectors: evolution of superradiant instabilities*, *Class. Quant. Grav.* **32** (2015) 134001 [`1411.0686`].

[32] A. Arvanitaki, M. Baryakhtar and X. Huang, *Discovering the QCD Axion with Black Holes and Gravitational Waves*, *Phys. Rev.* **D91** (2015) 084011 [`1411.2263`].

[33] A. Arvanitaki, M. Baryakhtar, S. Dimopoulos, S. Dubovsky and R. Lasenby, *Black Hole Mergers and the QCD Axion at Advanced LIGO*, *Phys. Rev. D* **95** (2017) 043001 [1604.03958].

[34] LIGO SCIENTIFIC, VIRGO, KAGRA collaboration, *All-sky search for gravitational wave emission from scalar boson clouds around spinning black holes in LIGO O3 data*, 2111.15507.

[35] A.K. Saha, P. Parashari, T.N. Maity, A. Dubey, S. Bouri and R. Laha, *Bounds on ultralight bosons from the Event Horizon Telescope observation of Sgr A**, 2208.03530.

[36] N. Siemonsen, T. May and W.E. East, *SuperRad: A black hole superradiance gravitational waveform model*, 2211.03845.

[37] H. Yoshino and H. Kodama, *Bosenova collapse of axion cloud around a rotating black hole*, *Prog. Theor. Phys.* **128** (2012) 153 [1203.5070].

[38] G. Mocanu and D. Grumiller, *Self-organized criticality in boson clouds around black holes*, *Phys. Rev. D* **85** (2012) 105022 [1203.4681].

[39] H. Yoshino and H. Kodama, *The bosenova and axiverse*, *Class. Quant. Grav.* **32** (2015) 214001 [1505.00714].

[40] A. Gruzinov, *Black Hole Spindown by Light Bosons*, 1604.06422.

[41] H. Fukuda and K. Nakayama, *Aspects of Nonlinear Effect on Black Hole Superradiance*, *JHEP* **01** (2020) 128 [1910.06308].

[42] M. Baryakhtar, M. Galanis, R. Lasenby and O. Simon, *Black hole superradiance of self-interacting scalar fields*, *Phys. Rev. D* **103** (2021) 095019 [2011.11646].

[43] D. Baumann, H.S. Chia and R.A. Porto, *Probing Ultralight Bosons with Binary Black Holes*, *Phys. Rev. D* **99** (2019) 044001 [1804.03208].

[44] D. Baumann, H.S. Chia, R.A. Porto and J. Stout, *Gravitational Collider Physics*, *Phys. Rev. D* **101** (2020) 083019 [1912.04932].

[45] T. Takahashi and T. Tanaka, *Axion clouds may survive the perturbative tidal interaction over the early inspiral phase of black hole binaries*, 2106.08836.

[46] T. Takahashi, H. Omiya and T. Tanaka, *Axion cloud evaporation during inspiral of black hole binaries – the effects of backreaction and radiation*, 2112.05774.

[47] D. Baumann, G. Bertone, J. Stout and G.M. Tomaselli, *Ionization of Gravitational Atoms*, 2112.14777.

[48] X. Tong, Y. Wang and H.-Y. Zhu, *Termination of superradiance from a binary companion*, *Phys. Rev. D* **106** (2022) 043002 [2205.10527].

[49] W.E. East, *Vortex String Formation in Black Hole Superradiance of a Dark Photon with the Higgs Mechanism*, *Phys. Rev. Lett.* **129** (2022) 141103 [2205.03417].

[50] J.a.G. Rosa and T.W. Kephart, *Stimulated Axion Decay in Superradiant Clouds around Primordial Black Holes*, *Phys. Rev. Lett.* **120** (2018) 231102 [`1709.06581`].

[51] T. Ikeda, R. Brito and V. Cardoso, *Blasts of Light from Axions*, *Phys. Rev. Lett.* **122** (2019) 081101 [`1811.04950`].

[52] H. Omiya, T. Takahashi and T. Tanaka, *Renormalization group analysis of superradiant growth of self-interacting axion cloud*, *PTEP* **2021** (2021) 043E02 [`2012.03473`].

[53] H. Omiya, T. Takahashi, T. Tanaka and H. Yoshino, *Impact of multiple modes on the evolution of self-interacting axion condensate around rotating black holes*, `2211.01949`.

[54] H. Omiya, T. Takahashi and T. Tanaka, *Adiabatic evolution of the self-interacting axion field around rotating black holes*, *PTEP* **2022** (2022) 043E03 [`2201.04382`].

[55] D. Brill, P. Chrzanowski, C. Martin Pereira, E. Fackerell and J. Ipser, *Solution of the scalar wave equation in a kerr background by separation of variables*, *Phys. Rev. D* **5** (1972) 1913.

[56] J.L. Roberts, N.R. Claussen, S.L. Cornish, E.A. Donley, E.A. Cornell and C.E. Wieman, *Controlled collapse of a bose-einstein condensate*, *Phys. Rev. Lett.* **86** (2001) 4211.

[57] L.Y. Chen, N. Goldenfeld and Y. Oono, *Renormalization Group Theory for Global Asymptotic Analysis*, *Phys. Rev. Lett.* **73** (1994) 1311 [`cond-mat/9407024`].

[58] L.-Y. Chen, N. Goldenfeld and Y. Oono, *The Renormalization group and singular perturbations: Multiple scales, boundary layers and reductive perturbation theory*, *Phys. Rev.* **E54** (1996) 376 [`hep-th/9506161`].

[59] T. Kunihiro, *A Geometrical Formulation of the Renormalization Group Method for Global Analysis*, *Progress of Theoretical Physics* **94** (1995) 503.

[60] S.-I. Ei, K. Fujii and T. Kunihiro, *Renormalization group method for reduction of evolution equations: Invariant manifolds and envelopes*, *Annals Phys.* **280** (2000) 236 [`hep-th/9905088`].

[61] S.L. Shapiro and S.A. Teukolsky, *Black holes, white dwarfs, and neutron stars : the physics of compact objects*, John Wiley & Sons, Ltd (1983).

[62] J.M. Bardeen, B. Carter and S.W. Hawking, *The Four laws of black hole mechanics*, *Commun. Math. Phys.* **31** (1973) 161.

[63] K.S. Thorne, *Disk accretion onto a black hole. 2. Evolution of the hole.*, *Astrophys. J.* **191** (1974) 507.

[64] G. Ficarra, P. Pani and H. Witek, *Impact of multiple modes on the black-hole superradiant instability*, *Phys. Rev.* **D99** (2019) 104019 [`1812.02758`].

[65] R.P. Kerr, *Gravitational field of a spinning mass as an example of algebraically special metrics*, *Phys. Rev. Lett.* **11** (1963) 237.

[66] E.W. Leaver, *Solutions to a generalized spheroidal wave equation: Teukolsky's equations in general relativity, and the two- center problem in molecular quantum mechanics*, Journal of Mathematical Physics **27** (1986) 1238 [https://doi.org/10.1063/1.527130].

[67] J. Blandin, R. Pons and G. Marcilhacy, *General solution of teukolsky's equation*, Lettere al Nuovo Cimento (1971-1985) **38** (1983) 561.

[68] H. Suzuki, E. Takasugi and H. Umetsu, *Perturbations of Kerr-de Sitter black hole and Heun's equations*, Prog. Theor. Phys. **100** (1998) 491 [gr-qc/9805064].

[69] W. Gautschi, *Computational aspects of three-term recurrence relations*, SIAM Review **9** (1967) 24 [https://doi.org/10.1137/1009002].

[70] W.H. Press, B.P. Flannery and S.A. Teukolsky, *Numerical recipes. The art of scientific computing* (1986).

[71] E.W. Leaver, *An Analytic representation for the quasi normal modes of Kerr black holes*, Proc. Roy. Soc. Lond. A **402** (1985) 285.

[72] J.M. Bardeen, W.H. Press and S.A. Teukolsky, *Rotating black holes: Locally nonrotating frames, energy extraction, and scalar synchrotron radiation*, Astrophys. J. **178** (1972) 347.

[73] H.-P. Nollert, *Quasinormal modes of Schwarzschild black holes: The determination of quasinormal frequencies with very large imaginary parts*, Phys. Rev. **D47** (1993) 5253.

[74] R. Fujita and H. Tagoshi, *New numerical methods to evaluate homogeneous solutions of the Teukolsky equation*, Prog. Theor. Phys. **112** (2004) 415 [gr-qc/0410018].

[75] *"NIST Digital Library of Mathematical Functions."* http://dlmf.nist.gov/, Release 1.1.7 of 2022-10-15.

[76] S. Mano, H. Suzuki and E. Takasugi, *Analytic Solutions of the Teukolsky Equation and Their Low Frequency Expansions*, Progress of Theoretical Physics **95** (1996) 1079 [9603020].

[77] M. Sasaki and H. Tagoshi, *Analytic black hole perturbation approach to gravitational radiation*, Living Rev. Rel. **6** (2003) 6 [gr-qc/0306120].

[78] H. Yoshino and H. Kodama, *Gravitational radiation from an axion cloud around a black hole: Superradiant phase*, PTEP **2014** (2014) 043E02 [1312.2326].